Processing and Opto-Mechanical Characterization of Transparent Glass-Filled Epoxy Particulate Composites

by

Austin B. Branch

A thesis submitted to the Graduate Faculty of
Auburn University
in partial fulfillment of the
requirements for the Degree of
Master of Science

Auburn, Alabama
May 2, 2020

Keywords: Dynamic Fracture, Photoelasticity, High-Speed Photography, Transparent Particulate Composites, Experimental Mechanics

Approved by

Hareesh V. Tippur, Chair, McWane Professor of Mechanical Engineering
Jeffrey C. Suhling, Quina Distinguished Professor of Mechanical Engineering
James S. Davidson, Gottlieb Professor of Civil Engineering

Abstract

Optically transparent materials have a wide range of applications in areas such as face shields, ground vehicle and aircraft windows, and bullet-resistant enclosures. Glass, the standard material used for applications requiring transparency, is often deficient in providing low weight, high mechanical strength, and toughness. Hence, the development of polymer-based transparent composites has the potential to offer complementary material systems for such applications at a low cost.

In this work, a method to produce transparent glass-filled epoxy composites by refractive index matching of an epoxy matrix and rod-shaped E-glass fillers has been developed. These composites were processed at different filler volume fractions (V_f) from 0% to 15%, with transparency maintained at each V_f. The initial investigation included quasi-static three-point bending of edge-cracked specimens to determine the critical stress intensity factor (SIF), K_{Icr}, values. Improvement in K_{Icr} over neat epoxy was seen in each case, with a maximum increase of approximately 30%. Furthermore, this composite was observed to exhibit birefringence, thus making mechanical characterization through photoelastic methods feasible. To determine the mechanical properties, first, the stress optic constant, f_σ, had to be evaluated for each sample. This was done using symmetric four-point bending configuration and recording the fringe patterns with a dark-field polariscope and time-lapse photography. Under quasi-static three-point bending, optical fringes in each sample were observed, recorded, and subsequently, stress-intensity factors were evaluated at various load levels and compared to the analytical counterparts. The values determined experimentally matched

analytically determined ones closely, thus validating the use of photoelastic characterization of this material.

Mode-I dynamic fracture tests were also performed at three different loading rates, and the photoelastic stress fringes were recorded using high-speed photography and a laser light illumination. The mode-I stress intensity factor values, K_I, were evaluated for each image recorded during the fracture event using crack-tip fringe digitization and least-squares analysis of optical data. For each loading rate, as the volume fraction of the filler material was increased, a monotonic increase in the K_{Icr} values corresponding to crack initiation in this transparent composite was observed. Additionally, a complementary finite element analysis of pre-crack initiation SIF values was performed, showing a good match with the experimental results.

Finally, the high-speed photoelastic measurements were extended to mixed-mode (mode-I + mode-II) fracture of these transparent glass-epoxy composites. A simple method of varying the crack length in an eccentrically impacted edge-cracked specimen was adopted to alter the mode-mixity at crack initiation. Isochromatic fringes near the crack tip were recorded throughout the fracture event from which the mode-I and mode-II stress intensity factor values were successfully extracted. The SIF histories for samples of the equivalent filler volume fractions, but different crack length, were compared, and significant variation in the mode-mixity at crack initiation was observed. Additionally, the effect of volume fraction on the mixed-mode fracture behavior was studied, and a monotonic increase in the K_{eff} values at crack initiation with respect to filler volume fraction was observed.

Acknowledgments

I would like to express my deepest gratitude to my advisor, Dr. Hareesh V. Tippur, for his guidance and support throughout my time at Auburn University. From when he first welcomed me to the Laboratory for Failure Mechanics and Optical Techniques when I was an undergraduate student, through my time as a graduate student, Dr. Tippur has been a constant source of motivation and inspiration. For his encouragement, patience, and persistent help, I am very grateful.

I also wish to thank Dr. Jeffrey Suhling and Dr. James Davidson for their willingness to serve on my committee as well as for the crucial knowledge I gained from their courses. Thanks are also due to my labmates, Bala, Vinod, Robert, Amith, Chengyun, and Abhiram, for their support and memorable times.

I am grateful to my parents, John and Susan Branch, for their never-ending love and support. Thank you for always encouraging me and making me who I am today.

Finally, I must thank my wife, Scharli, without whom this work would not be possible. Thank you for always being by my side through all the ups and downs, for putting up with the late nights and the early mornings, and always believing in me, even when I did not believe in myself. Thank you for your relentless patience and unwavering love. But most of all, thank you for being my best friend. With my whole heart, I dedicate this work to you.

Table of Contents

List of Figures

List of Tables

CHAPTER 1: INTRODUCTION

Optically transparent engineering materials are present in virtually all settings in everyday life. Common examples include home windowpanes, light bulbs, table glassware, and eyeglasses. They also have a wide range of functional applications in areas such as face shields, ground vehicle and aircraft windows, and bullet-resistant enclosures (Figure 1-1).

Figure 1-1: Examples of transparent composite applications
(Sources: (a) www.defencetalk.com, (b) www.cbsistatic.com,
(c) www.bulletresistant.bulletguard.com)

The former category is typically produced from conventional transparent materials, such as glass or transparent polymers, as they are primarily focused on near-perfect transparency even at the cost of durability. In contrast, the latter applications require materials with excellent optical transparency and superb mechanical properties, such as low weight and high impact resistance.

Some methods to utilize conventional materials for these high-performance applications also exist. One way to accomplish this is simply by increasing the thickness of the glass. Glass is often thought of as the preferred material, given that it is fully transparent with excellent clarity and low cost. However, by increasing the thickness as

suggested, its application may become impractical when low weight is essential to function. While the strength of glass in domestic contexts is satisfactory, it is not so well suited for items that need to withstand impact loading conditions.

The process of layering multiple materials has also been used as a technique to create a strong lightweight transparent material [1] [2]. Layered structures are typically produced from materials such as traditional glass, Polymethyl methacrylate (PMMA), polycarbonate, among others [3]. However, layering materials can create similar weight problems if glass layers are present. Further, the production of these materials is often complicated and limited in its application to complex structures/geometries.

Another material used in transparent structures are transparent polymers. Although they are often lighter than glass and offer ease of manufacturing, many are limited by optical properties, typically still lack stiffness, strength, and are brittle. It is because of these limitations in such critical settings, safety, and protective applications, that there is a need for innovation within the field of optically transparent materials.

One possible solution is polymer-based transparent composite materials, which offer the opportunity for added strength and optimal transparency by allowing adjustments in the ratio of the reinforcement to matrix materials.

1.1 Particulate Composites

The term composite encompasses several different subsets of materials, but for this research, the focus will be on particulate composites. Like most composite materials, they are known for their ability to provide strength at a lower weight for applications in

the protective context, such as aerospace, automotive, and other industries requiring high-performance materials.

Particulate composites are generally created by dispersing particles into a binding matrix. The particles are used generally as reinforcement material, although compliant fillers are known to toughen the material while decreasing the overall stiffness. In the context of developing a particulate composite, common reinforcement materials are mica, alumina, glass and carbon fibers, and silica. Depending on the desired application for the material, the exact reinforcement material and its shape and volume fraction vary.

Through careful selection of a reinforcement material, mechanical properties can be enhanced; namely, fracture toughness, low weight, and fatigue characteristics, among others [4]–[13]. Studies on this subject have included examining many different particulate composite materials under varied testing conditions.

One such study was performed by Kitey et al. [10], which investigated the effect of particle size and filler-matrix adhesion on the dynamic fracture of glass-filled epoxy composites. The elastic characteristics were found to be unaffected by the filler size and adhesion strength. When the filler and matrix materials were weakly bonded, the fracture toughness was highly dependent on the filler size. The opposite was found for the strongly bonded case, where the filler size did not have an effect on the fracture toughness. As exhibited in Figure 1-2, in both cases (weakly and strongly bonded), higher fracture toughness was found when compared to neat epoxy.

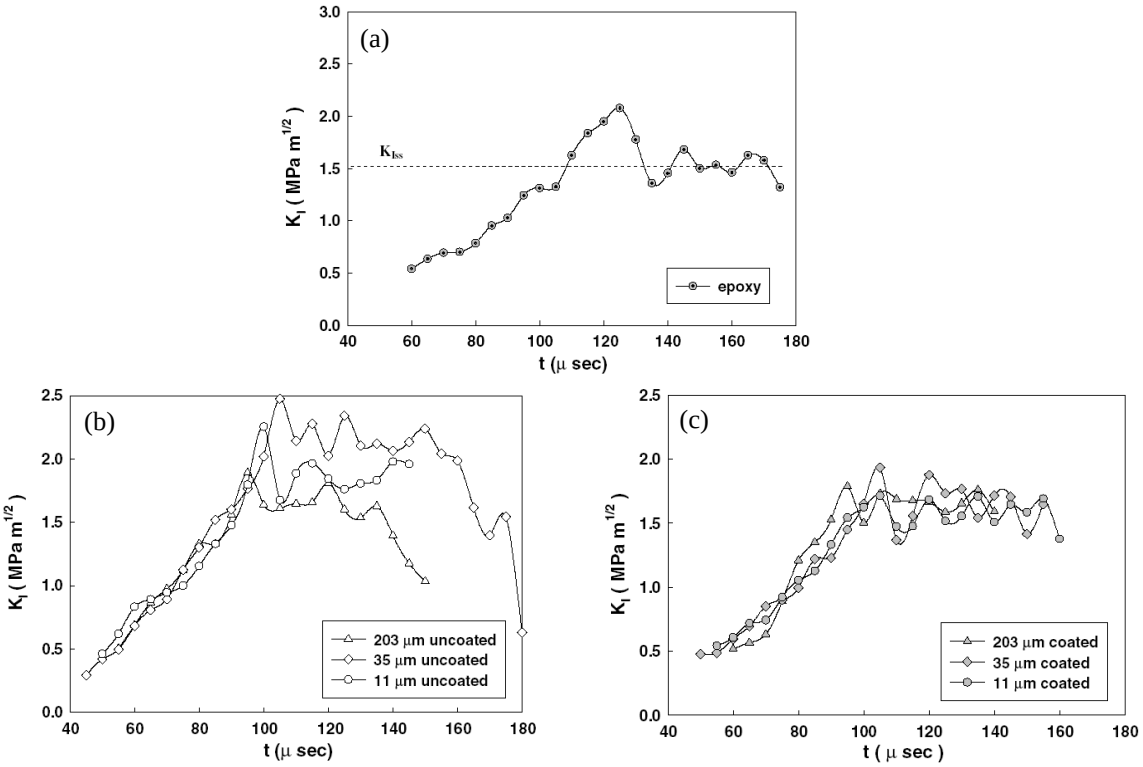

Figure 1-2: Stress intensity factor histories for (a) neat epoxy, (b) weakly-bonded glass-filled epoxy, and (c) strongly-bonded epoxy samples (Reproduced from Ref. [10])

Kushvaha et al. [14] also studied the dynamic fracture behavior of glass-filled epoxy composites. The analysis was focused on determining the effect of adjusting the glass-filler of various aspect ratios (rods, spheres, and flakes) and filler volume fractions. In each case, there was a significant increase in the crack initiation toughness. As shown in Figure 1-3, a maximum improvement of 145% was achieved in the 15% V_f rod-shaped glass-filled epoxy composites when compared to neat epoxy.

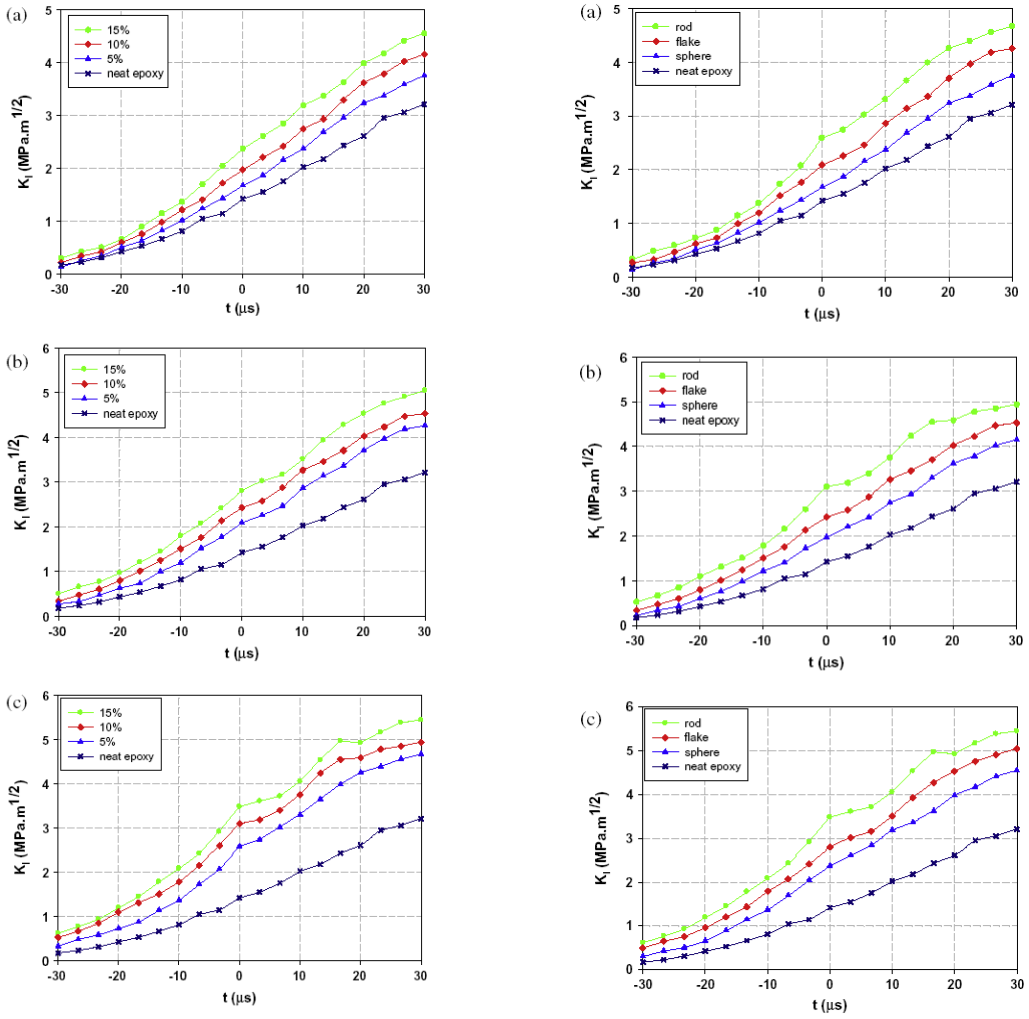

Figure 1-3: (Left) Stress-intensity factor histories for glass-filled epoxy composites of various volume fractions with spherical, flake, and rod-shaped fillers, (a)-(c), respectively. (Right) Stress intensity factor histories for glass-filled epoxy composites of various filler shapers with 5%, 10%, and 15% filler volume fractions, (a)-(c), respectively. (Reproduced from Ref. [14])

In addition, Spanoudakis et al. [13] examined crack propagation in a glass-sphere epoxy composite with respect to particle volume fraction and particle size. His research showed that the elastic modulus was mostly unaffected by particle size at low volume

fractions. As that filler volume fraction increased, larger particle sizes contributed to a slight decrease in elastic modulus.

1.2 Transparent Particulate Composites

Due to the flexibility of using different types of reinforcement materials, as exhibited by the research set out above, particulate composites offer the ability to develop a strong material that can also be made transparent. This is done primarily through two methods.

One method is to reduce the size of the reinforcement material below the wavelength of light [15]. Practically, this process requires a composite with a very low volume fraction of reinforcement, which may not allow for optimal strength and stiffness. Furthermore, agglomeration of nanofillers could be a potential difficulty to overcome. The other, more common method is to match the refractive indices of the constituents, namely transparent fillers with that of the matrix [16]. This method also comes with its own difficulties. When matching indices of refraction to obtain transparency, the indices must be matched to approximately the third decimal place. The high precision required in index matching significantly limits the number of materials with which the matrix or the reinforcement constituent can be paired. Secondly, the transmittance of a composite is also dependent on the filler volume fraction.

Despite these difficulties, several studies have demonstrated the feasibility of producing transparent glass-fiber reinforced polymer composites using refractive index matching.

For example, Liu et al. [17] tested a transparent sc-PLA PMMA composite at multiple volume filler fractions. They found that there was an improved tensile strength without a significant reduction in the transparency of PMMA. However, some studies, as discussed in more detail below, found that as volume fraction increased, the light transmittance of the composite material decreased.

Kagawa et al. [4] examined the thermal behavior of a transparent glass-fiber reinforced epoxy composite material. The results showed that the addition of the glass-fiber filler reduced the coefficient of thermal expansion compared to neat epoxy. However, it was also found that the added glass-fiber filler lowered the light transmittance of the material. Similarly, Iba et al. [8] studied a transparent glass-fiber epoxy composite and various filler volume fractions. There was added tensile strength as volume fraction increased; however, a decrease in the light transmittance of the composite material was observed.

Moreover, Olson et al. [18] investigated the light transmittance and flexural strength of a transparent unidirectional glass-fiber polymethyl methacrylate (PMMA) composite under various volume fractions. Light transmittance decreased as the volume fraction increased. However, the volume fraction increase also caused a flexural strength increase. For the 40% filler volume fraction case, an increase of six times in the flexural strength, and nine times in flexural modulus were measured.

Another category of researchers developed a transparent particulate composite, which was examined under specific criteria to determine its light transmittance properties. Iba et al. [16] developed a transparent SiO_2 fiber epoxy composite that was

tested to determine its light transmittance under specific parameters. Those parameters were the effect of the filler volume fraction, the refractive index mismatch between the epoxy and the reinforcement material, and the fiber radius. Sato et al. [19] examined the effect of the light transmittance with respect to the index mismatch of transparent glass particle epoxy composite materials.

Additional research focused on determining the tensile and flexural strength of the composite material. Lin et al. [5] studied the tensile strength of transparent glass-fiber reinforced PMMA composite, which was found to be twice that of pure PMMA. Klepaczko et al. [12] examined the static and dynamic fracture toughness of a transparent rubber-particle PMMA composite.

Khanna et al. [20] studied the quasi-static Mode-I fracture behavior of a transparent woven E-glass cloth reinforced polyester matrix composite using photoelasticity. From their results, they were able to generate isochromatic fringe patterns that were found to be in good agreement with the experimentally obtained isochromatic fringe patterns.

Epoxy was used in many of the studies discussed above due to its low cost, relatively simple processing, and optical transparency. For those reasons, epoxy is one of the most common types of engineering polymers used in structural composites. However, its brittle nature can be problematic in many applications where catastrophic failure due to cracks could occur. As was shown in the above research, the incorporation of glass fiber into an epoxy matrix has been shown as an effective method to strengthen polymeric materials while maintaining optical transparency Additionally, due to a close

match in the epoxy and glass fiber refractive indices, optical transparency is largely maintained.

Once a transparent sample is created, it is important to understand its mechanical properties. Past works have shown that fracture behavior is dependent on a number of factors, notably strain rate and loading condition (mode-mixity) [14], [21]–[24].

Beginning with strain rate, Schoßig et al. [21] studied glass-fiber reinforced polypropylene (PP) and polybutene-1 (PB-1) composites using a high-speed tensile test. The glass-fiber content and strain rate were varied in the range between 0-40 wt.-% 0.007 - 174 s^{-1}. An increase in the strain rate caused an increase in the tensile strength; thus, a positive strain rate dependence was observed. Cao et al. [22] examined the compressive properties of glass fiber epoxy composites embedded with tetra-needle-like zinc oxide (ZnO) nanowhiskers. Those properties were seen to be significantly impacted by strain rate. Furthermore, the composites were shown to have higher strength with an increased strain rate.

In addition, Shokrieh et al. [24] studied the unidirectional glass-fiber reinforced polymeric composites at varying strain rates, ranging from 0.001 to 100 $s^{-1.}$ It was found that both the compressive strain and modulus were dependent on strain rate, both increasing with increased strain rate.

Kushvaha et al. [14] examined the loading rate effect of the dynamic fracture of glass-filled epoxy composites. As shown in Figure 1-4, the crack initiation toughness was shown to be sensitive to the loading rate, with the slowest loading rate producing the greatest improvement compared to neat epoxy of the respective loading rate.

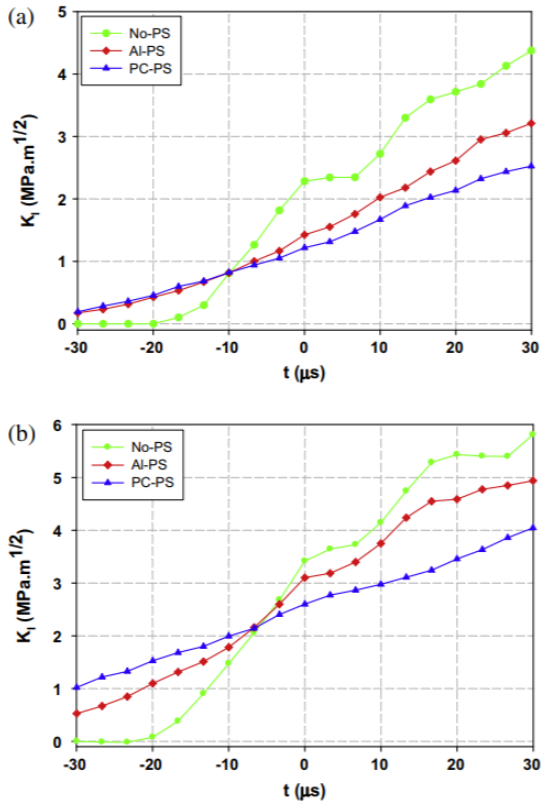

Figure 1-4: Stress intensity factor histories at different loading rates for (a) neat epoxy and (b) glass-filled epoxy samples under dynamic mode-I loading (reproduced from Ref. [14])

As mentioned previously, because these materials are commonly used in contexts involving varying loading conditions (aerospace and automotive production), ranging from simple static loads to dynamic events such as bird strikes and impact from explosives, their mechanical properties need to be studied under similar conditions. Furthermore, when considering the example of an aircraft window, where catastrophic failure would be devastating, the fracture behavior is of particular interest and underscores the need for research in this area.

1.3 Overview of Optical Methods and Photoelasticity

Generally speaking, full-field optical methods have several advantages in their application to fracture mechanics studies, including but not limited to the ability to visualize the entire displacement and stress fields in a particular area of interest, locate the crack-tip throughout a fracture event, and are generally non-contact, thus allowing for their implementation non-invasively. Furthermore, with the recent advances in high-speed photography, full-field optical methods can be used to study dynamic fracture events such as rapid crack growth, including the recording of rapidly changing stress fields as well as identifying the location of the crack tip at various time instants. In addition, some full-field optical methods such as photoelasticity can provide information in real-time, without the need for extensive post-processing.

Photoelasticity is a full-field, nondestructive experimental technique used to measure the stress distribution within solid bodies based on the principle of temporary birefringence. This is certainly not a novel optical phenomenon, and photoelasticity has seen significant developments with continued use as a tool for experimental stress analysis. Because photoelasticity was the chosen optical method to evaluate fracture events in the research set out below, it is discussed in great detail in Chapter 3.

1.4 Objectives

- Develop methods to produce transparent glass-filled epoxy composites at various filler volume fractions
- Investigate the material's birefringence and perform calibration measurements of optical and physical properties
- Demonstrate the feasibility of implementing full-field optical methods such as photoelasticity for the study of quasi-static fracture in glass-filled epoxy composites
- Develop various experimental setups to study the material's dynamic fracture behavior using high-speed photoelasticity.
- Study the effect of filler volume fraction on the static and dynamic fracture behavior of the glass-filled epoxy composites
- Explore the effects of various loading rates and mode-mixites to the material's dynamic fracture behavior using the recorded photoelastic fringe image to measure crack velocity and stress-intensity factor histories

1.5 Thesis Layout

The introduction is the first of six chapters. Chapter 2 describes the material processing methods, sample preparation, and initial optical evaluation applied to the transparent glass-filled epoxy. It also discusses the material transparency and the mechanical and physical properties of the composite material.

The principles of photoelasticity are the focus of Chapter 3. It applies those principles to fracture mechanics, including the methods for digitizing isochromatic fringe

data and evaluating the stress intensity factors. In addition, the optical calibration and characterization of the composites are described.

Chapter 4 discusses the quasi-static fracture testing of the neat and glass-filled epoxy composites. Specifically, the specimen preparation and loading configuration for quasi-static fracture testing are described. A comparison of optical and theoretical results using photoelasticity to accurately determine stress intensity factors is another focus of the chapter.

Photoelastic evaluation is presented again in Chapter 5 but in the context of a dynamic mode-I fracture study. A description of the sample preparation is followed by the experimental setup of the three loading configurations used to achieve three distinct loading rates. Measured crack velocity and mode-I stress intensity factor histories are shown with a discussion of the results in conjunction with high-speed photoelastic images. Finally, an explanation of a complementary finite element analysis performed to supplement experimental results for which closed form solutions do not exist is provided.

This thesis is concluded with Chapter 6, which begins with a description of the experimental method used to study the composites in various mixed-mode dynamic loading conditions. It also continues the discussion that began in Chapter 5 regarding crack velocity and mode-I stress intensity factor histories. Chapter 6 adds mode-II stress intensity factor histories as well as K_{eff} and mode-mixity histories. A detailed evaluation of the results of each type of stress intensity factor histories concludes the chapter and the thesis.

CHAPTER 2: MATERIAL PROCESSING

In this chapter, the material properties, sample preparation, and initial optical evaluation of a transparent glass-filled epoxy are discussed. First, material selection of the filler and matrix components and their individual specifications are discussed. Next, the method for sample preparation of 0% (neat epoxy), 5%, 10%, and 15% volume fraction (V_f) composites and considerations for optimal material transparency are described. This chapter concludes with the methods used for an initial evaluation of material properties for each volume fraction, and results are presented.

2.1 Material Description

In this work, a transparent glass-filled epoxy composite was developed based on the principle of refractive index matching. Rod-shaped E-glass milled glass fibers were used as fillers and were dispersed into a low viscosity epoxy system, Epothin™ from Buehler Inc., USA (Bisphenol-A resin and an Amine based hardener), shown in Figure 2-1 and Figure 2-2.

Figure 2-1: Epothin epoxy system

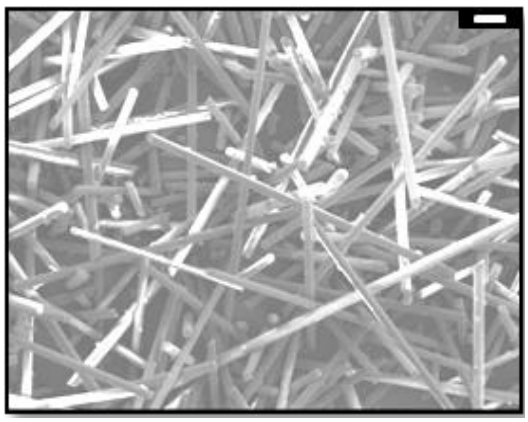

Figure 2-2: Scanning electron microscopy image rod-shaped E-glass milled fibers (scale bar: 50 μm) [14]

The Epothin™ epoxy system and was chosen as the matrix material due to its low viscosity allowing filler materials to be dispersed with relative ease and at higher volume fractions. Furthermore, Epothin™ has a relatively short gel period of thirty minutes, which helps reduce the settlement of filler particles in the mold that can occur before the material is fully cured. Rod-shaped E-glass was selected due to having a near match to the refractive index of the epoxy system allowing for optical transparency. Specifications for the matrix and filler are shown below in Table 2-1:

Table 2-1: Rod-shaped E-Glass fiber and Epothin™ epoxy specifications

	Rod Shaped E-glass	Epothin™
Density	2500 kg/m3	1087.6 kg/m3
Refractive Index	1.576	1.5702
Length (average)	800 μm	-
Diameter (average)	10 μm	-
Aspect Ratio	80	-

2.2 Sample Preparation

As an initial investigation of the optical and physical properties of the glass-filled epoxy composite, samples were processed with 0% (neat epoxy), 5%, 10%, and 15% volume fraction (V_f) of filler. For each sample, the epoxy resin was heated on a hot plate set to 100°C for ten minutes in order to lower the viscosity and improve fiber dispersion (Figure 2-3). Next, a magnetic stir bar was added into the resin and stirred by creating a small vortex on the hotplate.

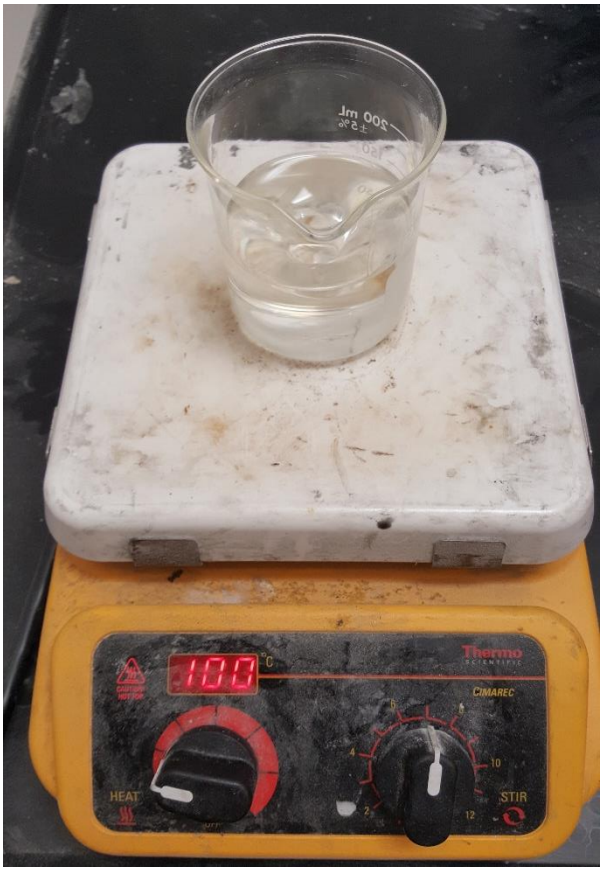

Figure 2-3: Photograph Epoxy resin and glass fiber mixture in 300mL beaker placed on a hot plate during magnetic stir bar mixing

The glass fiber was slowly poured into the resin and was stirred for fifteen minutes with the hotplate set to 100°C. To remove any air bubbles trapped during the stirring, the mixture was placed in a room-temperature vacuum chamber and degassed continuously at 30 inHg for typically fifteen minutes. However, when increasing the volume fraction of filler, degassing time tended to increase, at times taking up to an hour. In these cases, prolonged degassing caused sample cooling, increasing the viscosity of the mixture, and making complete bubble removal quite difficult. When this occurred, the mixture was reheated in a 900-watt microwave oven for thirty seconds and then placed back in the vacuum until complete degassing had been achieved.

Once removed from the vacuum chamber, the mixture was allowed to cool to room temperature while maintaining uniform fiber dispersion with hand-stirring. Next, hardener was added and stirred by hand for approximately twenty minutes or until the mixture had gelled sufficiently to prevent the settling of the glass fibers. It is important to note that adding the hardener to heated resin can significantly reduce the epoxy's gel time, making homogeneity of the sample challenging to achieve.

The mixture was then poured into a fresh PMMA mold formed from two rectangular PMMA sheets, which were separated by spacers. The parts were fastened at both ends of the mold with either machine screws or standard binder clips, then sealed at the bottom with duct tape, as shown in Figure 2-4 and Figure 2-5.

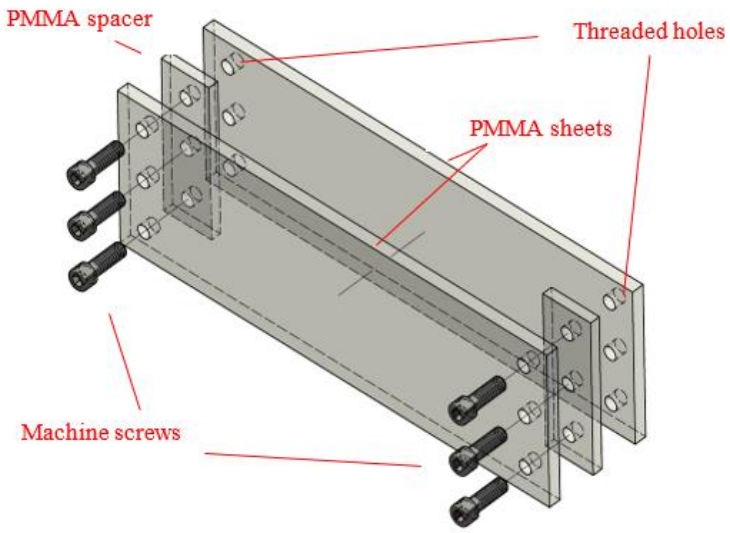

Figure 2-4: Schematic of a mold used for casting glass-filled epoxy composites

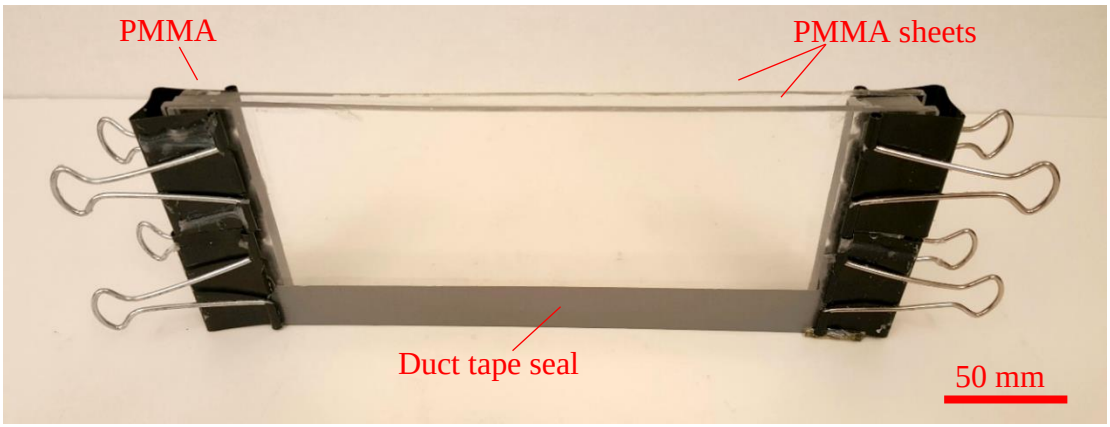

Figure 2-5: Specimen mold formed from two PMMA spacers sandwiched between two PMMA sheets. Sealed on the bottom with duct tape

No mold release agent coating was used to ensure a smooth surface finish and good optical transparency. Finally, the mixture was allowed to cure for a minimum of two days.

2.3 Optical Transparency

Initially, optical transparency was not present due to the mismatch in the refractive indices of uncured/liquid epoxy and filler, but as the curing progressed, the refractive index of the epoxy approached that of the glass fibers resulting in a transparent composite. To record this change in transparency, a simple time-lapse camera setup (schematic shown in Figure 2-6) was utilized, and the Auburn logo was used as a reference image.

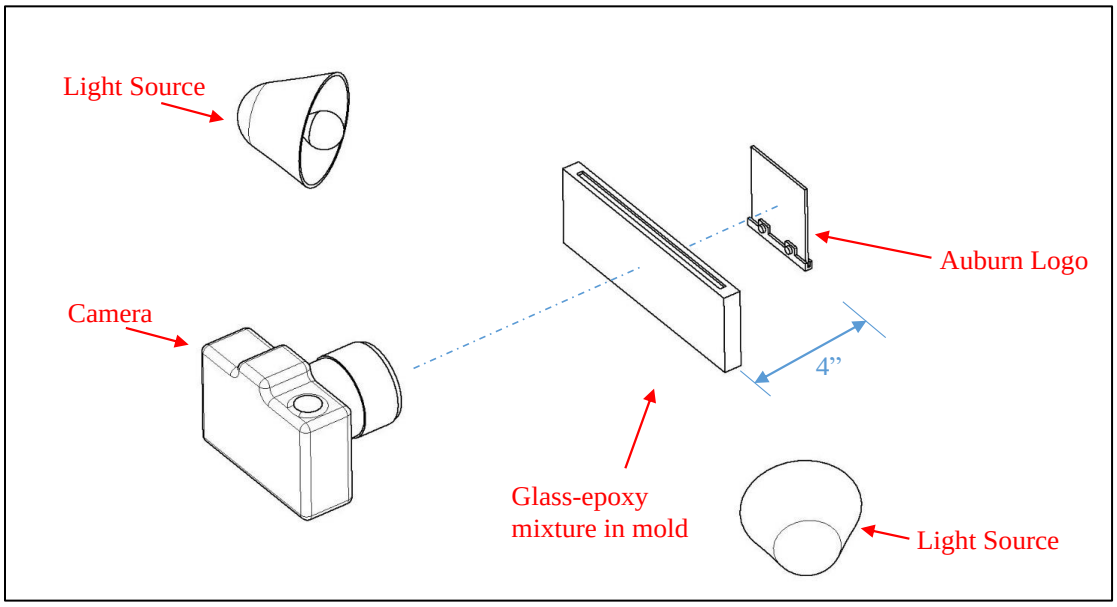

Figure 2-6: Schematic of the optical evolution imaging setup

In this setup, an epoxy mixture was poured into a PMMA mold and placed four inches in front of the Auburn University logo. Figure 2-7 shows the optical evolution of a 10% volume fraction sample at intervals from t=0 (immediately after being poured into the mold) until completion at nine hours.

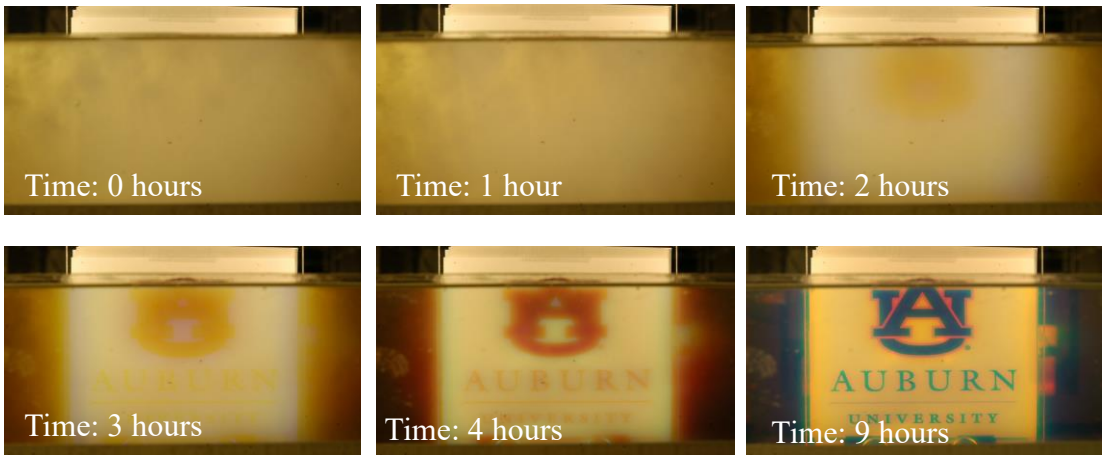

Figure 2-7: Evolution of optical transparency during the curing process of glass-filled epoxy material (10% volume fraction)

In the first hour of curing, a minimal increase in optical transparency can be observed. After 1-2 hours, the Auburn logo begins to be distinguishable from the surrounding white background. After about three hours into the curing process, the optical transparency rapidly improves up until nine hours, after which point the mixture has fully cured, and no further improvements occurred. A comparison between an unobstructed Auburn logo, where no epoxy mixture or mold is present, and the fully cured 10% glass-fiber filled epoxy sample is shown in Figure 2-8 and Figure 2-9.

Figure 2-8: Photograph of Auburn logo used in optical evolution imaging with glass-fiber epoxy mold removed. Shown for comparison

Figure 2-9: Optical transparency of fully cured glass-filled epoxy material (10% volume fraction, Time = 9 hours)

2.4 Mechanical/Physical Properties

In order to gain an initial understanding of the physical and elastic properties of each composite, ultrasonic measurements were carried out. To determine the wave speeds, an Olympus™ EPOCH 600 oscilloscope ultrasonic device (Figure 2-10) was used to perform pulse-echo measurements. Longitudinal wave speeds were evaluated using a V106-RM transducer (10MHz) connected to the oscilloscope and coupled to the sample with propylene glycol. Shear wave speeds were measured with a V-154-RM transducer (2.27MHz) and a shear gel couplet.

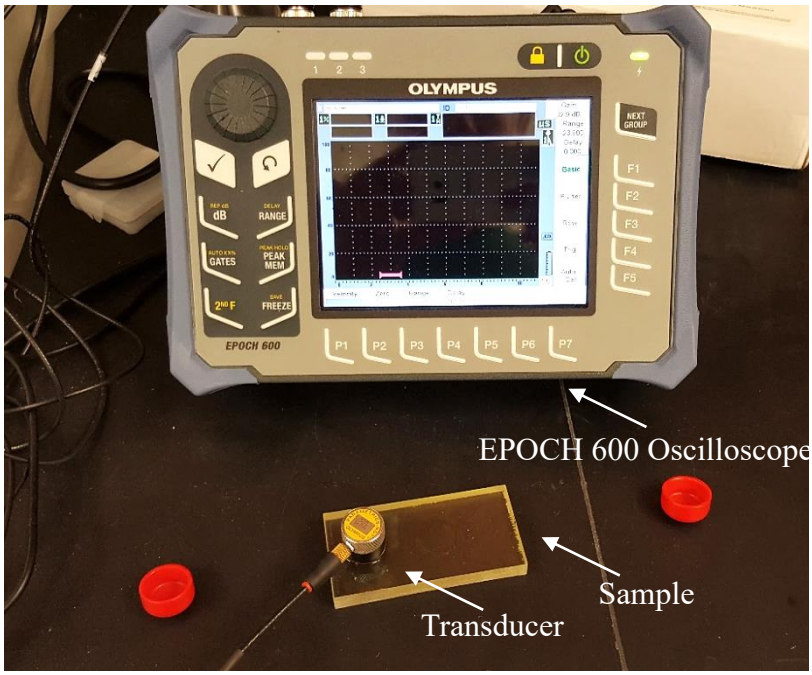

Figure 2-10: Photograph of oscilloscope and transducer used to perform ultrasonic measurements

Each sample was tested at several locations on the surface, and the measured wave speeds were averaged. From these values and material density measurement, the

elastic modulus and Poisson's ratios were calculated using the following expressions for C_l and C_s:

$$C_s = \sqrt{\frac{E_d}{2\rho(1+v_d)}} \quad 2\text{-}1$$

$$C_l = \sqrt{\frac{E_d(1-v_d)}{\rho(1+v_d)(1-2v_d)}} \quad 2\text{-}2$$

The measured physical and elastic properties for each composite are shown in :

Table 2-2:

Table 2-2: Physical and elastic properties of the glass-filled epoxy composite at 0%, 5%, 10% and 15% volume fractions

V_f(%)	Density ρ (kg/m^3)	Longitudinal wave speed C_1 (m/s)	Shear wave speed C_2 (m/s)	Elastic modulus E_d (GPA)	Poisson's ratio υ_d
0%	1125 ± 12	2440 ± 10	1125 ± 5	3.96	0.36
5%	1226 ± 12	2480 ± 12	1170 ± 8	4.67	0.35
10%	1285 ± 11	2534 ± 6	1240 ± 8	5.31	0.35
15%	1375 ± 8	2568 ± 11	1282 ± 4	6.04	0.34

It is evident that with respect to increased volume fraction, the elastic modulus increases monotonically, indicating an increase in stiffness as more glass fibers are added.

CHAPTER 3: OPTICAL MEASUREMENTS AND ANALYSIS

This chapter explains the working principle of photoelasticity, evaluation of the stress-optic constants of birefringent materials, and the application of photoelasticity to fracture mechanics. The glass-fiber reinforced composites are shown to exhibit birefringent behavior, and the experimental setup for optical characterization is discussed. The resulting stress-optic constants of the composites are then measured and tabulated. Lastly, the data extraction from photoelastic images and two methods for stress intensity factor (SIF) evaluation are described.

3.1 Birefringent Materials

Photoelasticity is a full-field, nondestructive experimental technique used to measure the stress distribution in a material based on the principle of optical birefringence. A material is said to be birefringent when light incident on the material is split into two rays of different speeds and paths. This phenomenon, also known as "double refraction," occurs when a material's refractive index differs with respect to the polarization and direction of incident light, and is commonly found in optically anisotropic materials, such as quartz or calcite.

Take, for example, a piece of crystal in Figure 3-1 where light is incident on the surface of material 2 at an angle *i*.

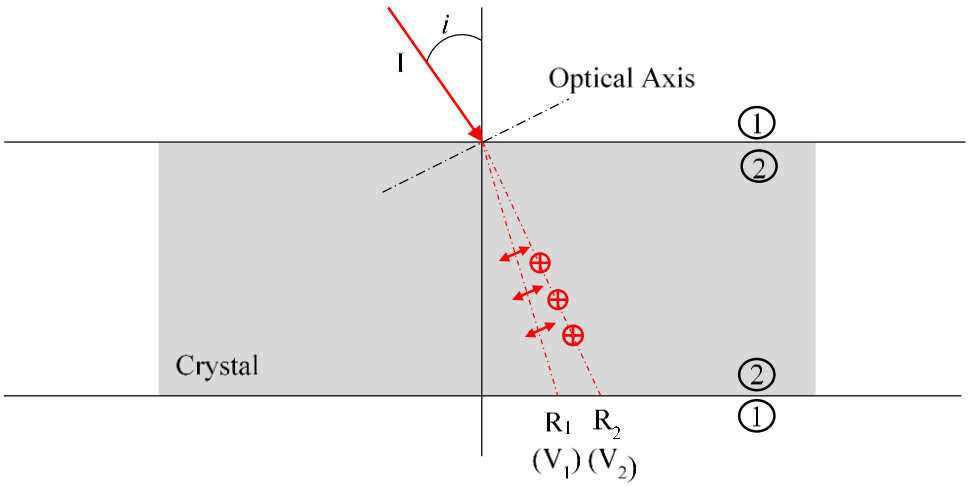

Figure 3-1: Propagation of light through birefringent materials

As the incident wave crosses the 1-2 interface, two refracted waves, R_1 and R_2 are formed, taking slightly different paths. The resulting waves become linearly polarized in directions mutually perpendicular to each other, as indicated by the ↔ and ⊕ symbols representing in-plane and out-of-plane oscillations, respectively. Additionally, the two refracted waves travel at different velocities, V_1 and V_2, where one wave follows Snell's law, $\frac{\sin\theta_1}{\sin\theta_2} = \frac{V_1}{V_2} = \frac{\lambda_1}{\lambda_2}$, and is referred to as the "ordinary ray" while the other does not follow Snell's law and is referred to as the "extraordinary ray". Birefringence can be observed on a piece of quartz crystal resting on notebook paper in Figure 3-2.

Figure 3-2: Birefringence in a quartz crystal

For a 2D photoelastic material where the optical axis is normal to the two faces of the medium and the incident rays are perpendicular to the optical axis, both the ordinary and extraordinary rays will travel along the same path, but at different velocities. In this case, the medium acts as an optical retarder and imposes a phase difference Δ between the two rays. Assuming a constant thickness, isotropic materials subjected to in-plane loading (the principal stresses are perpendicular to the direction of light propagation), the magnitude of the phase difference is given by the stress-optic law:

$$\Delta = \frac{2\pi h}{\lambda} C(\sigma_1 - \sigma_2) \qquad 3\text{-}1$$

where Δ is the induced phase shift, C is the stress-optic constant, h is the thickness of the medium, λ is the wavelength, and σ_1 and σ_2 are the first and second principal stresses.

3.2 Principles of Photoelasticity

A polariscope is an optical instrument used for extracting birefringence induced optical shifts and hence the embedded information about the stress field in a photoelastic material/model subjected to external loads. Two types of polariscopes are commonly used in experimental stress analysis. The first and most basic is the plane polariscope, which consists of the combination of a light source and two polarizers arranged on opposite sides of the photoelastic material. The second, called a circular polariscope, consists of a plane polariscope with two additional wave plates. As its name suggests, a circular polariscope produces circularly polarized light to interrogate the specimen.

For both types of polariscopes, the relative orientation of the two polarizers determines whether it is defined as either a “dark field” or “light field”. If both polarizers are oriented with the polarization axis in the same direction, a “light field” polariscope is formed, and light passing through an unstressed sample will be observable. Alternatively, if the polarizers are oriented perpendicular to each other, an unstressed sample placed in the polariscope will appear dark and is called a “dark field” polariscope. In this work, the latter setup was used.

3.2.1 Plane Polariscope

In a plane polariscope, light passes through the first polarizer, called the “polarizer”, then through a birefringent specimen (under stress) and out through the second polarizer, the “analyzer”. If no stress is applied to the specimen, the light rays pass through the material undisturbed, and a “dark field” is produced due to the

perpendicular orientation of two polarizer axes. However, if the model is stressed, the refractive indices of the material in the plane of polarization shift relative to each other, creating a change in velocity and retardation between the two orthogonal light rays formed through the principle of birefringence.

A detailed analysis of light propagation through the polariscope shows that the intensity of light emerging from the analyzer of a plane polariscope is given by [25]:

$$I = K\ sin^2\ 2\alpha\ sin^2\frac{\Delta}{2} \tag{3-2}$$

where α is the angle between the principal stress direction of the model and the axis polarization of the polarizer and Δ is previously given by equation 3-1.

It is clear from equation 3-2 that the intensity of light at any arbitrary point will be zero (I = 0) under two scenarios; when $sin^2\ 2\alpha$ = 0 and $sin^2\frac{\Delta}{2}$ = 0. Thus, for a stressed model viewed in a plane polariscope, two sets of overlapping optical interference fringes occur, one known as 'isoclinics' and the other as 'isochromatics'.

Isoclinics represent contours of constant principal stress orientation and are formed when:

$$sin^2 2\alpha = 0 \tag{3-3}$$

Isochromatic fringes, representing contours of constant principal stress difference magnitudes, occur when:

$$\Delta = \sigma_1 - \sigma_2 = N\frac{\lambda}{CB} \tag{3-4}$$

where N denotes the fringe order (N = 0, ±1, ±2, …).

3.1.2 Circular Polariscope

However, if only isochromatic fringes are desired, a pair of quarter-wave plates can be used to modify the plane polariscope into a "circular polariscope". Quarter-wave plates are a subset of optical elements called "wave plates" and are constructed from a permanently birefringent film/sheet to introduce a known, constant phase shift between the refracted rays in the field of view. A ray of plane-polarized light incident on a wave plate is resolved into two mutually perpendicular components traveling at different speeds. The axis of the faster component is termed the "fast axis", while the slower component is said to travel along the "slow axis".

Since these two components travel through the waveplate at different velocities, they will emerge at different times; thus, a relative phase shift, Δ, is introduced. In the case of a quarter-wave plate, Δ is equal to 90°, or a quarter of a wavelength.

Additionally, using quarter-wave plates converts linearly polarized light to circularly polarized light as it enters the stressed model. Fringe patterns formed by linear polariscopes are dependent on the orientation of the polarizer axes relative to the optical axes of the birefringent material. If a direction of the optical axes of the material aligns with the orientation of the polarizer, light will pass through unstressed, virtually unaffected, but for some intensity attenuation. In this case, no relative phase change will occur, and fringes will not be formed (or, a constant fringe with infinite spacing will be formed). Thus, by placing two quarter-wave plates on either side of the specimen in opposite orientations (fast and slow axes of the two quarter-wave plates line up as shown) at 45° relative to the polarizer axis, a circular polariscope (Figure 3-3) can be constructed,

and fringe formation becomes dependent solely on the phase shift created by the birefringent material.

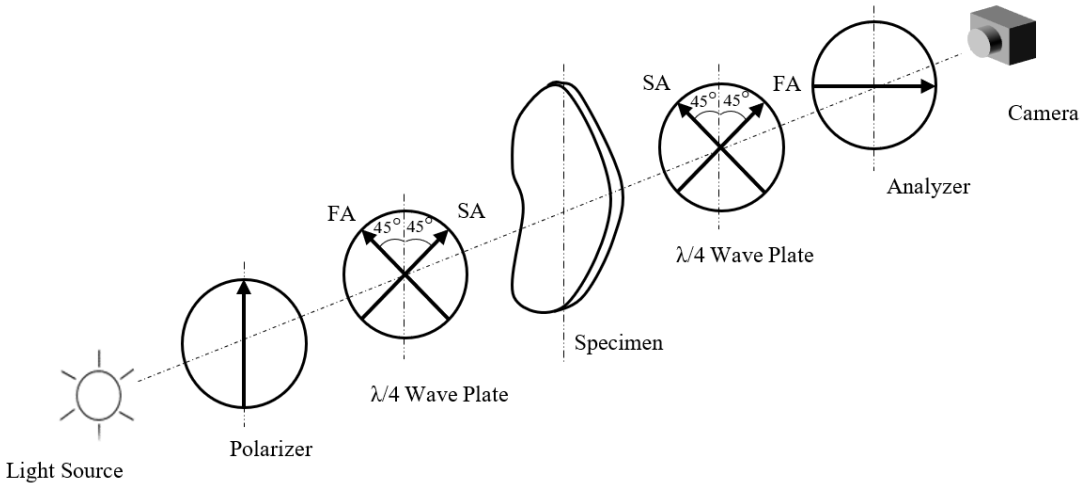

Figure 3-3: Schematic of a circular dark-field polariscope

3.3 Evaluation of Photoelastic Constants

Upon initial investigation of the samples using the polariscopes discussed, the transparent composites were found to exhibit birefringent properties, making it feasible to mechanically study the fracture mechanics of the material using transmission photoelasticity. Figure 3-4 shows two pictures of the same 10% V_f glass-filled epoxy composite sample placed in a circular dark-field polariscope with a symmetric four-point bending setup. Figure 3-4 (a) shows an image taken before loading (light areas indicate residual stresses introduced through sample machining and prior testing), and thus a dark-field can be observed. As the sample was loaded, isochromatic fringes emerged and an image of the 10% V_f under an imposed load (P; Figure 3-5) of approximately 500N is shown in Figure 3-4 (b):

a)

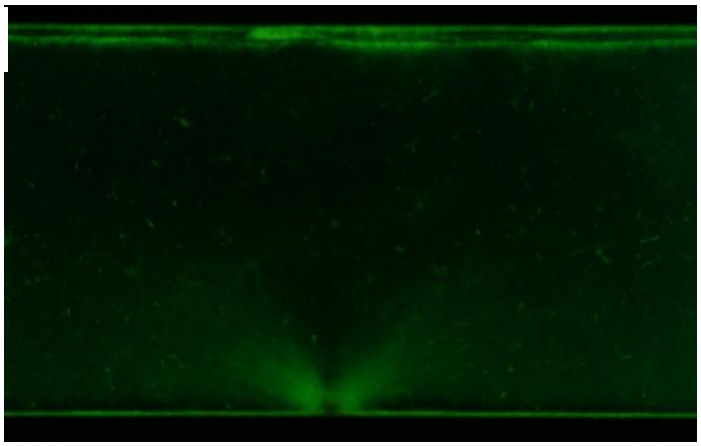

b)

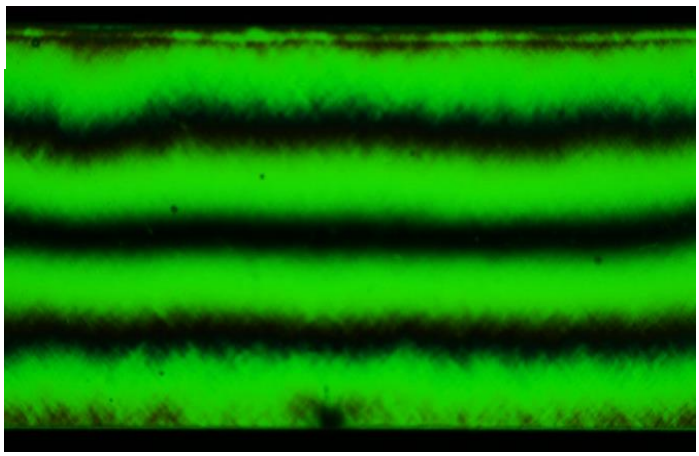

Figure 3-4: Glass-filled (10% V_f) epoxy sample viewed through circular polariscope in a) unloaded and b) loaded conditions

First, the stress-optic constant (f_σ) for each material composition was determined using a standard dark-field circular polariscope with a green filter to form isochromatic fringes. Each sample was subjected to symmetric four-point bending, as can be seen in the schematic in Figure 3-5. Load data was recorded by an Instron 4465 machine and the resulting fringes were captured using time-lapse photography (Figure 3-6). The two fringe patterns shown in Figure 3-7 are typical for a neat and 10% V_f sample at a 600 N

load within the pure bending zone of the specimen. Evidently, the fringes of the neat epoxy sample are well-formed and relatively smooth. On the other hand, due to the superposition of imposed stress field and random residual stresses, the fringes in the glass-filled composite exhibit an uneven appearance. During the curing process, a mismatch in the Coefficient of Thermal Expansion between epoxy and glass-filler produces microscopic residual stresses which, as a result of heterogeneity of the material, are random in nature.

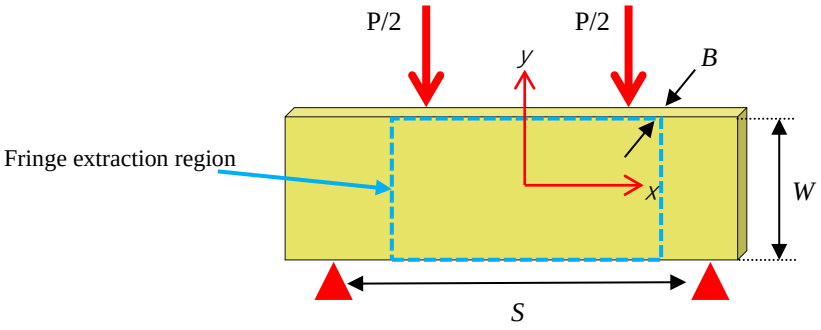

Figure 3-5: Symmetric four-point bending diagram

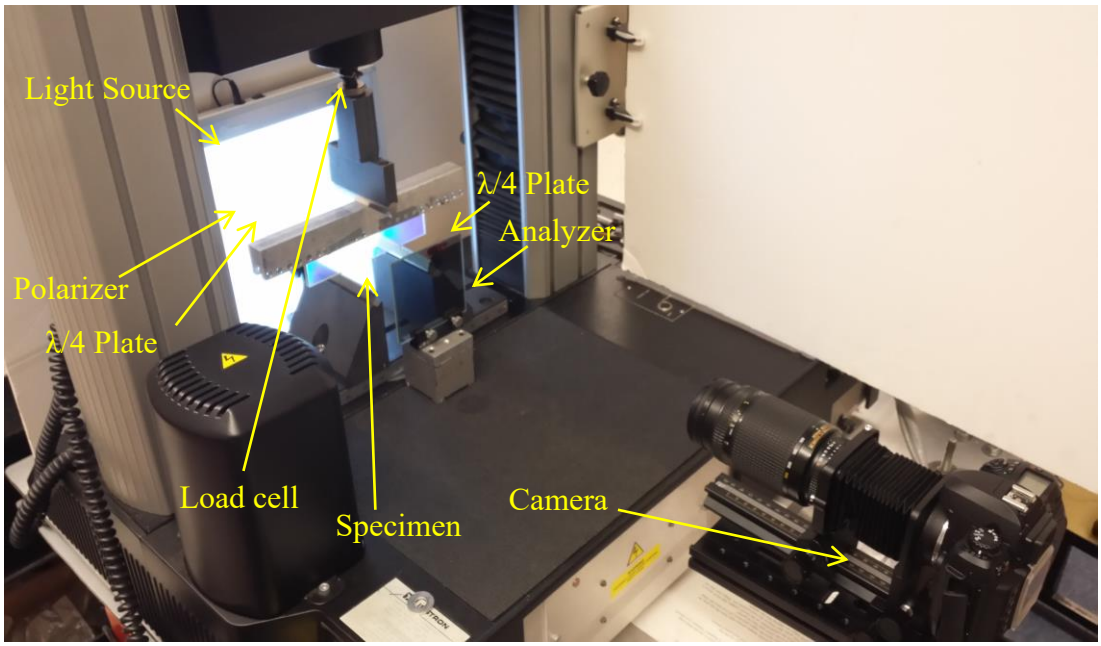

Figure 3-6: Experimental setup consisting of a circular dark-field polariscope, Instron 4465 machine, and DSLR camera fitted with a green filter.

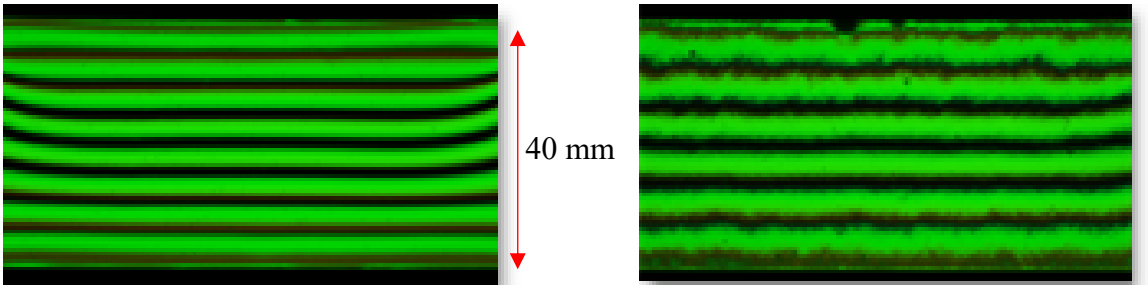

Figure 3-7: Isochromatics in neat epoxy (left) and 10% V_f glass-filled epoxy (right) obtained from a symmetric four-point bend test using a circular dark-field polariscope (P = ~500N)

To obtain the stress-optic constant (f_σ) from these isochromatics, elementary beam theory, in conjunction with the stress-optic law, must be used. The stress-optic law states,

$$\sigma_1 - \sigma_2 = \frac{N f_\sigma}{B} \tag{3-5}$$

where σ_1 and σ_2 are the two principal stresses, N is the fringe order, f_σ is the stress-optic constant, and B is the sample thickness. However, with a four-point symmetrical loading set-up, σ_y and τ_{xy} in the region of interest are zero. Therefore,

$$\sigma_1 - \sigma_2 = \sigma_x \tag{3-6}$$

and from the beam theory,

$$\sigma_x = \frac{My}{I} \tag{3-7}$$

where M is the bending moment in the region of interest, y is the distance from the neutral axis, and I is the moment of inertia of the specimen then,

$$f_\sigma = \frac{MyB}{NI} \tag{3-8}$$

Using this expression, f_σ was be determined for each composite by assigning orders to each fringe and measuring the distance from the central (N = 0) fringe, as shown in Figure 3-8. Measurements were made for each fringe at various load levels and averaged for each composite. The resulting f_σ values are shown in Table 3-1.

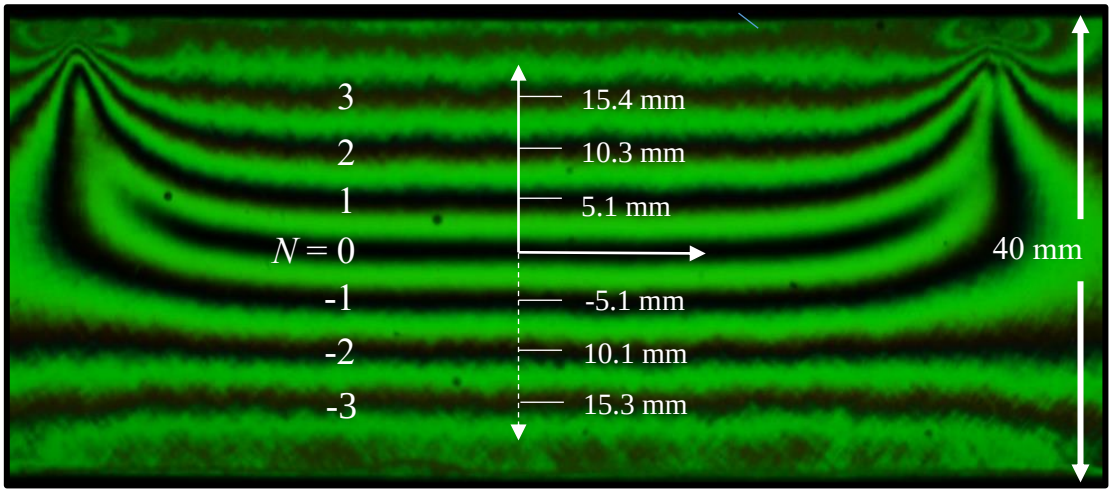

Figure 3-8: Fringe orders and neutral axis distances values of isocromatics obtained from a symmetric four-point bend test using a circular dark-field polariscope

Table 3-1: Experimentally obtained stress-optic constants (f_σ) for neat and glass-filled epoxy

Filler % (V_f)	Stress-optic constant (f_σ)
0%	19.0 ± 0.3
5%	22.9 ± 0.2
10%	28.4 ± 0.4
15%	38.5 ± 0.2

Clearly, as the volume fraction increases, there is a monotonic increase in the stress-optic constant. Higher f_σ values can make photoelastic evaluation more difficult as the number of fringes formed at a load decreases, providing either fewer data points to analyze or, in the case of crack tip stresses, smaller radial extent of fringes. Typically, this issue can be adverted by using high loads if sample breakage is not a concern or

using fringe multiplying methods [25]. Figure 3-9 demonstrates this behavior where fringe patterns are shown for each composite at approximately 500 N load.

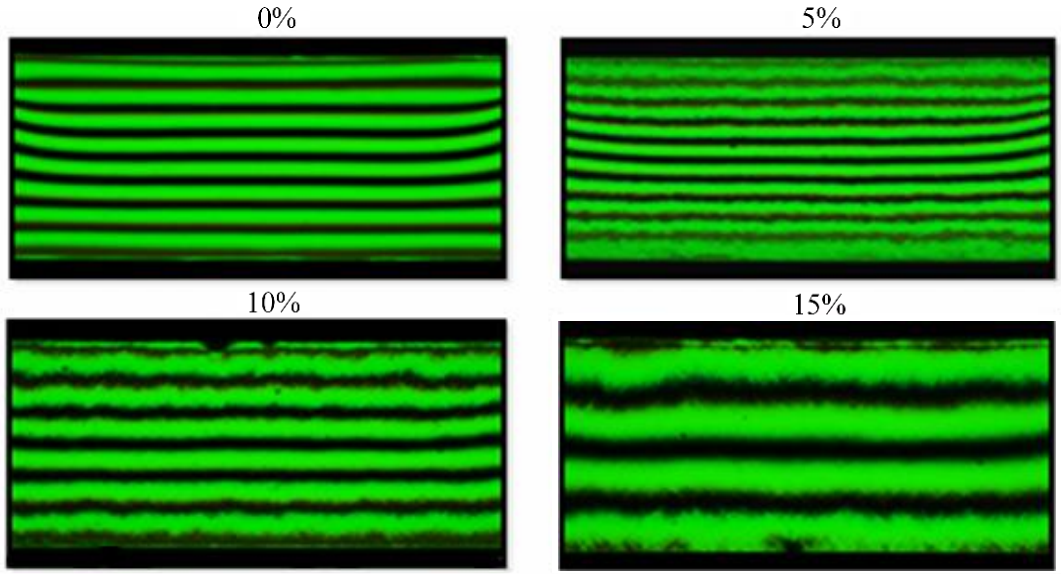

Figure 3-9: Isochromatic fringe patterns for 0%, 5%, 10% and 15% (volume fraction) glass-filled composites at similar loads (approximately 500 N)

3.4 Photoelasticity Applied to Fracture Mechanics

The characterization of materials presented in this work is primarily focused on the study of the fracture behavior. As such, fractures tests under both static and dynamic loading conditions were performed. Utilizing the birefringent behavior of the glass-filled epoxy composite, a photoelastic evaluation of the *critical* stress intensity factors (K_{Icr}), for quasi-static loading, as well as mode-I and mode-II Stress Intensity Factors (SIF) histories under dynamic loading were conducted.

Photoelasticity is a particularly useful method for this study, as the isochromatic fringes formed around a crack tip provide sufficient data for the evaluation of these fracture parameters and can be measured with relative ease.

3.4.1 Digitization of Isochromatic Fringe Data

The first step in the analysis of images obtained from photoelastic testing is the measurement relevant fringe information such as distance from the crack tip, fringe order, and angle relative to the crack axis, from a selection of points in the region of interest around the crack tip (Figure 3-10).

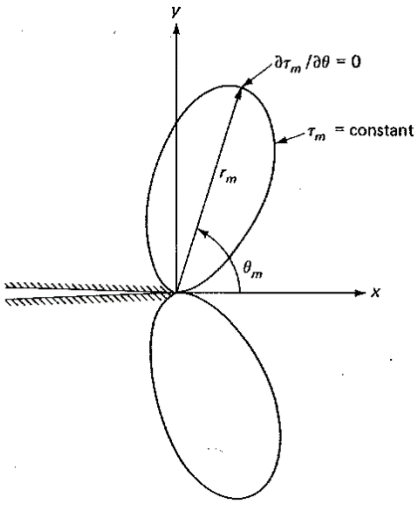

Figure 3-10: Characteristics of an isochromatic fringe occurring around a crack tip [25]

When performing an analysis using a relatively simple approach, such as the Smith and Schoedl method (described in the next section), this measurement becomes somewhat trivial as data points are only considered along the θ=90° line. However, when increased accuracy is desired, methods that employ many data points should be used. The process of data point selection can be aided by a technique called "Fringe Thinning" where the thickness of the isochromatic fringes can be reduced through a variety of image processing methods. This becomes especially useful when many data points are desired, ensuring a consistent position within the fringe is selected across all values of θ.

In this work, MATLAB was used for both image processing and data collection. As a first step, images of isochromatic fringe patterns were viewed in MATLAB, and, using the "Image Processing Toolbox", masks were applied using RGB and intensity filters in order to isolate a "fringe skeleton" representing the darkest locations for each fringe. An example result of this fringe thinning technique using MATLAB is shown below in Figure 3-11 and an overlay of an original (unprocessed) image and the generated "fringe skeleton" is shown in Figure 3-12:

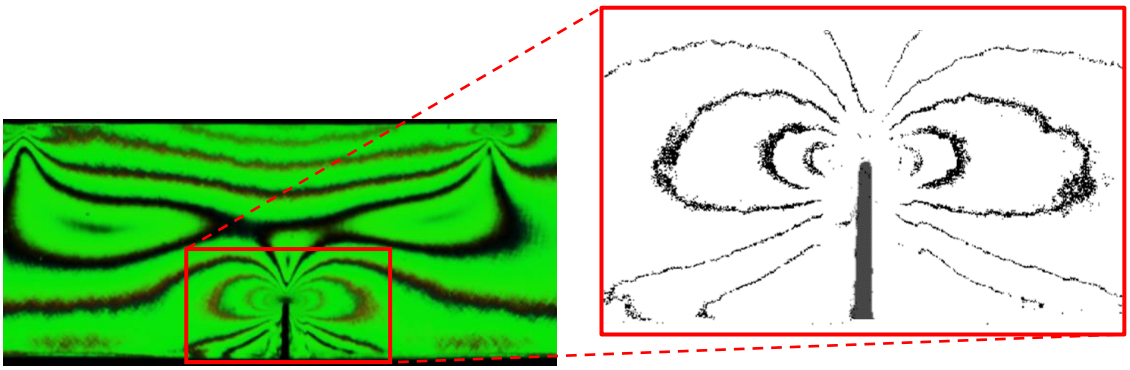

Figure 3-11: Isochromatic fringes in 5% V_f sample under quasi-static symmetric four-point loading. Unprocessed image (left) and image with "fringe thinning" (right).

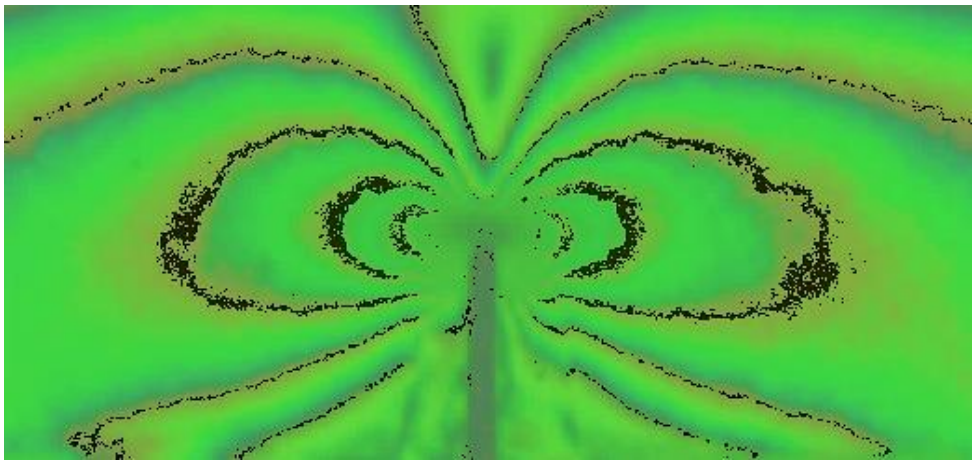

Figure 3-12: Overlay of an original (unprocessed) image and the generated "fringe skeleton"

Clearly, when evaluating the fringes along the "fringe skeleton," the effective thickness of each fringe is minimized, reducing possible data extraction errors that could arise from an inconsistent selection of the fringe centerline.

3.4.2 Evaluation of Stress Intensity Factors (SIFs)

In this work, a photoelastic evaluation of stress intensity factors (SIFs) was performed using two techniques of differing complexity. First, the Smith and Schroedl method [26], a relatively simple two-parameter analysis, was used to determine the feasibility of using photoelasticity for stress intensity factor evaluation with the glass-filled epoxy composite. In this method, K_I values are determined by selecting points on two different fringes at 90º from the crack tip, as shown in Figure 3-13.

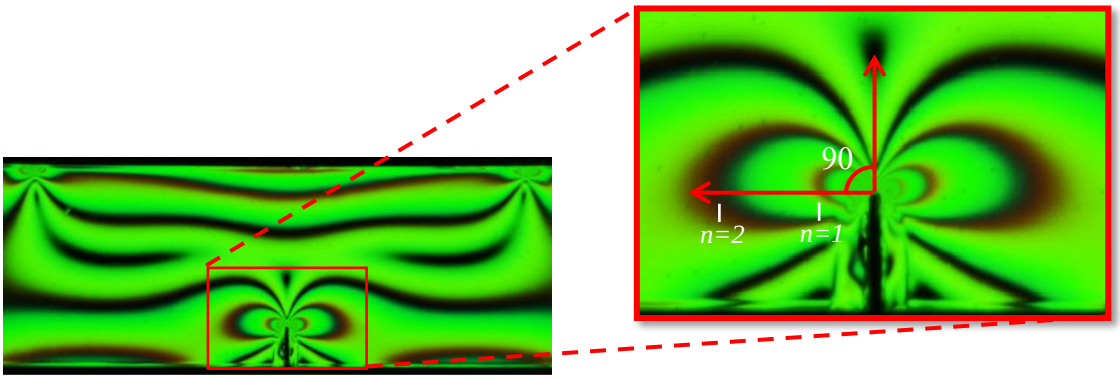

Figure 3-13: Diagram of point selection used to evaluate K_I using the Smith and Schroedl method

To do this, the distance from the crack tip along with the fringe order of the two points are recorded and K_I is determined using equation 3-9.

$$K_I \approx \sqrt{\pi r}\left[\left(2\sqrt{2}\tau_{max}\right) - \sigma_o\right] \qquad 3\text{-}9$$

where, K_I and σ_0 become the only unknowns, and thus two equations can be solved simultaneously.

Once photoelastic evaluation proved successful, a more robust over-deterministic nonlinear least-squares analysis approach was used to determine the mode-I and mode-II stress intensity factors, K_I and K_{II}. After generating a fringe skeleton, data points were selected from the fringes around the crack tip. Typically, points from three distinct fringes were considered with approximately 80-100 data points selected in total. An example of this point selection from a 5% V_f sample under quasi-static symmetric four-point loading is shown in Figure 3-14(a) (original image) and Figure 3-14(b) (fringe skeleton).

a)

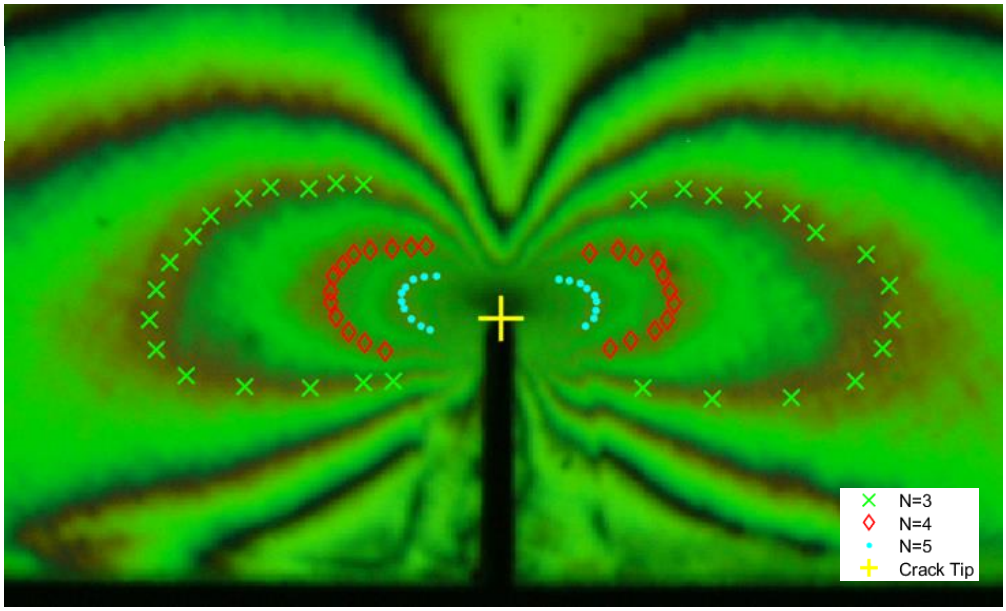

b)

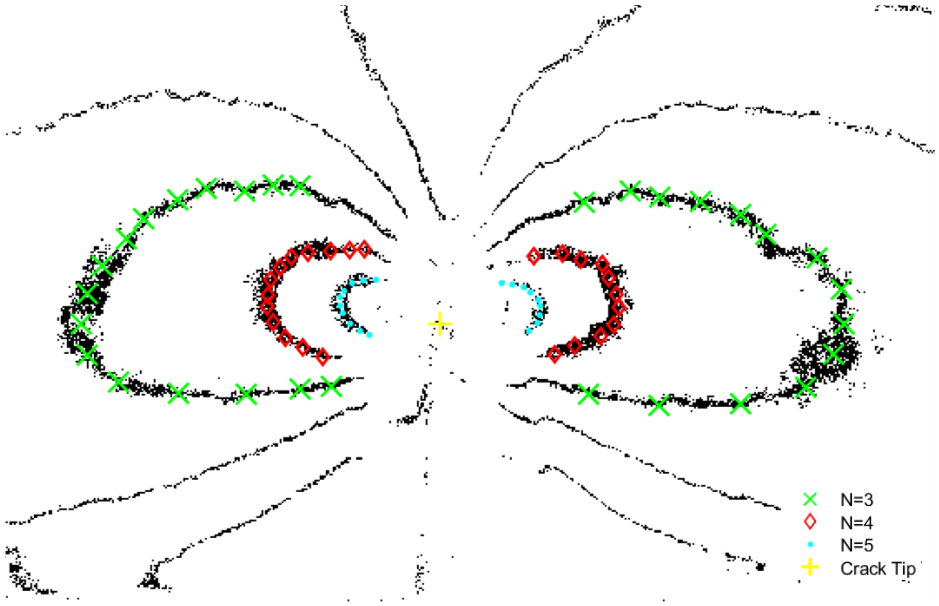

Figure 3-14: Example of point selection of isochromatic fringe data. Identical data sets overlayed on both the original image (a) and fringe skeleton (b) shown for comparison.

In order to evaluate the SIFs, an over-deterministic least-squares analysis was performed based on the following asymptotic representation of the stresses around the crack tip [25]:

$$\left(\frac{Nf_{\sigma}}{2h}\right)^2 = \left(\frac{\sigma_{yy}-\sigma_{xx}}{2}\right)^2 + \tau_{xy}^2 = D^2 + T^2 \tag{3-10}$$

where,

$$\begin{aligned} D &= \frac{\sigma_{yy}-\sigma_{xx}}{2} \\ &= \sum_{n=0}^{i}\left(n-\frac{1}{2}\right)A_n r^{\left(n-\frac{1}{2}\right)} sin\theta\, sin\left(n-\frac{3}{2}\right)\theta \\ &\quad + \sum_{m=0}^{i} B_m r^m \left[m\, sin\theta\, sin\, m\theta + cos\, m\theta\right] \\ &\quad - \sum_{n=0}^{i} C_n r^{n-\frac{1}{2}}\left[\left(n-\frac{1}{2}\right) sin\theta\, cos\left(n-\frac{3}{2}\right)\theta + sin\left(n-\frac{1}{2}\right)\theta\right] \\ &\quad - \sum_{m=0}^{i} D_m r^m\, sin\theta\, cos(m-1)\theta \end{aligned} \tag{3-11}$$

$$\begin{aligned} T &= \tau_{xy} \\ &= -\sum_{n=0}^{i}\left(n-\frac{1}{2}\right)A_n r^{\left(n-\frac{1}{2}\right)} sin\theta\, sin\left(n-\frac{3}{2}\right)\theta \\ &\quad - \sum_{m=0}^{i} B_m r^m \left[m\, sin\theta\, cos\, m\theta + sin\, m\theta\right] \\ &\quad + \sum_{n=0}^{i} C_n r^{n-\frac{1}{2}}\left[cos\left(n-\frac{1}{2}\right)\theta - (n-\frac{1}{2})sin\theta\, sin\left(n-\frac{3}{2}\right)\theta\right] \\ &\quad - \sum_{m=0}^{i} D_m r^m \left[m\, sin\theta\, sin(m-1)\theta\right] \end{aligned} \tag{3-12}$$

and A_n, B_m, C_n, D_m are unknowns which are determined using an over-deterministic least squares analysis based on equation 3-10 such that:

$$D^2 + T^2 - \left(\frac{Nf_\sigma}{2h}\right)^2 = 0 \qquad 3\text{-}13$$

Once evaluated, the values the stress intensity factors, K_I and K_{II}, are determined from A_0 and C_0 by:

$$K_I = \sqrt{2\pi}A_0 \qquad 3\text{-}14$$

$$K_{II} = \sqrt{2\pi}C_0 \qquad 3\text{-}15$$

CHAPTER 4: QUASI-STATIC CRACK-INITIATION AND FRACTURE

In this chapter, material preparation for static fracture testing of neat and glass-filled epoxy composites is described. Mode-I stress intensity factors are determined initially from load histories measured with an Instron testing machine. A polariscope was then added to the setup, and new, identical samples were loaded quasi-statically and evaluated using photoelastic fringe data in conjunction with an over-deterministic least-squares analysis. Results from both methods of evaluation were compared and found to match closely.

4.1 Material Preparation

Glass-filled epoxy sheets with 0%, 5%, 10% and 15% filler volume fractions were machined into specimens of dimensions 44 mm x 10 mm x 4.3 mm. A notch of length 2.5 mm (a/W = 0.25) was introduced at the mid-span of each specimen with a diamond impregnated circular saw (Buehler wafering blade 114244). To prevent a circular crack front during cutting, each sample was raised and lowered relative to the circular saw at the maximum cutting distance. Lastly, each sample was sharpened with a fresh razor blade to ensure a sharp pre-crack (Figure 4-1). The figure clearly shows the end of the cut due to the circular saw and the tip of the crack by scoring with the razor blade. Evidently, one order reduction in the root radius is achieved using the razor blade.

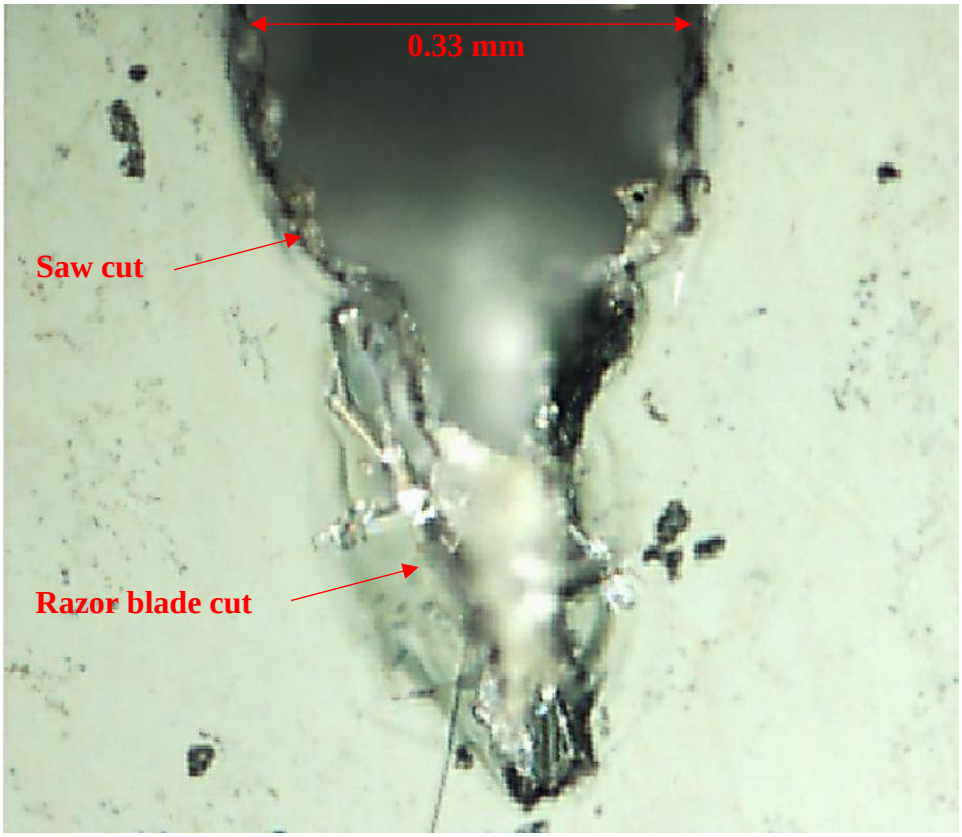

Figure 4-1: Crack notch machined with diamond impregnated circular saw and sharpened with a razor blade

4.2 Loading Configuration and Initial Results

In order to gain an initial understanding of this material's failure characteristics, quasi-static symmetric three-point bend fracture tests were performed to determine the crack initiation toughness (K_{Icr}) of each sample compared to the neat epoxy. A schematic of the experimental setup is shown below in Figure 4-2.

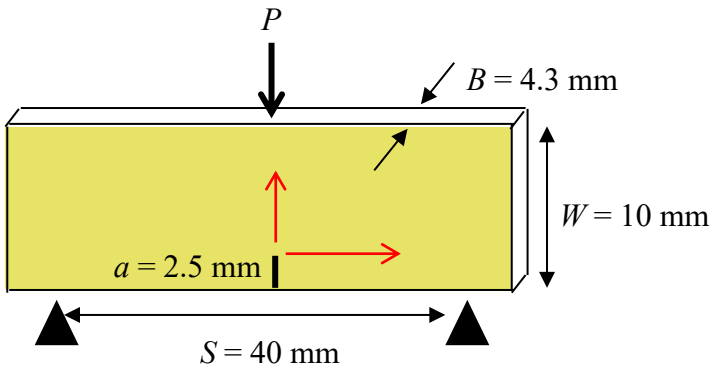

Figure 4-2: Quasi-static symmetric three-point bend fracture test schematic

An Instron 4465 testing machine was used to load the samples in a symmetric three-point bending configuration. The samples were placed on two anvils with a span of 40 mm and loaded at a rate of 0.25 mm/min until fracture, at which point the failure load (P_{max}) was recorded. Displacement as a function of load for each V_f is shown in Figure 4-3:

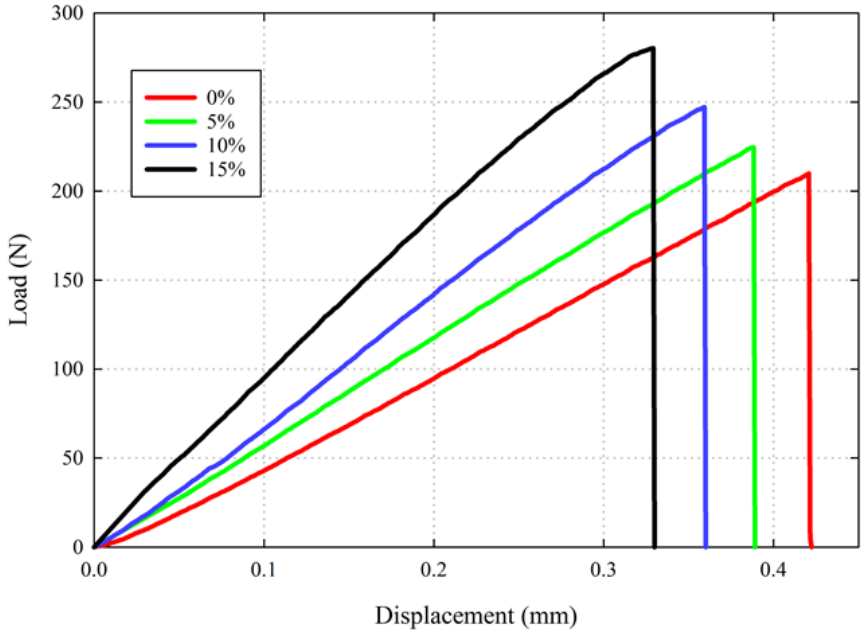

Figure 4-3: Load vs displacement for 0%, 5%, 10%, and 15% volume fraction glass-filled epoxy composites under quasi-static symmetric three-point bending

As the volume fraction of the filler increased, an increase in the material's stiffness, as well as failure load, was observed. The fracture response in terms of load v. load-point deflection in each case is nominally brittle with a modest nonlinearity evident in the 10% and 15% V_f cases, attributed to a higher prevalence of crack tip bridging and shielding effects. Repeatability of the results was ensured by conducting multiple experiments at each filler volume fraction. Good reproducibility was observed in all cases and can be seen in the load v. displacement graphs for the 10% V_f case in Figure 4-4.

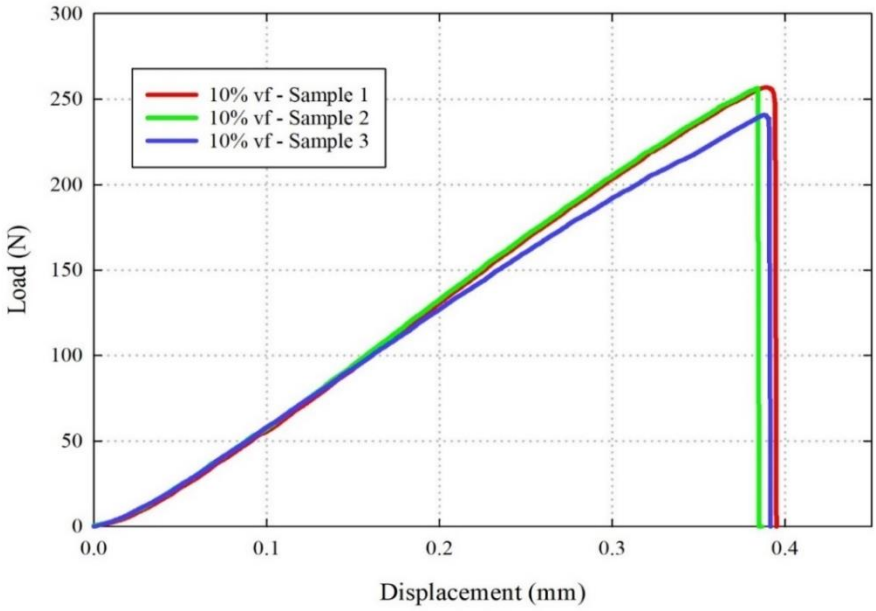

Figure 4-4: Quasi-static three-point bend test repeatability of 10% (V_f) glass-filled epoxy composite

The K_{Icr} values were computed using equation 4-1, and the results are shown below in Table 4-1:

$$K_{Icr} = \frac{\frac{P_{max}}{B\sqrt{W}}\left(3\frac{s}{W}\sqrt{\frac{a}{W}}\right)}{2\left(1+2\frac{a}{W}\right)\left(1-\frac{a}{W}\right)^{1.5}}\left[1.99-\frac{a}{W}\left(1-\frac{a}{W}\right)\left\{2.15-3.93\left(\frac{a}{W}\right)+2.7\left(\frac{a}{W}\right)^{2}\right\}\right] \qquad 4\text{-}1$$

Table 4-1: Experimentally measured quasi-static crack-initiation toughness (K_{Icr}) values for glass-filled epoxy composites. (% increase of K_{Icr} values measured with respect to 0% V_f case)

V_f (%)	K_{Icr} (MPa√m)	% Increase
0%	2.24 ± 0.12	-
5%	2.35 ± 0.08	4.9%
10%	2.67 ± 0.09	19.1%
15%	2.85 ± 0.06	27.2%

The improvement in the crack initiation toughness values can be observed in each volume fraction relative to neat epoxy. A maximum increase of ~27% was achieved in the 15% V_f case. Higher volume fractions were not investigated due to the difficulty in casting samples with large amounts of filler.

4.3 Quasi-Static Photoelasticity Experiments and Results

With the previously determined stress-optic constant of each material known, it was then possible to evaluate the fracture performance of these transparent composites using photoelasticity. As a first step, edge cracked glass-filled epoxy samples were loaded in symmetric four-point bend configuration (as shown in Figure 3-5) and examined in a dark-field circular polariscope. Using an Instron 4465 machine, a load of approximately 500 N, sufficient for producing discernible crack tip fringes without causing specimen fracture, was applied. Using a typical DSLR camera fitted with a green filter, fringes representing isochromatics, or the maximum in-plane shear stresses, were

recorded in the region of interest. An example of the same for a 5% V_f is shown in Figure 4-5.

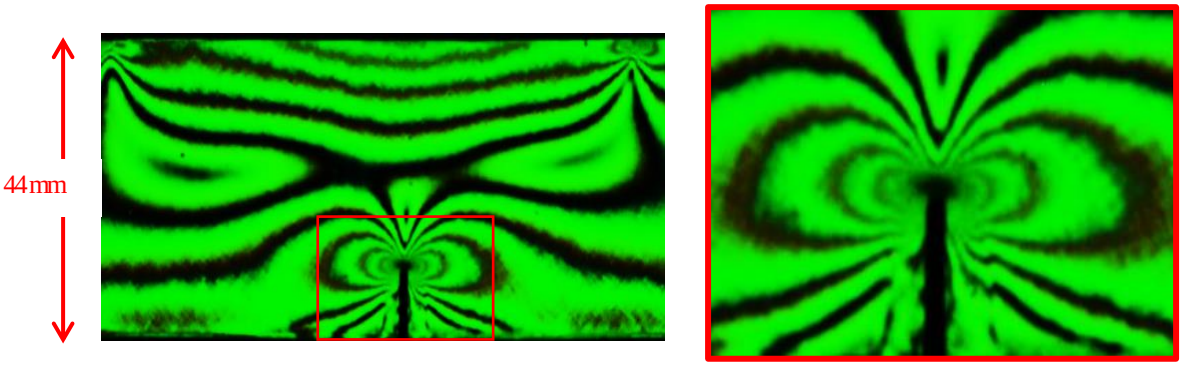

Figure 4-5: Isochromatic fringes in a notched sample (5% V_f) under symmetric four-point bend configuration (left). Close up of region of interest around the crack tip (right)

Very good crack tip fringe discernibility is evident in the enlargement of the crack tip region. In order to determine the feasibility of K_I evaluation using photoelasticity for the composites, the classical Smith and Schroedl method [26] was initially used due to its simplicity. As was discussed in chapter 3, K_I values were evaluated from the selection of two points at 90º from the crack tip from which the respective fringe orders, distance from the crack tip, and applied load were measured. For each image, multiple sets of data point pairs were analyzed, and the results averaged.

A comparison between the experimentally determined and theoretical K_I values (evaluated from the Boundary Collocation Method [27]) for samples of each V_f is shown below in Table 4-2:

Table 4-2: Experimentally determined and theoretical K_I values for 0%, 5%, 10%, and 15% glass-filled epoxy composites under quasi-static symmetric four-point bending

V_f (%)	Load (N)	K_I (Smith and Schroedl) (MPa√m)	K_I (Theoretical) (MPa√m)
0%	447	1.54	1.52
5%	453	2.17	2.168
10%	511	1.70	1.705
15%	528	1.67	1.76

Clearly, those obtained from the Smith and Schroedl method match closely to the theoretical counterparts with a maximum % difference of ~5% seen in the 15% V_f case.

With photoelasticity having been validated as an accurate optical method to investigate this material, a more robust and popular over-deterministic nonlinear least-squares analysis approach (from Chapter 3) was used to determine the mode-I stress intensity factors. This analysis was performed using the same images from the previous Smith and Schroedl analysis to allow for a good comparison between the measured K_I values obtained from the two experimental methods. Results of both experimental methods are compared to the theoretical values in Table 4-3:

Table 4-3: Comparison of experimentally and theoretically determined K_I values

V_f (%)	Load (N)	$K_{I\ \text{Smith and Schroedl}}$ (MPa√m)	$K_{I\ \text{Least squares}}$ (MPa√m)	$K_{I\ \text{Theoretical}}$ (MPa√m)
0%	447	1.54	1.53	1.52
5%	453	2.17	2.15	2.168
10%	511	1.70	1.68	1.705
15%	528	1.67	1.79	1.76

Again, experimental results from the least-squares analysis are consistent with both the Smith and Schroedl and theoretical analysis. With static fracture behavior of the composites explored, dynamic experiments were to be performed to understand these materials further.

CHAPTER 5: DYNAMIC FRACTURE EXPERIMENTS; MODE-I

In this chapter, the photoelastic evaluation of the effect of volume fraction and load rate on the fracture behavior of the transparent glass-filled epoxy composites under dynamic mode-I impact loading is presented. The material preparation, experimental setups used, and implementation of a high-speed photoelastic imaging configuration are described. Also, the measured crack velocities and dynamic mode-I stress intensity factor histories are shown and are followed by a discussion of those results. The chapter concludes with an explanation of a complementary finite element analysis performed to supplement experimental results for which closed form solutions do not exist.

5.1 Sample Preparation

Glass-filled epoxy composite sheets of 0%, 5%, 10%, and 15% volume fraction (by filler) were prepared in the manner described in Chapter 2 (Section 2.1). After curing for a minimum of 7 days, specimens were then machined into 80 mm x 40 mm x 9 mm specimens and an edge notch of 8 mm (a/W = 0.2) was introduced at the mid-span of each specimen which was then sharpened with a razor blade. A schematic of the specimen geometry is shown in Figure 5-1:

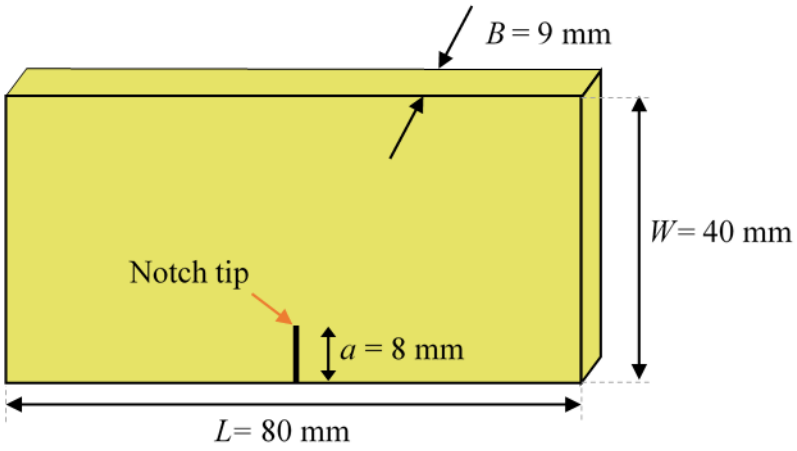

Figure 5-1: Specimen geometry used in dynamic mode-I fracture tests

5.2 Experimental Details

In this study, the dynamic mode-I fracture behavior of the transparent glass-filled epoxy composite was evaluated with respect to two parameters: loading rate and filler volume fraction. In order to investigate the loading rate effect, dynamic mode-I fracture tests were conducted with three unique loading configurations; a pneumatic table-top plunger and a gas-gun assisted long-bar impactor (Hopkinson Pressure Bar) setup with and without a pulse shaper. A detailed description of each setup is given in the following sections. To examine the volume fraction effect, glass-fiber filled epoxy samples of 0%, 5%, 10%, and 15% volume fractions were tested at each setup.

A dark-field circular polariscope in conjunction with high-speed photography was employed to study the dynamic fracture event. Upon loading, isochromatic fringe patterns emerged and were recorded using a single sensor, adjustable pixel resolution Phantom high-speed camera at 100,000 frames per second and with a spatial resolution of 256 x 200 pixels. The illumination was provided using an incoherent LED laser light

source (product SI-LUX-640 from Specialized Imaging, Inc.) programmed to pulse for 10 ns at a frequency of 100,000 Hz to match the framing rate of the camera.

While configuring the recording equipment, a tradeoff between frame rate and resolution was made based on the data rate capabilities of the high-speed camera, where an increase in pixel resolution reduced the maximum possible framing rate and vice versa. A good compromise between image quality and imaging rate was found at a framing rate of 100,000 frames per second and a resolution of 256 x 200 pixels.

Furthermore, it should be noted that dynamic photoelasticity, when used to visualize and quantify maximum shear stresses in the field-of-view, the light intensity contours travel at shear wave speed (C_s) in the material. For most photoelastic polymers, C_s is approx. 1000-1200 m/s and hence capturing the instantaneous values of stress fields requires very short duration exposure to prevent smearing of the light intensity information. That is, the exposure time should be limited to 10-50 ns for the successful capture of high contrast fringes without smearing. This behavior can be seen by comparing images from two separate table-top plunger tests where only the light source was changed in otherwise identical test setups. Figure 5-2(a) shows a 5% V_f sample at t = -20 μs (t = 0 corresponds to crack initiation) illuminated with a 2400 watt halogen light source which was recorded at 100,000 frames per second (the maximum recording rate of the camera at the selected image resolution) and exposure time set to 8 μs (minimum exposure time allowed by the camera software at the selected frame rate). In Figure 5-2(b), a different 5% V_f sample was recorded under the same loading conditions and identical camera settings (100,000 Hz, 8 μs exposure time); however, illumination was

provided from a LED laser light source (product SI-LUX-640 from Specialized Imaging, Inc.) programmed to pulse for 10 ns at a frequency of 100,000 Hz to match the framing rate of the camera, as opposed to the halogen light.

Due to the camera's relatively long minimum exposure time, when recording fringe illuminated with the halogen source, smearing was significant and fringes were poorly defined, especially near the crack tip. This issue was significantly reduced by using the frame rate synchronized pulsing laser. By providing a single extremely short pulse (adjustable from 10 ns to 30 ns) once per frame, the exposure time for each image was effectively equal to the pulse duration. This extremely short illumination period provided significantly sharper fringes and was utilized in all subsequent high-speed photoelastic testing.

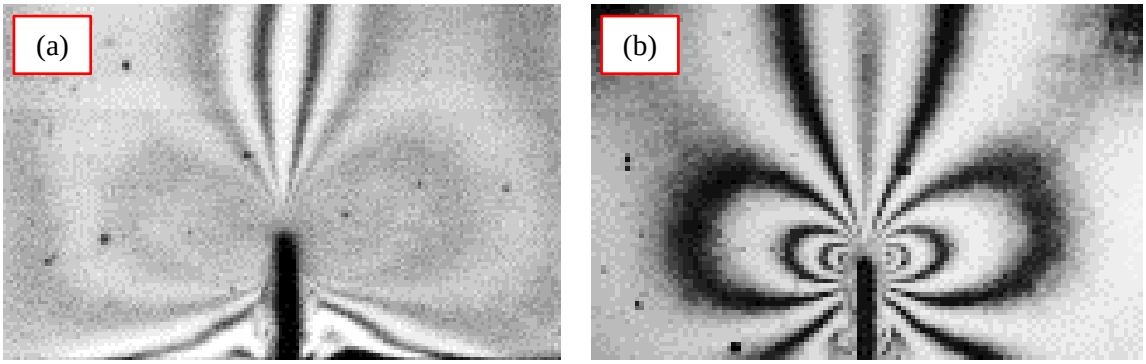

Figure 5-2: Comparison of isochromatic fringes of two 5% V_f samples under identical dynamic mode-I loading configuration illuminated with (a) a continuous halogen light source and (b) a synchronized pulsing laser (a single 10ns pulse per frame). Images were recorded using a Phantom high-speed camera at a framing rate of 100,000 frames per second and a resolution of 256 x 200 pixels.

5.1.1 Table-top Plunger Setup

Dynamic mode-I fracture of the glass-filled epoxy composites was studied first using a pneumatic table-top plunger in conjunction with a circular-dark field polariscope and high-speed photography. A three-point-bend impact setup was configured by fitting a hemispherical steel crosshead to the plunger and aligning two fixed supports equidistantly about the impact point.

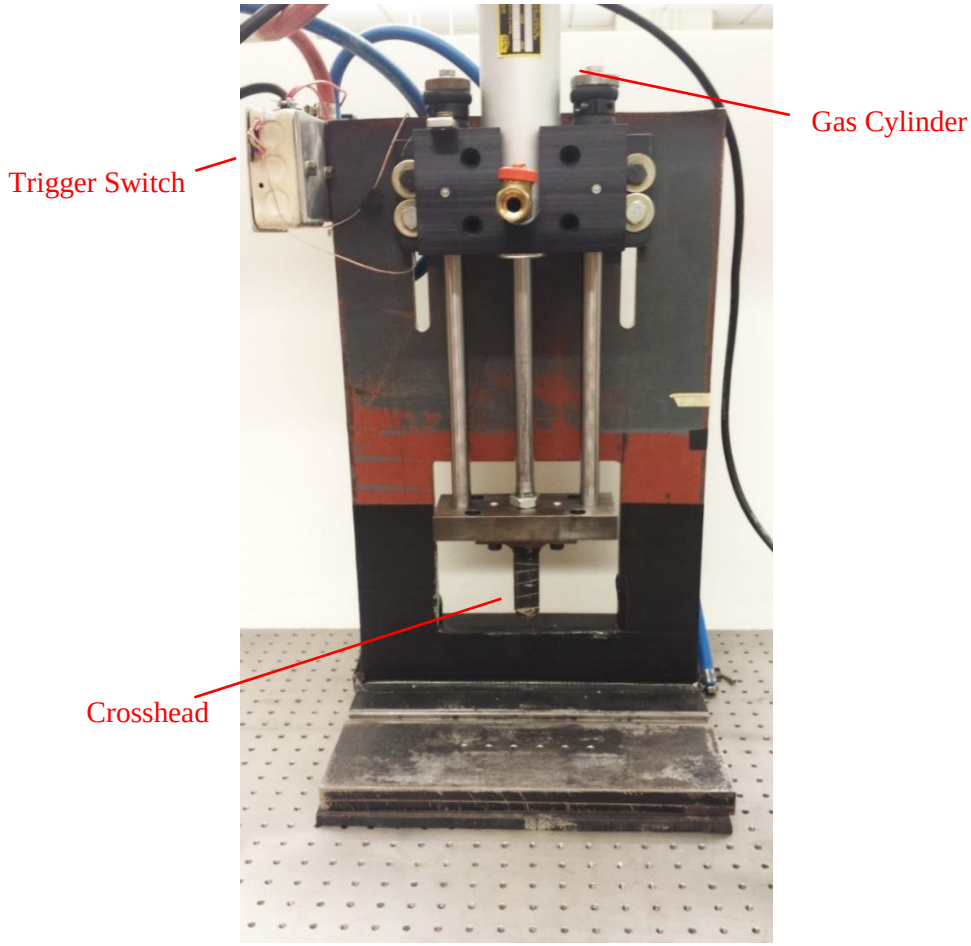

Figure 5-3: Photograph of the table-top pneumatic plunger

An impact velocity of 2.5 m/s was selected by adjusting the pressure of the gas cylinder's feed line, measuring the resulting crosshead velocity using photogate timer measurements. Additionally, to ensure that a consistent velocity was maintained, these measurements were also performed during each test, and results were compared to previous results.

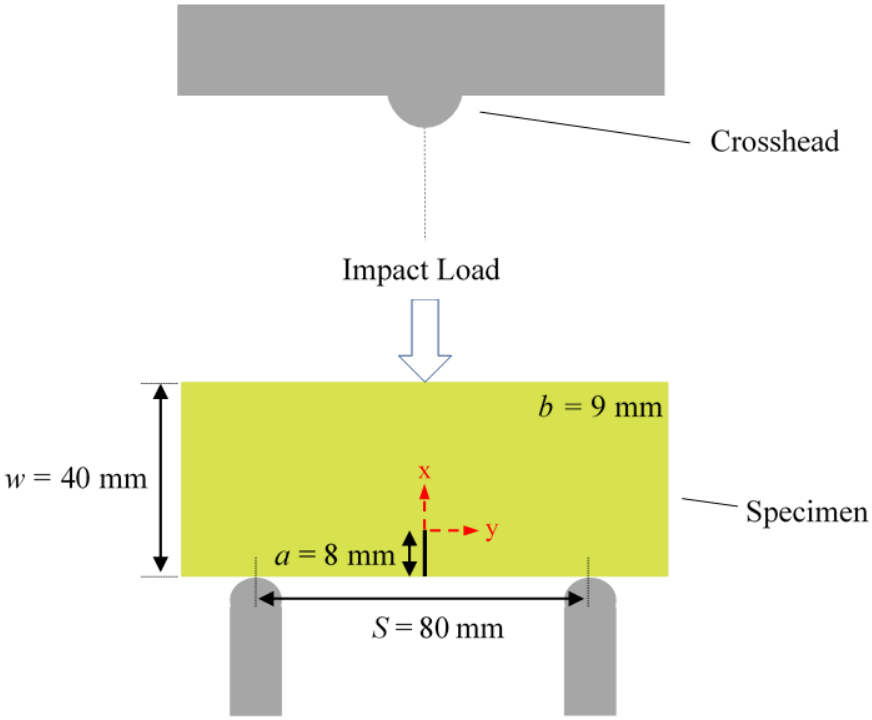

Figure 5-4: Table-top plunger impact loading schematic

Images from the area of interest around the crack-tip were recorded with the previously discussed Phantom high-speed camera and pulsed laser light source illumination setup at 100,000 frames per second and with a spatial resolution of 256 x 200.

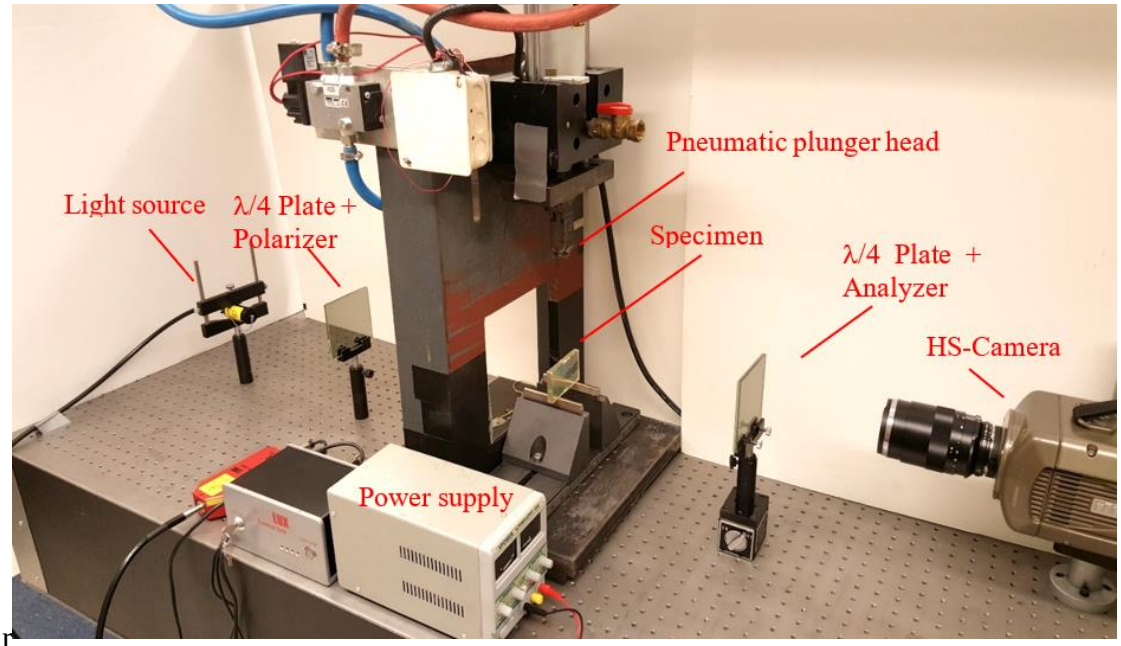

Figure 5-5: Photograph of the table-top plunger and high-speed photoelasticity setup

Triggering of the recording devices was achieved through an electrical circuit created by a DC power supply from which a 5-volt output signal was introduced on the surface of the plunger near the crosshead. The output signal was attached to a trigger box for the camera/laser, and the top surface of the sample was made conductive with adhesive aluminum tape. Once the plunger was propelled downward, the output signal from the crosshead was able to pass through the sample, then the trigger box and back to the input of the power supply, thus completing the circuit and triggering both the camera and the laser (Figure 5-6).

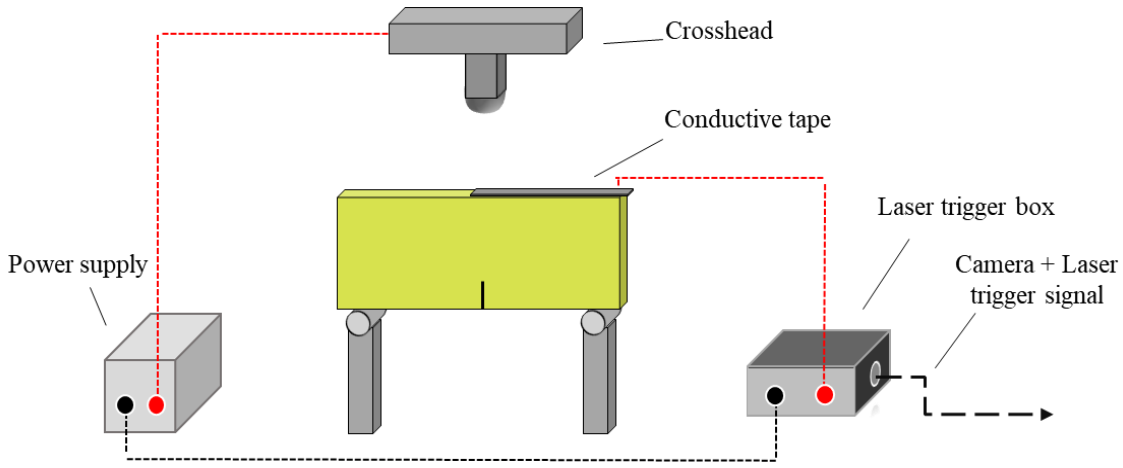

Figure 5-6: Schematic of camera and light source trigger circuit for the pneumatic table-top plunger setup

Once properly configured and a consistent impact velocity was ensured through repeated photogate timer measurements, a dark-field circular polariscope setup was introduced to the pneumatic plunger apparatus (Figure 5-5). Next, with the plunger fixed in a "raised" position, samples were placed on the supports and aligned such that the crack line was centered about the hemispherical crosshead. Finally, the plunger was propelled with a gas cylinder, and images of the resulting isochromatics fringe patterns around the crack tip were recorded.

5.1.2 Long-bar Impactor Setup

Two additional loading rates were achieved using a long-bar impactor setup consisting of a striker which was propelled using a gas-gun at a velocity of approximately 16 m/s into a long-bar (Hopkinson pressure bar) in contact with a specimen (Figure 5-8). The long-bar was 6 feet in length with a 1/4 inch semicircular bull-nose tip and the striker

was 1 foot in length. Additionally, both the long-bar and the striker were 1 inch in diameter and made of aluminum 7075-T6 in order to eliminate impedance mismatch between the two. Furthermore, the specimen was in contact with a soft putty strip on the top and bottom edges to prevent impedance mismatch between the edges of the specimen. A schematic of the specimen and loading configuration is shown in

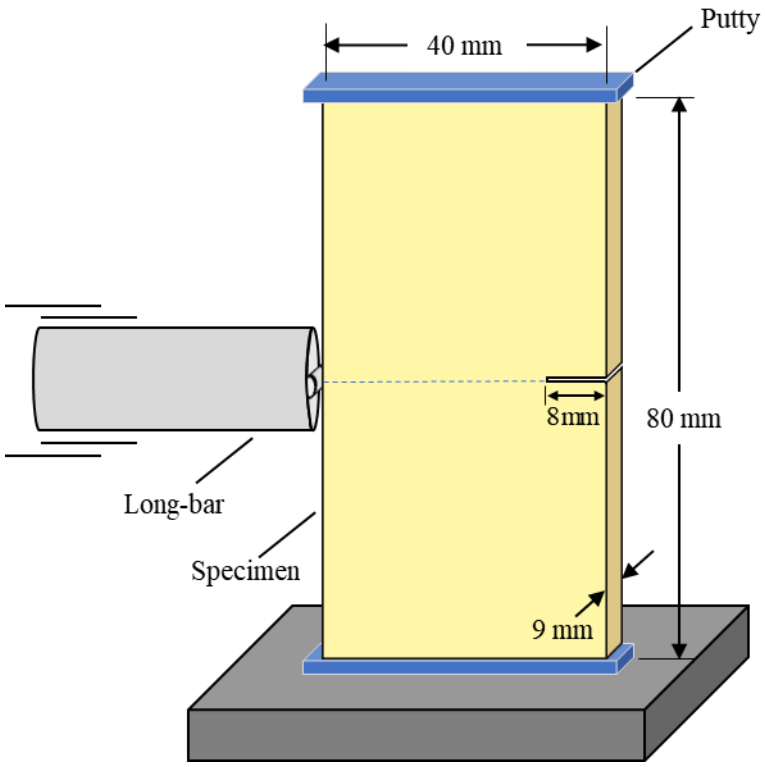

Figure 5-7: Schematic of the sample geometry and loading configuration used in the mode-I dynamic fracture tests (long-bar impactor setup)

The same resolution and framing rate from the table-top plunger experiments were used in these experiments; 256 x 200 pixels and 100,000 Hz. Triggering of the camera and laser lighting system was achieved in a similar manner with a 5V DC power source connected to the striker and the long-bar. As the striker contacted the long-bar, a

circuit was completed sending a 5V signal to the high-speed camera, which then would trigger the laser. Due to the camera's capability to record for nearly a full second and the laser's ability to produce light pulses for the same duration, no trigger delay was necessary to capture the fracture event.

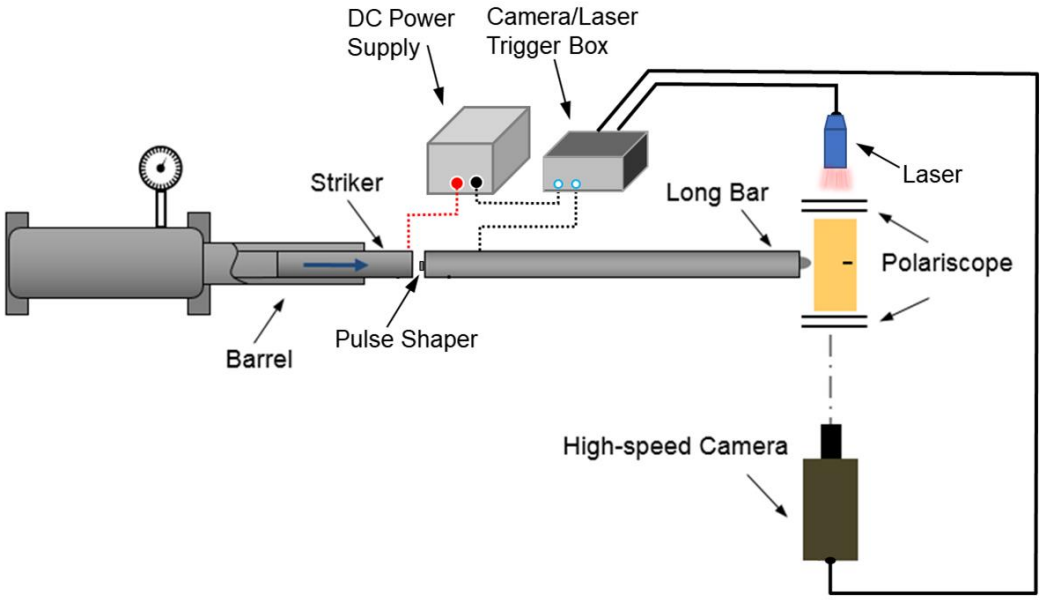

Figure 5-8: Schematic of the long-bar impactor and photoelastic experimental setup

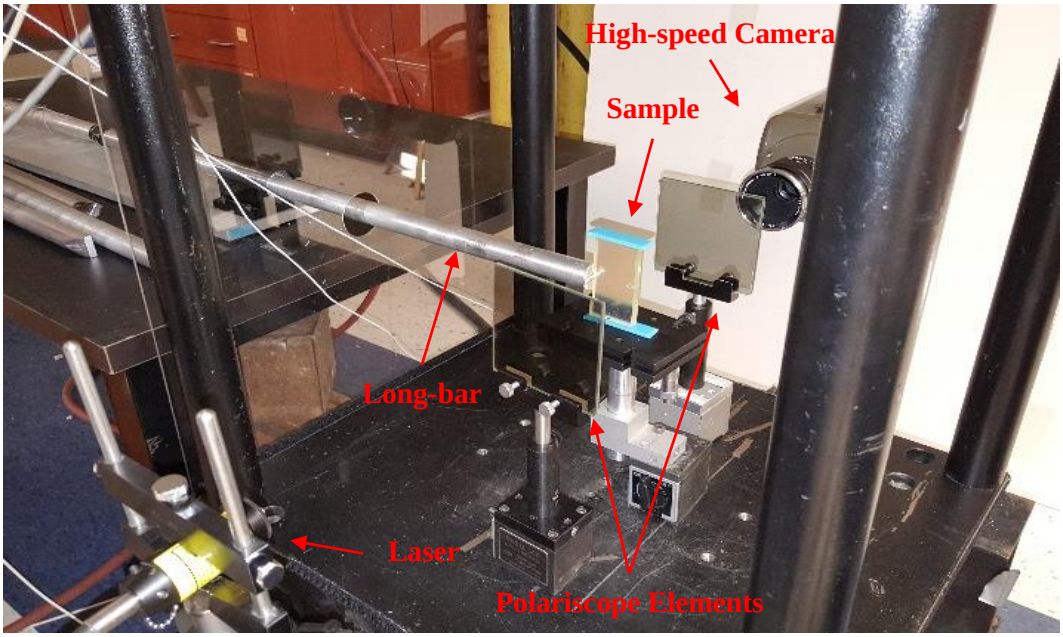

Figure 5-9: Photograph of long-bar impactor setup

To vary the loading rate using this setup, a soft aluminum 1100 pulse-shaper disk (11/32" in diameter, 1 mm thickness) was placed between the long-bar and striker lowering the loading rate, shown in Figure 5-10. Thus, two loading rates were generated by either directly impacting the long-bar with the striker or adding the pulse shaper to the long-bar [28]. The strain rate histories for each case are shown in Figure 5-11.

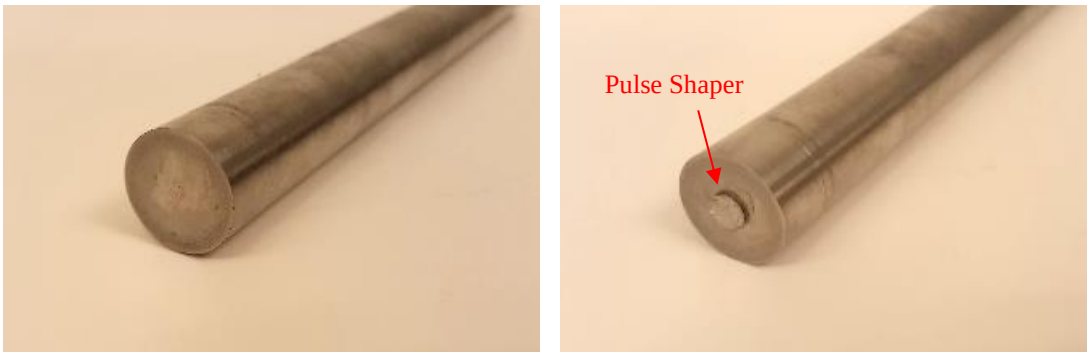

Figure 5-10: Aluminum 7075-T6 long-bar with no pulse-shaper (left) and aluminum 1100 dish pulse-shaper (right)

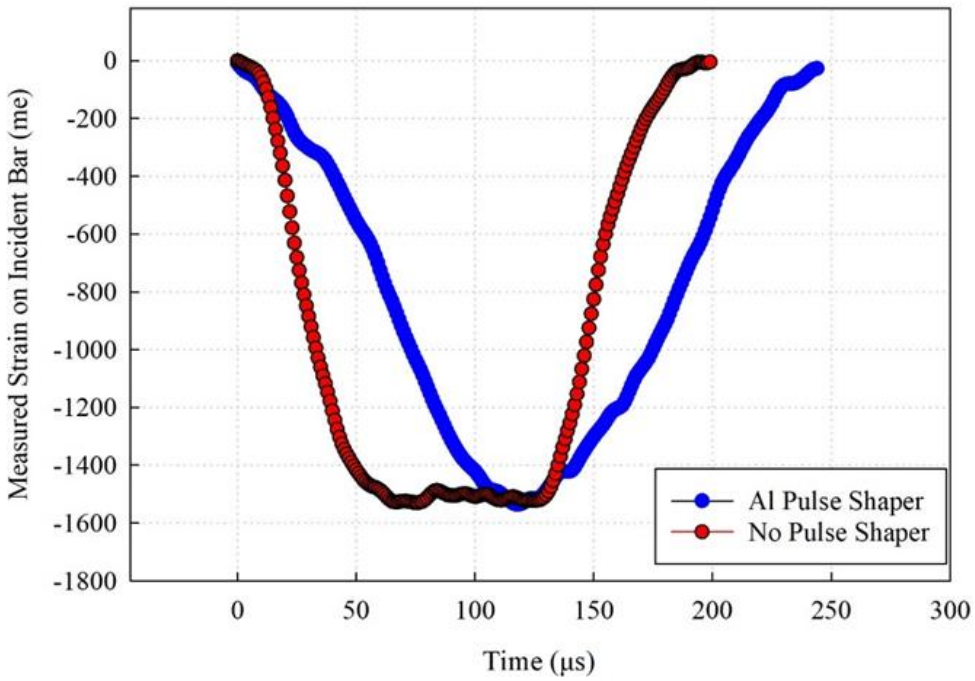

Figure 5-11: Measured strain histories on long-bar for No PS and PS cases [29]

Just as in the table-top plunger case, the optical information was recorded at 100,000 frames per second and illuminated with a 10 ns laser pulse as 100,000 Hz. Four glass-filled epoxy samples for each filler V_f with and without pulse shaper conditions were tested. In each case, good fringe discernibility was achieved, both before and after crack initiation.

5.2 Table-top Plunger Results

Representative images for the table-top plunger test for each volume fraction at time -20 μs, 0 μs and 20 μs (0 μs corresponds to crack initiation) are shown below in Figure 5-12:

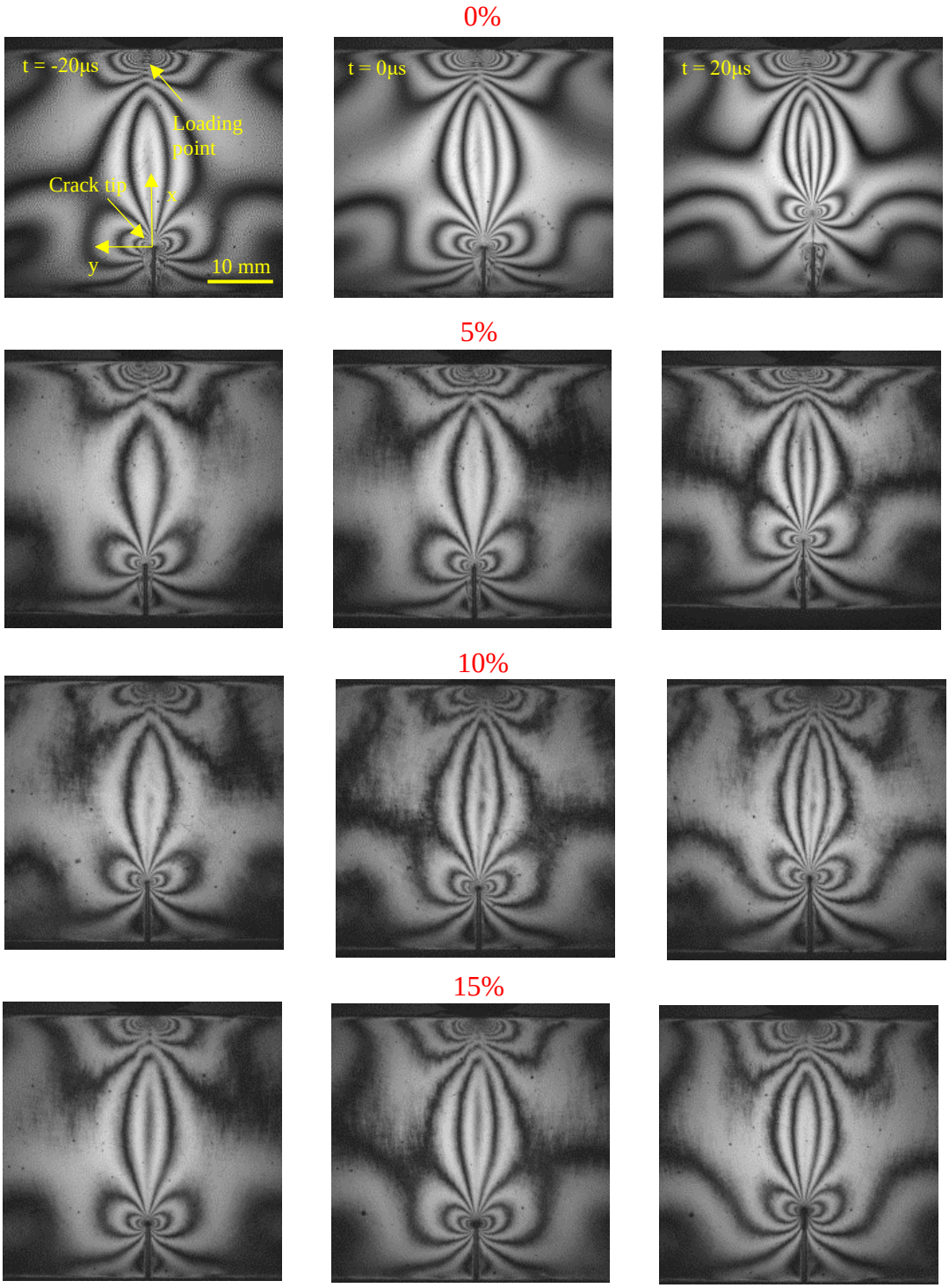

Figure 5-12: Isochromatic fringe patterns for 0%, 5%, 10%, and 15% V_f composites under dynamic mode-I loading (Table-top Plunger). Images were recorded with high-speed photography at 10 μs intervals (t=-20 μs, 0 μs, and 20 μs shown)

These images were used to measure crack velocity, and the fringe patterns were digitized to measure crack-tip stress intensity factors (SIFs). By measuring the crack length in each image recorded during high-speed photography, crack velocities were calculated using a central-difference method and are shown in Figure 5-13.

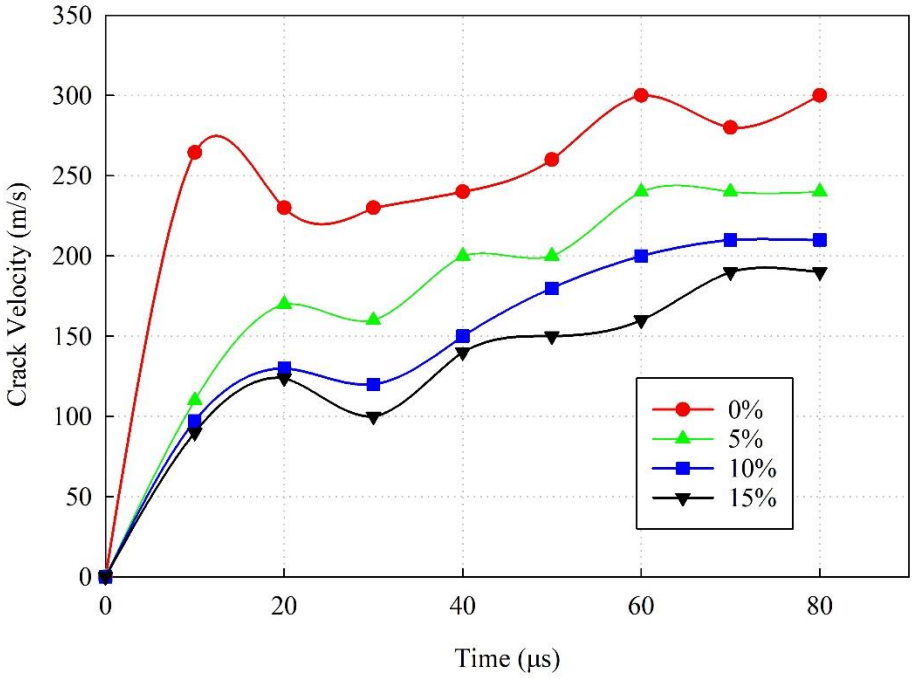

Figure 5-13: Measured crack velocity histories of 0%, 5%, 10%, and 15% V_f samples for dynamic mode-I fracture tests (table-top plunger case)

Clearly, there is a substantial decrease in the apparent crack velocity as the volume fraction of fillers is increased. Comparing peak velocities between the 0% and the 15% case, a decrease of over 50% is seen, indicating that the presence of glass fiber inhibits crack growth. Furthermore, using fringe order, distance from the crack-tip, and angle for each digitized point relative to the instantaneous crack direction, the mode-I stress intensity factor, K_I, was determined for each image with the previously discussed over-deterministic least-squares analysis.

The measured K_I histories for the plunger test are shown Figure 5-14. As noted earlier, the crack initiation for the different experiments was made to coincide with $t = 0$ or observed crack initiation for consistency. Within the window of observation, K_I values for each case increase monotonically up to crack initiation. Once the crack initiates, a drop in K_I occurs due to instantaneous unloading in the crack-tip region. Subsequently, the stress intensity factors continue to decrease in these low-rate dynamic loading cases.

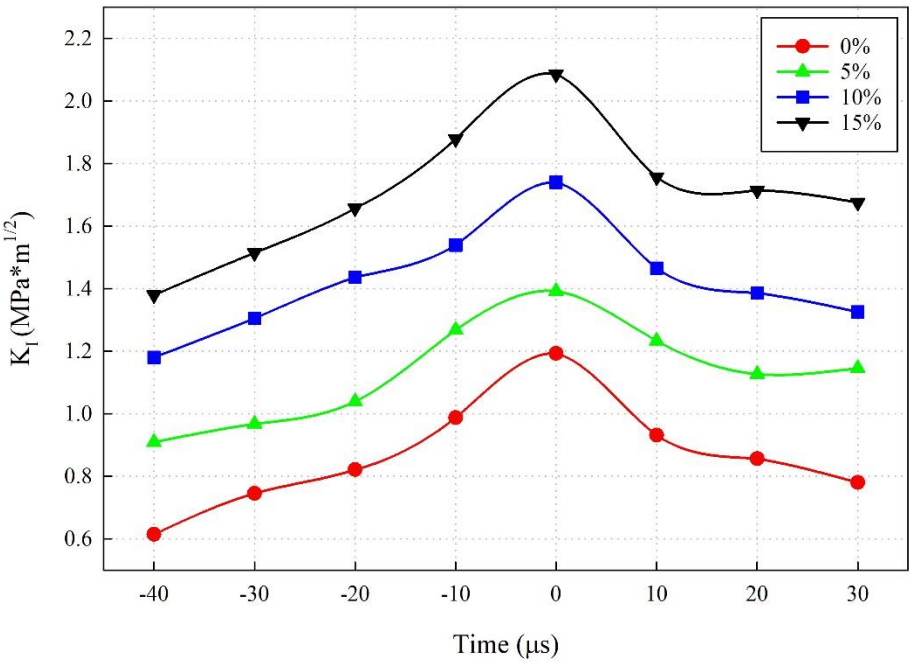

Figure 5-14: K_I histories for 0%, 5%, 10% and 15% V_f glass-filled epoxy composites (table-top plunger case)

Once again, as the volume fraction of filler increases, higher K_I values are achieved with a maximum increase of approximately 75% in the 15% V_f case. The K_{Icr} values at crack initiation for each volume fraction are tabulated in Table 5-1.

Table 5-1: Crack initiation toughness (K_{Icr}) values for glass-filled epoxy composites at V_f = 0%, 5%, 10%, and 15% and relative % increase compared to 0% V_f. Dynamic mode-I loading with table-top plunger setup.

V_f (%)	K_{Icr} (MPa√m)	*% Increase*
0%	1.19 ± 0.07	-
5%	1.39 ± 0.05	16.8%
10%	1.74 ± 0.04	46.2%
15%	2.08 ± 0.08	74.8%

5.3 Long-bar Impactor Results

In order to understand the behavior under higher loading rates, the composites were tested using a Hopkinson pressure bar impactor or simply a long-bar. Tests were performed with and without an aluminum pulse shaper placed between the striker and the long-bar. The diameter of the 1100 aluminum pulse shaper was 11/32" and was of 1 mm thickness.

The effect of the strain rate variance between the pulse shaper and no pulse shaper case was immediately evident in the difference between the crack velocities of corresponding specimens. First, the crack lengths were measured from each image after initiation using MATLAB, and crack velocities were generated by employing a backward-difference method. Figure 5-15 and Figure 5-16 show the crack velocity histories for the pulse shaper and no pulse shaper cases, respectively.

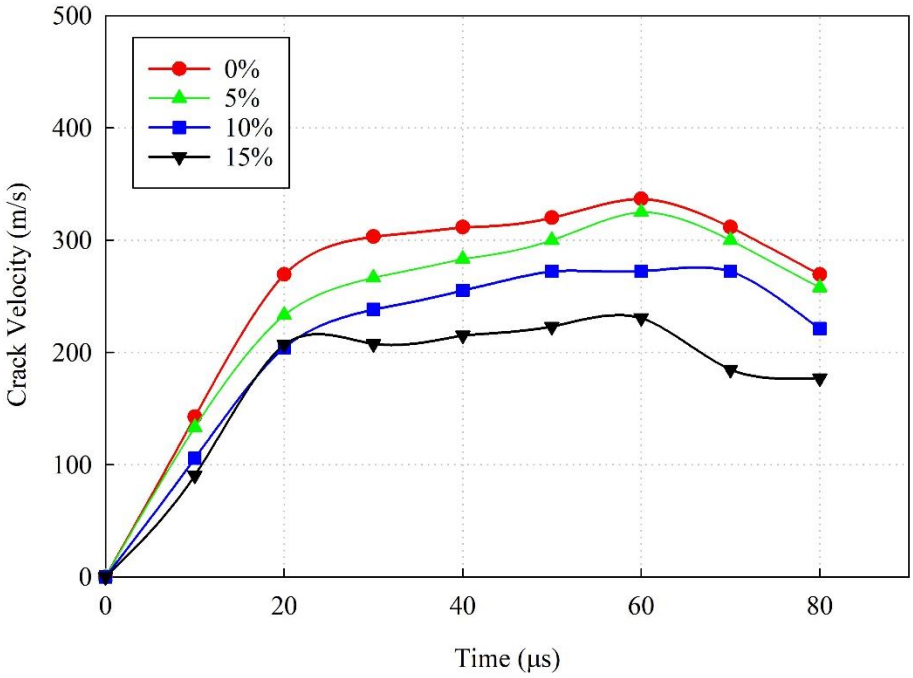

Figure 5-15: Measured crack velocity histories of 0%, 5%, 10%, and 15% V_f samples for dynamic mode-I fracture tests (long-bar with pulse shaper case)

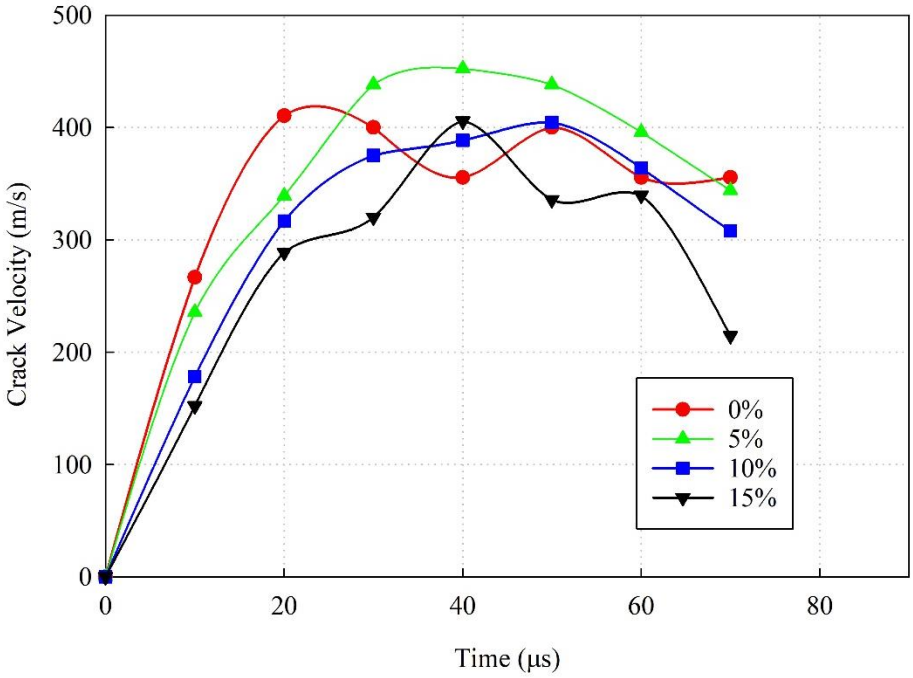

Figure 5-16: Measured crack velocity histories of 0%, 5%, 10%, and 15% V_f samples for dynamic mode-I fracture tests (long-bar no pulse shaper case)

Clearly, the introduction of soft aluminum 1100 pulse shaper produced slower crack growth and acceleration when compared to the no pulse shaper case. A reduction in crack velocity with respect to increasing filler V_f was observed.

Representative fringe patterns at 0 μs, 20 μs, and 40 μs intervals for the pulse shaper and no pulse shaper case are shown in Figure 5-17 and Figure 5-18, respectively:

Pulse Shaper

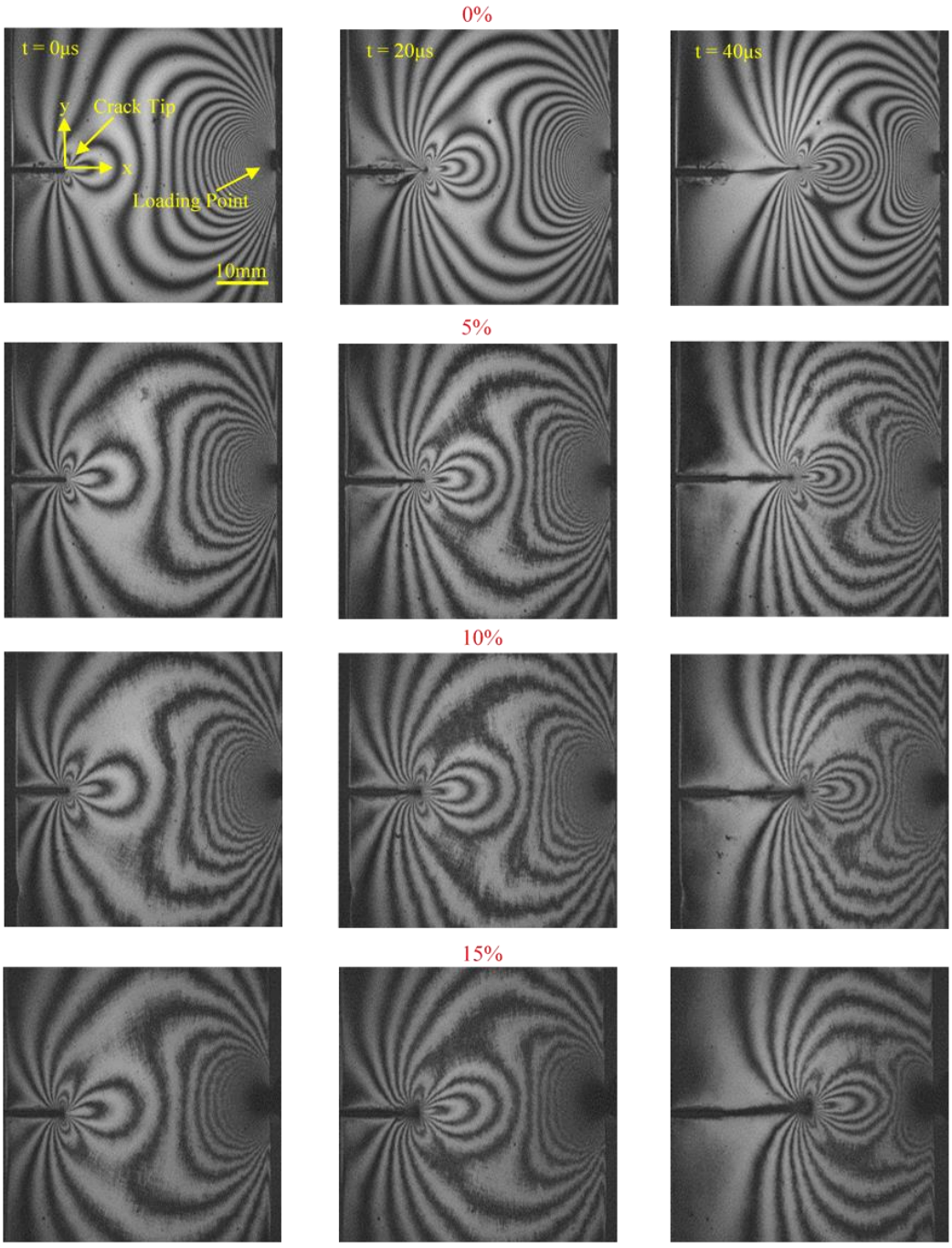

Figure 5-17: Isochromatic fringe patterns for 0%, 5%, 10%, and 15% V_f composites under dynamic Mode-I loading (Pulse Shaper). Images were recorded with high-speed photography at 10 μs intervals (t=0 μs, 20 μs, and 40 μs shown)

No Pulse Shaper

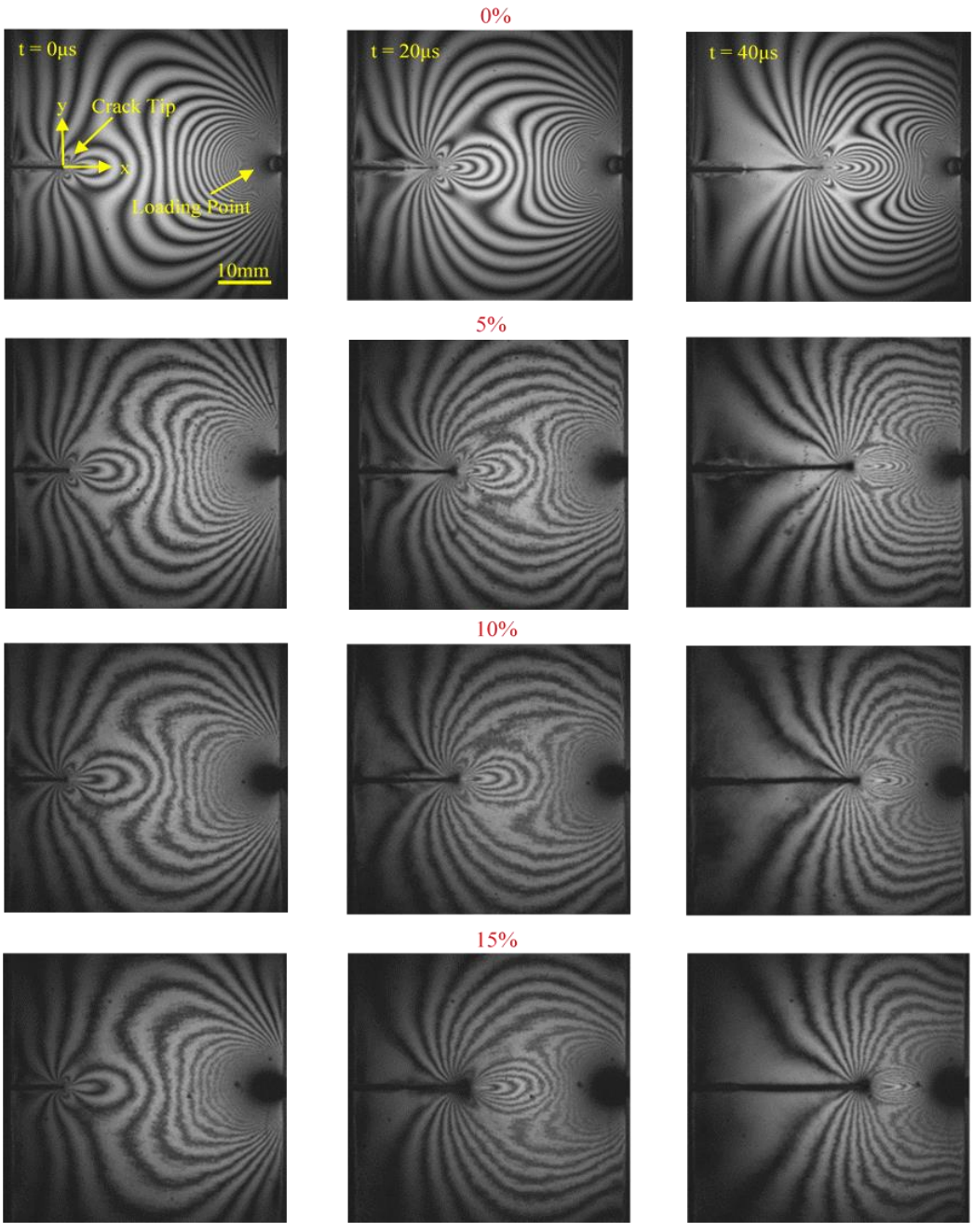

Figure 5-18: Isochromatic fringe patterns for 0%, 5%, 10%, and 15% V_f composites under dynamic Mode-I loading (No Pulse Shaper). Images were recorded with high-speed photography at 10 μs intervals (t=0 μs, 20 μs, and 40 μs shown)

5.3.1 Long-bar Impactor Results: With Pulse Shaper (PS)

Next, images for the case with pulse shaper were analyzed at intervals of 10 μs between -20 μs and 20 μs as fringe discernibility was greatly reduced outside of this time window. Mode-I and mode-II stress intensity factors were evaluated by averaging results from four samples and using the over-deterministic least-squares analysis described in the previous chapter.

As can be seen in Figure 5-19, K_I values increased correspondingly with increasing filler volume fraction. Furthermore, unlike in the table-top impactor experiments, the stress intensity factors here increase in the post-initiation time period attributed to the continued loading phase of the pulse following crack initiation. Comparing K_I values at crack initiation, an increase of 140% was found between the 0% and 15% cases. Additionally, K_{II} values close to zero indicate the crack initiation and growth occurred in nearly mode-I condition. The results for each volume fraction are shown in Table 5-2.

Table 5-2: Crack initiation toughness or critical SIF (K_{Icr}) values for glass-filled epoxy composites at V_f = 0%, 5%, 10%, and 15% and relative % increase compared to 0% V_f. Dynamic mode-I loading with long-bar with pulse shaper setup.

Filler % (V_f)	K_{Icr} (MPa√m)	% Increase
0%	1.43 ± 0.03	-
5%	2.16 ± 0.08	51.0%
10%	2.80 ± 0.10	95.8%
15%	3.43 ± 0.04	139.9%

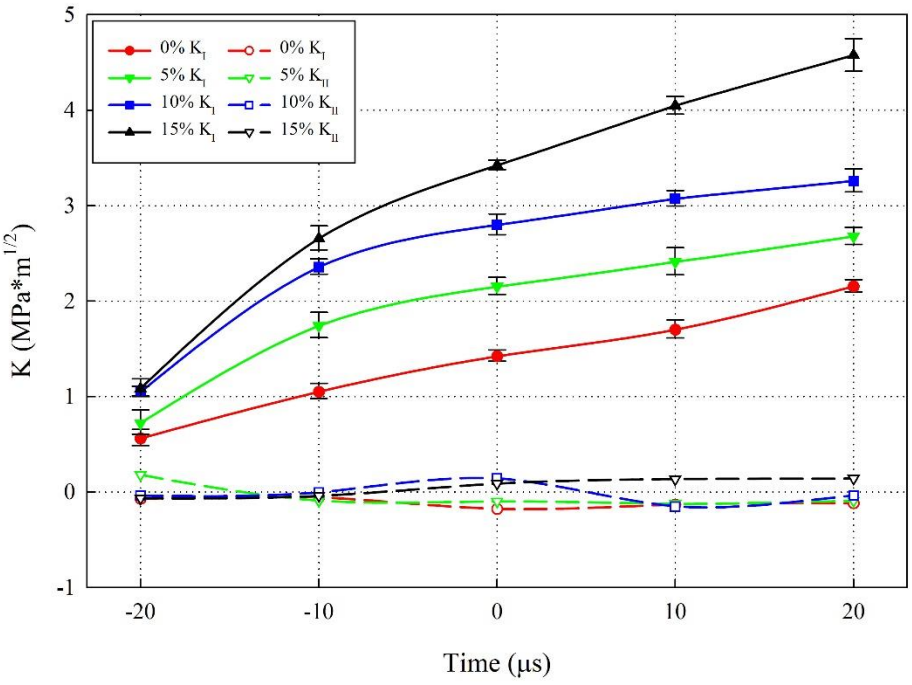

Figure 5-19: K_I and K_{II} histories for 0%, 5%, 10%, and 15% V_f glass-filled epoxy composites (long-bar with pulse shaper)

5.3.2 Long-bar Impactor Results: No Pulse Shaper

As with the pulse shaper cases discussed in the previous section, mode-I and mode-II stress intensity factors were determined for the no pulse shaper case by averaging values from four samples and using the over-deterministic least-squares analysis of digitized fringe data. Results from this analysis are plotted in Figure 5-20.

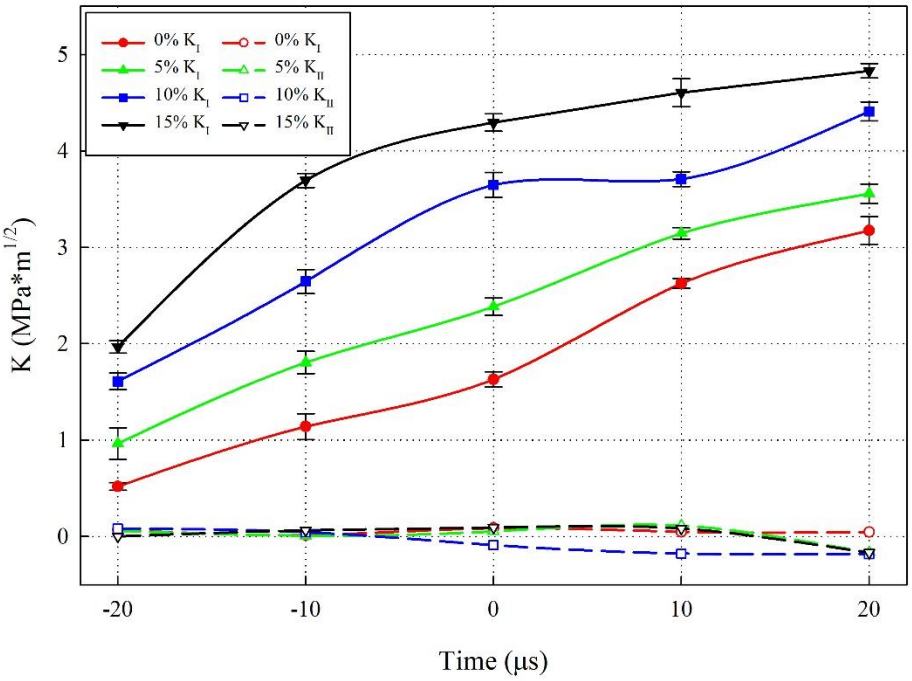

Figure 5-20: K_I and KII histories for 0%, 5%, 10% and 15% Vf glass-filled epoxy composites (long-bar no pulse shaper)

As seen in the long-bar with pulse shaper case, the stress intensity factors continued to increase in the post-initiation time period attributed to a continued loading phase of the pulse following crack initiation. Comparing K_I values at crack initiation, an increase of approximately 163% was found between the 0% and 15% cases. Again, good mode-I conditions are evident as the values of K_{II} are negligibly small when compared to

K_I. Additionally, an increase in K_I values compared to the case when the pulse shaper was used shows the effect of increased strain rate. The K_{Icr} values for each volume fraction are shown below in Table 5-3:

Table 5-3: Crack initiation toughness or critical SIF (K_{Icr}) values for glass-filled epoxy composites at V_f = 0%, 5%, 10%, and 15% and relative % increase compared to 0% V_f. Dynamic mode-I loading with long-bar with no pulse shaper setup.

Filler % (V_f)	K_{Icr} (MPa$\sqrt{m}$)	% Increase
0%	1.63 ± 0.07	-
5%	2.38 ± 0.08	46.0%
10%	3.64 ± 0.12	123.3%
15%	4.29 ± 0.04	163.2%

5.4 Finite Element Analysis

To gain additional confidence in the fracture parameter measurements in the new material, specimen geometry, and loading configuration for which a closed for solution does not exist, a complementary finite element analysis was performed. The long-bar PS and No PS configurations were selected for their simpler boundary conditions and the availability of strain history measured during the impact loading event. Due to the robustness of explicit methods when dealing with complex contact conditions, such as those present in this study, ABAQUS/Explicit was selected for this analysis. Another

advantage of explicit methods is that they are generally computationally efficient. It should be noted that very small time steps are required in order to maintain stability which can be computationally expensive for large simulations, though this was not considered an issue for this study.

Past research has demonstrated an effective methodology for performing such an analysis and hence was adopted for this study [30]. The specimen was modeled as a free-standing solid subjected to transient load by the long-bar. The model was discretized into 71992 tetrahedral elements with 14434 nodes (Figure 5-21). Additionally, a seeding around the crack tip and contact point was performed locally to create a finer mesh.

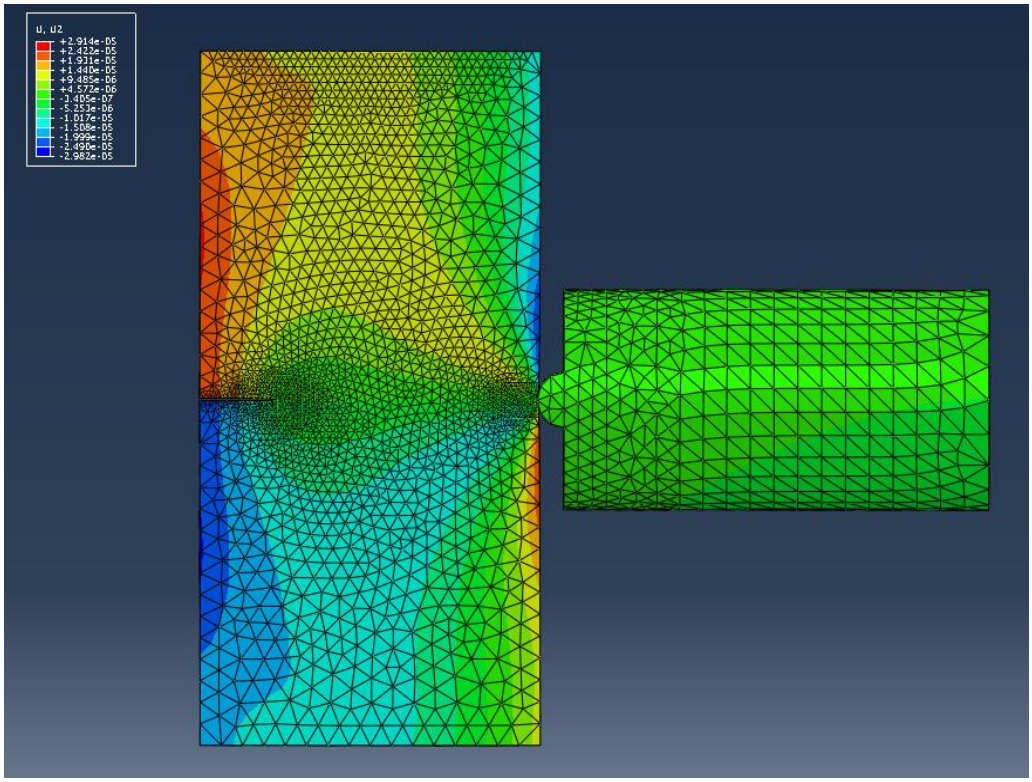

Figure 5-21: Discretized finite element model of glass-fiber epoxy composite and long-bar

Material properties for the 10% V_f glass-filled epoxy composite (Table 3-1) and the aluminum long-bar (E=71.7 GPa, ν=0.3, ρ=2730 kg/m^3) were input and the boundary conditions shown in Figure 5-22 were applied. In order to determine the input velocity, strain gage measurements were performed on the long-bar for both the pulse shaper and no pulse shaper cases. From the strain data, particle velocities were calculated using $V_p = C\varepsilon$ where C is the bar-wave speed for aluminum) and imposed on the model.

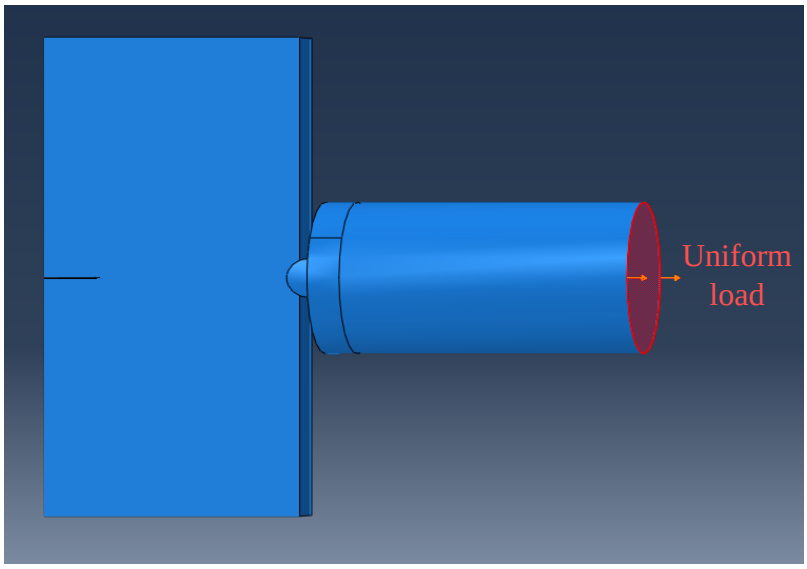

Figure 5-22: FEA model and applied boundary conditions

From the deformed model, paths were selected along the top and bottom crack faces/flanks (Figure 5-23), and crack opening (COD) and crack sliding (CSD) displacements were extracted at each nodal point.

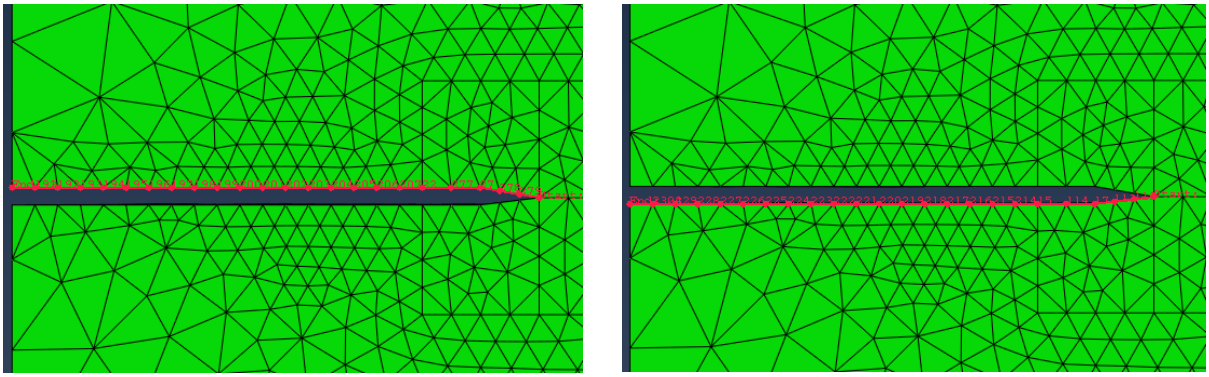

Figure 5-23: Selected nodes from the top (left) and bottom (right) crack faces used to measure the crack opening (COD) and crack sliding (CSD) displacements from FEA

The apparent K_I and K_{II} values were evaluated at each crack face node using the following expressions [31]:

$$(K_I)_{app} = \frac{E\sqrt{2\pi}}{8\sqrt{r}} u_{y'}; (r, \theta = \pi) \quad 5\text{-}1$$

$$(K_{II})_{app} = \frac{E\sqrt{2\pi}}{8\sqrt{r}} u_{x'}; (r, \theta = \pi) \quad 5\text{-}2$$

where E is the elastic modulus of the specimen, $u_{y'}$ and $u_{x'}$ are the half COD and CSD values, respectively.

Thus obtained $(K_I)_{app}$ and $(K_{II})_{app}$ were plotted as a function radial distance r along the crack faces, and by extrapolating the linear portion of the plot, true K_I and K_{II} values were determined. An example of the extrapolation of the mode-I stress intensity factor (K_I) for a 10% V_f sample at t=-10 μs is shown in Figure 5-24.

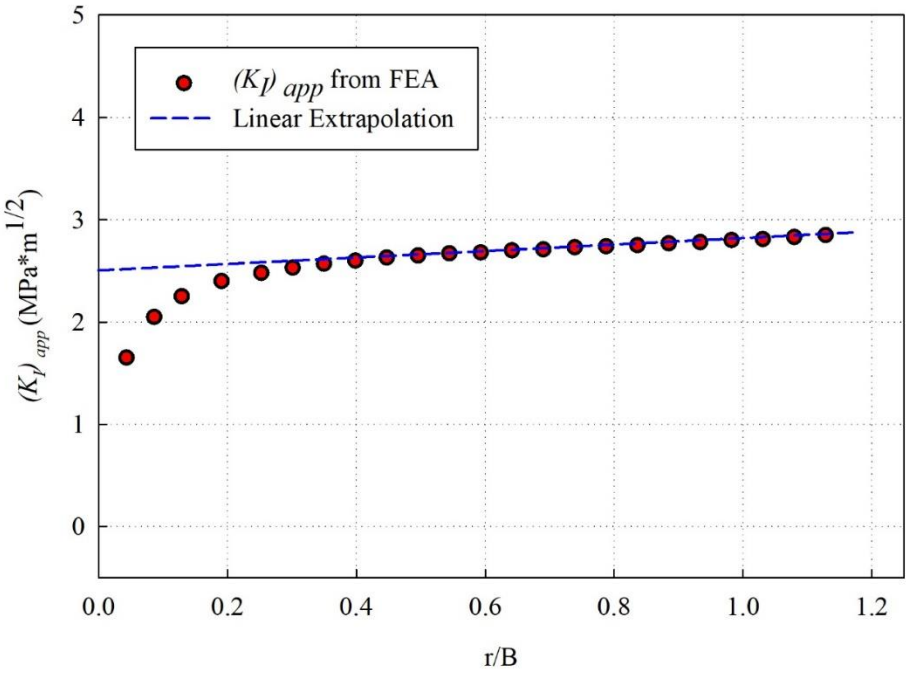

Figure 5-24: K_I evaluation from crack opening displacements obtained from FEA

This method was repeated from t = -40 μs to t = 0 μs (crack initiation) with 2.5 μs time steps. The computed FEA values were compared to the optically determined results. A good match between the two results was found, with a maximum deviation of 8% observed for the K_I values at t=0 from the pulse shaper case.

A comparison of the K_I and K_{II} histories from FEA and optical analysis for 10% V_f samples with and without a pulse shaper are shown in Figure 5-25(a) and Figure 5-25(b),

respectively.

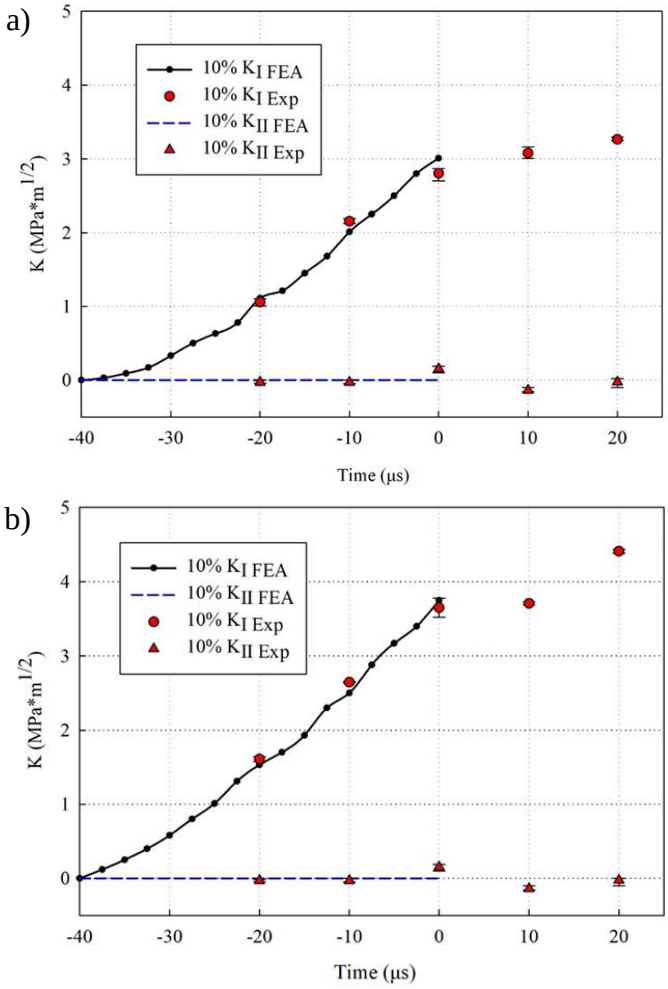

Figure 5-25: Comparison of the K_I and K_{II} histories obtained from FEA and photoelastic measurements for (a) long-bar with pulse shaper and (b) long-bar without pulse shaper

CHAPTER 6: DYNAMIC FRACTURE EXPERIMENTS – MIXED-MODE

In this chapter, an investigation of glass-filled epoxy composites fracture behavior under mixed-mode impact loading is described. Samples preparation and loading setup details are provided, followed by a description of the methodology to vary the mode-mixity in experiments. Evaluation of the crack initiation angles, crack velocity histories, and stress intensity factor histories from high-speed photoelastic images are presented, and the results are discussed.

6.1: Fracture Modes

Three pure modes of fracture exist and are defined as mode-I, mode-II, and mode-III. Mode-I fracture occurs due to tensile stress normal to the crack plane, causing a crack to open symmetrically. Mode-II fracture, or "in-plane crack sliding," is produced by shear stress acting parallel to the crack flanks. Lastly, mode-III fracture occurs due to out-of-plane shear stress acting on the crack flanks resulting in a tearing behavior. The three fracture modes are schematically shown in Figure 6-1.

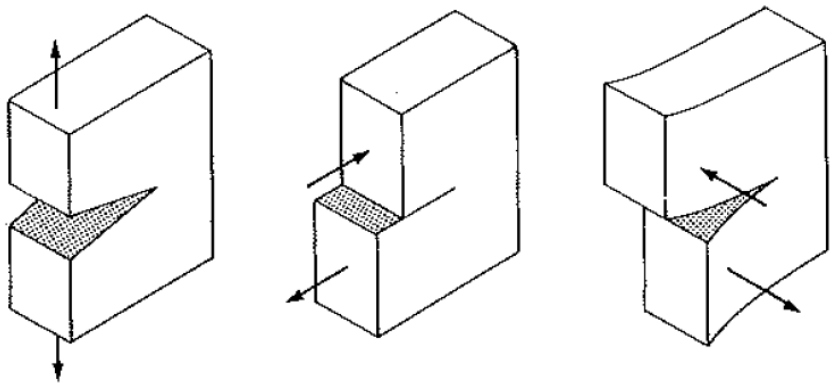

Figure 6-1: Schematics illustrating pure mode-I, mode-II, and mode-III fractures [25]

6.2: Sample Preparation and Experimental Procedure

To conduct a mixed-mode fracture study of the composites, glass-filled epoxy sheets were processed at 0%, 5%, 10%, and 15% filler volume fractions and machined into specimens with dimensions 80 mm x 40 mm x 9 mm. A notch was introduced at a fixed distance of 7.5 mm from the samples mid-span using a diamond impregnated circular saw and sharpened by scoring the root with a fresh razor blade. To produce different mode-mixites, three distinct notch lengths were used, 8 mm, 12 mm, and 16 mm (corresponding to a/W ratios of 0.2, 0.3, and 0.4, respectively). Due to limited availability of material, and the desire study each volume fraction under all three configurations, only two samples for each volume fraction were produced.

The mixed-mode dynamic fracture tests were conducted using the same experimental setup from the dynamic mode-I long-bar tests (describe in section 5.3). To establish a mixed-mode loading condition, samples were positioned with an eccentricity (e) of 15 mm, as shown in Figure 6-2.

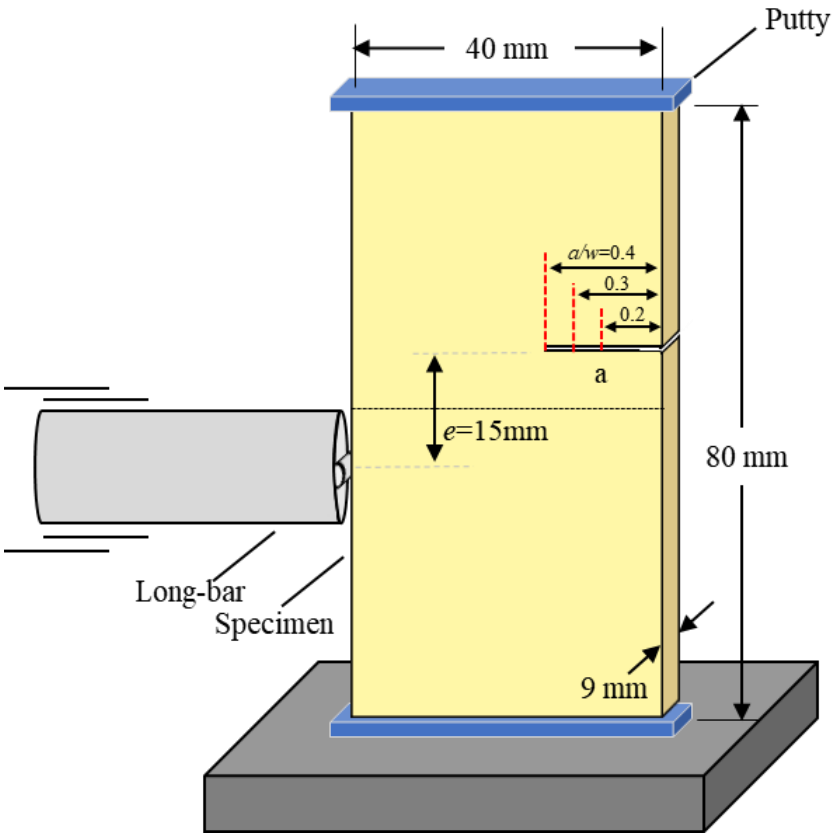

Figure 6-2: Schematic of the sample geometry and loading configuration used in the dynamic mixed-mode fracture tests

The impact velocity was maintained the same as the previous dynamic mode-I fracture tests, at ~16 m/s, and images of the fracture event were recorded with a Phantom high-speed camera at 100,000 frames per second using the pulsing LED laser light source illumination previously described in Chapter 5.

As an initial investigation into the fracture behavior with respect to various degrees of mode-mixity, images of 10% V_f samples for each *a/W* case were compared at $t = 0$ (immediately after crack initiation) and are shown in Figure 6-3.

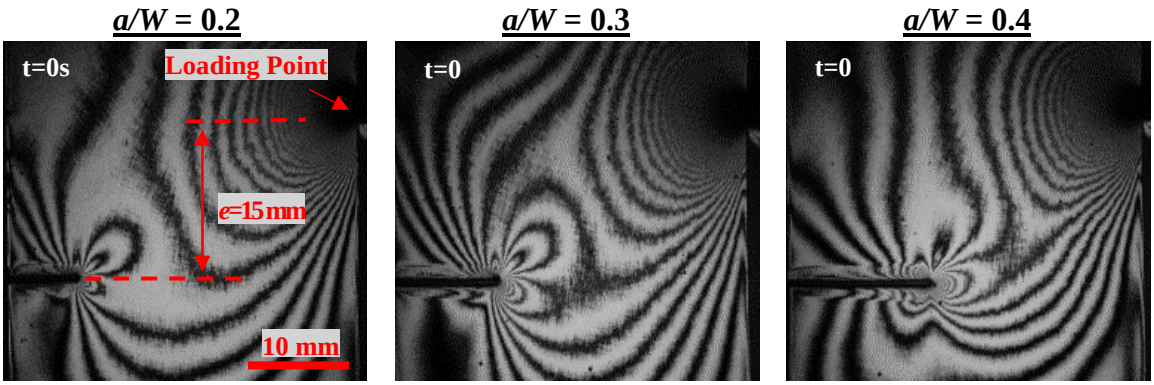

Figure 6-3: Isochromatic fringe images from 10% V_f samples under dynamic mixed-mode loading at t = 0 (crack initiation) for a/W = 0.2, 0.3, and 0.4

In each image, mixed-mode conditions are evident from the fringe asymmetry relative to the initial crack axis, where the fringe lobes appear "rotated" or 'tilted' about the crack tip. Additionally, as a/W was increased, further change in terms of fringe rotation was observed, indicating increasing mode-II stresses. From these initial results, it was clear that mode-mixity could be successfully controlled by adjusting the initial notch length. This procedure was repeated with 0%, 5%, and 15% V_f samples.

6.3: Experimental Results

Representative isochromatic fringe images of each sample volume fraction captured at t=-20 µs, 0 µs, and 20 µs are shown for a/W = 0.2, 0.3, and 0.4 in Figure 6-4, Figure 6-5, and Figure 6-6, respectively. In each case, a compressive stress wave enters the sample where the long-bar contacts the specimen. As the stress wave reaches the notch, it gets loaded, and fringe loops are formed around the tip. Fringe asymmetry with respect to the crack axis is apparent, indicating significant mode-mixity associated with

the presence of both in-plane normal and shear stresses near the crack-tip. As the stress waves reach the free edges, they reflect back into the specimen as tensile wave, opening the crack. From this combination of shear and tensile stresses, growth is initiated from the notch tip.

In order to test the composites under such dynamic mixed-mode loading conditions, two samples of each volume fraction and *a/W* ratio were tested and evaluated using the least-squares analysis discussed in Chapter 3. Additionally, each image was analyzed a minimum of three times, and the results were averaged to eliminate manual fringe digitization errors.

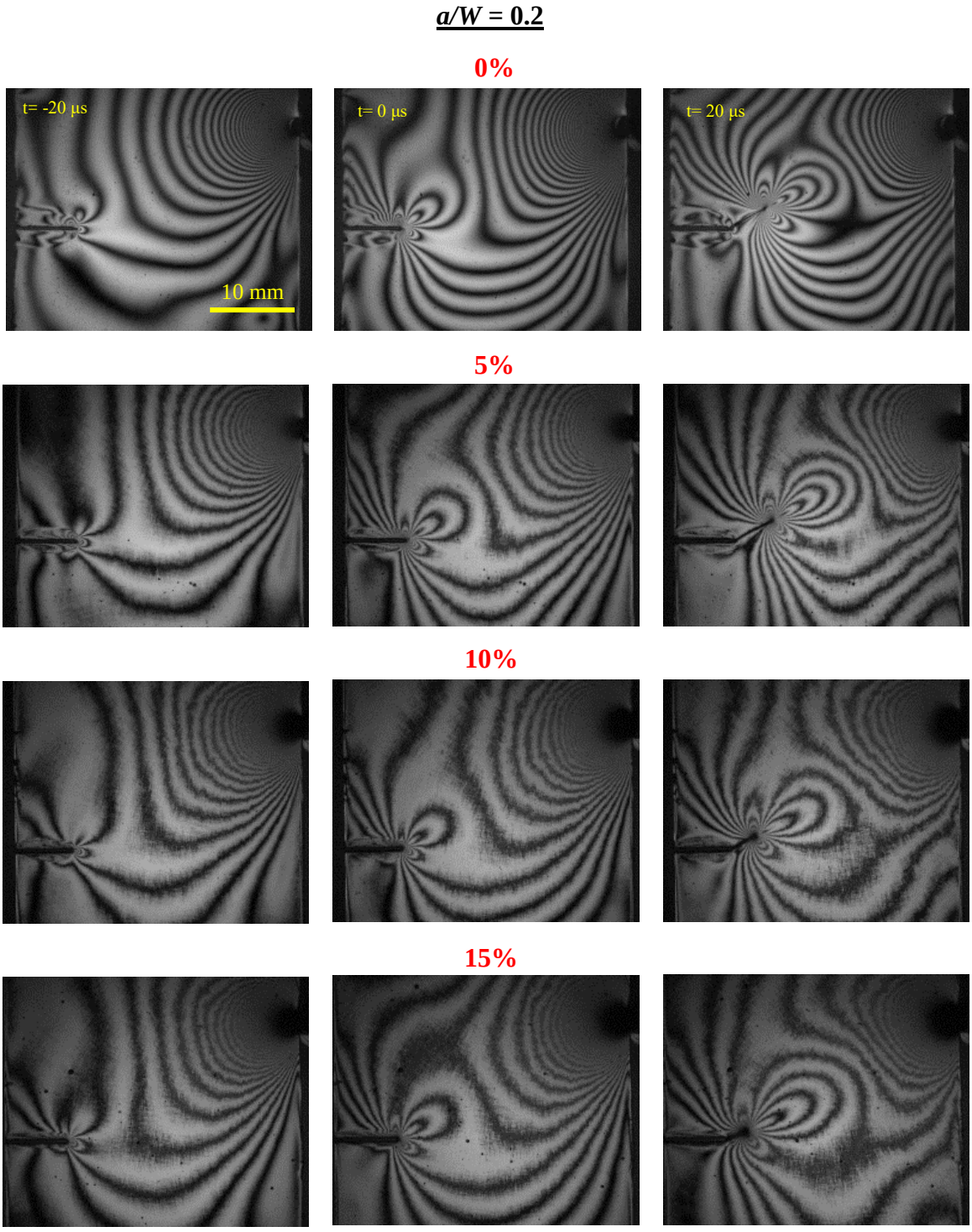

Figure 6-4: Isochromatic fringe patterns for 0%, 5%, 10%, and 15% V_f composites under dynamic mixed-mode loading (a/W = 0.2). Images are shown for t = -20 µs, 0 µs, and 20 µs shown (t = 0 corresponding to crack initiation)

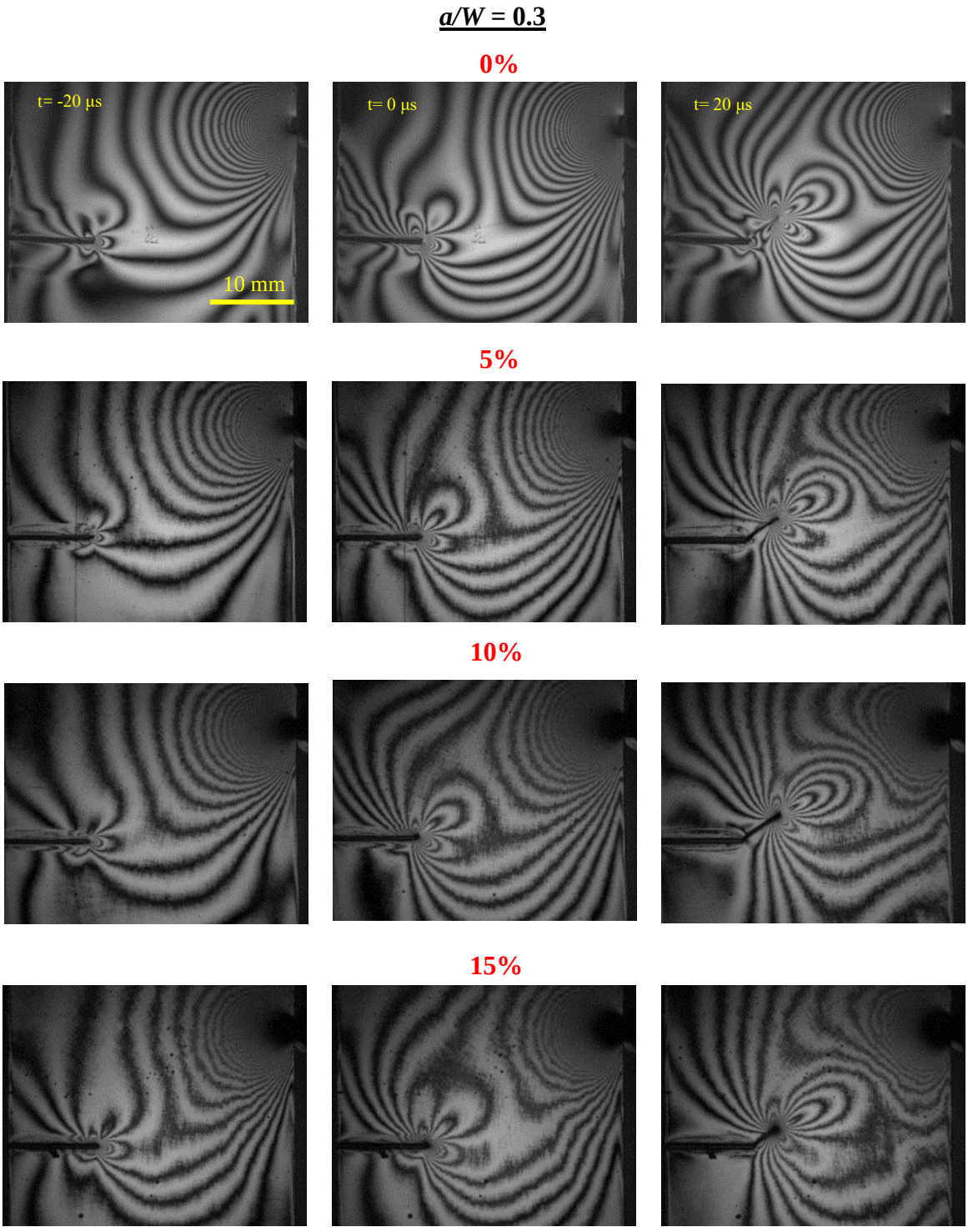

Figure 6-5: Isochromatic fringe patterns for 0%, 5%, 10%, and 15% V_f composites under dynamic mixed-mode loading (a/W = 0.3). Images are shown for t = -20 µs, 0 µs, and 20 µs shown (t = 0 corresponding to crack initiation)

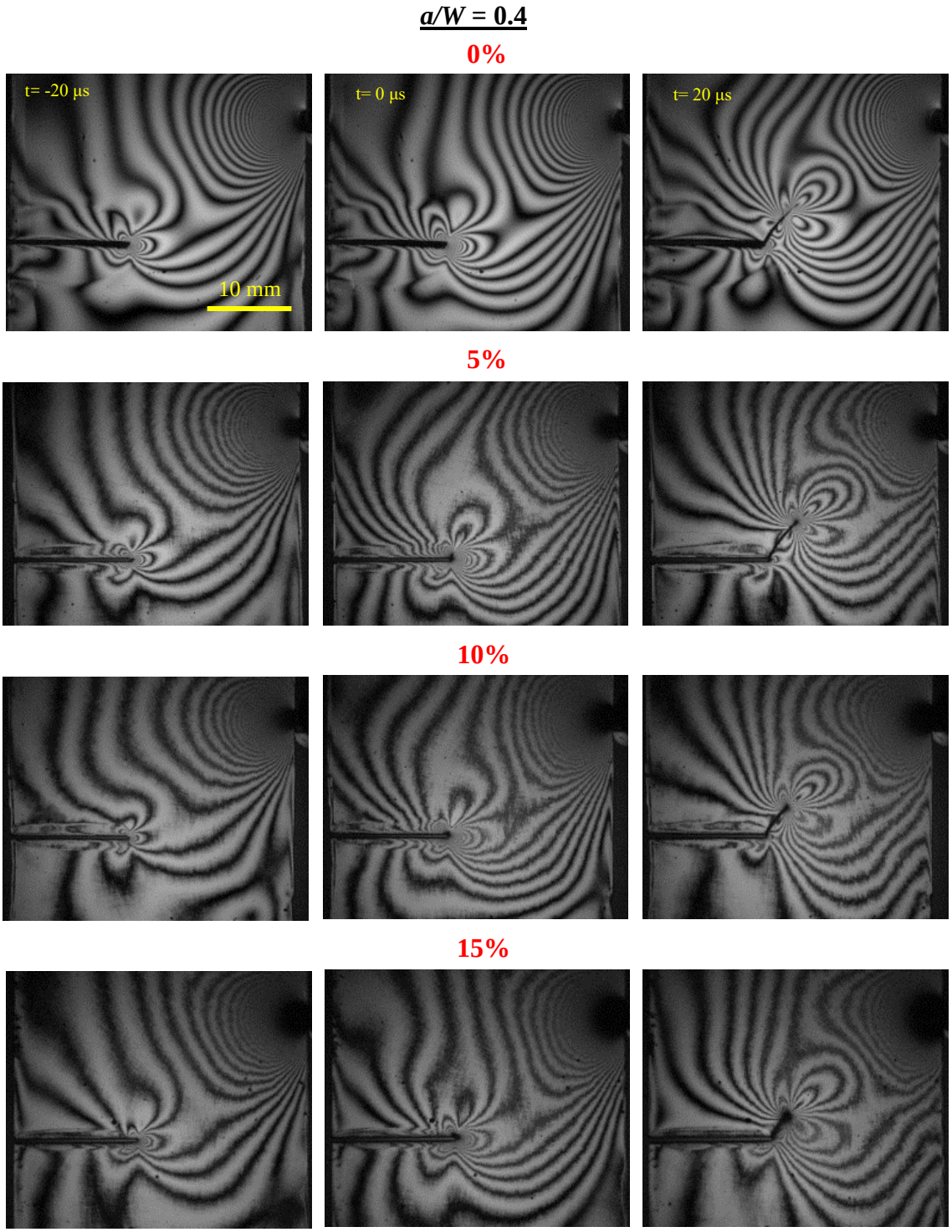

Figure 6-6: Isochromatic fringe patterns for 0%, 5%, 10%, and 15% V_f composites under dynamic mixed-mode loading (a/W = 0.4). Images are shown for t = -20 µs, 0 µs, and 20 µs shown (t = 0 corresponding to crack initiation)

6.3.1: Crack Initiation Angles

Representative images of 0% and 10% V_f samples captured at approximately 30 μs post crack initiation at a/W = 0.2, 0.3, and 0.4 are shown in Figure 6-7. In each case, the crack initiates from the machined notch tip at a kink angle relative to the initial notch. After approximately 10 μs the crack deviated from its initial angle and propagated towards the impact point on the right edge of the sample. This behavior can be seen in Figure 6-7, which shows measured crack initiation angles compared to the crack propagation angle at approximately 30 μs.

The crack initiation angle was measured for each sample and a/W ratio and are quantified in Table 6-1. As the a/W ratio was increased, an increase in the crack initiation angle was observed. Furthermore, as the volume fraction of filler increased, the crack initiation angle increased monotonically.

Table 6-1: Measured crack initiation angles comparison for 0%, 5%, 10%, and 15% V_f samples with a/W = 0.2, 0.3, and 0.4

V_f (%)	**Crack Initiation Angles (degrees)**		
	a/W = 0.2	a/W = 0.3	a/W = 0.4
0%	31.5 ± 0.2	51.3 ± 1.0	64.5± 1.2
5%	30.5 ± 0.3	48.1 ± 1.3	59.4 ± 0.7
10%	27.9 ± 0.3	46.5 ± 0.9	57.6 ± 0.5
15%	25.1 ± 0.2	43.9 ± 0.4	53.7 ± 1.3

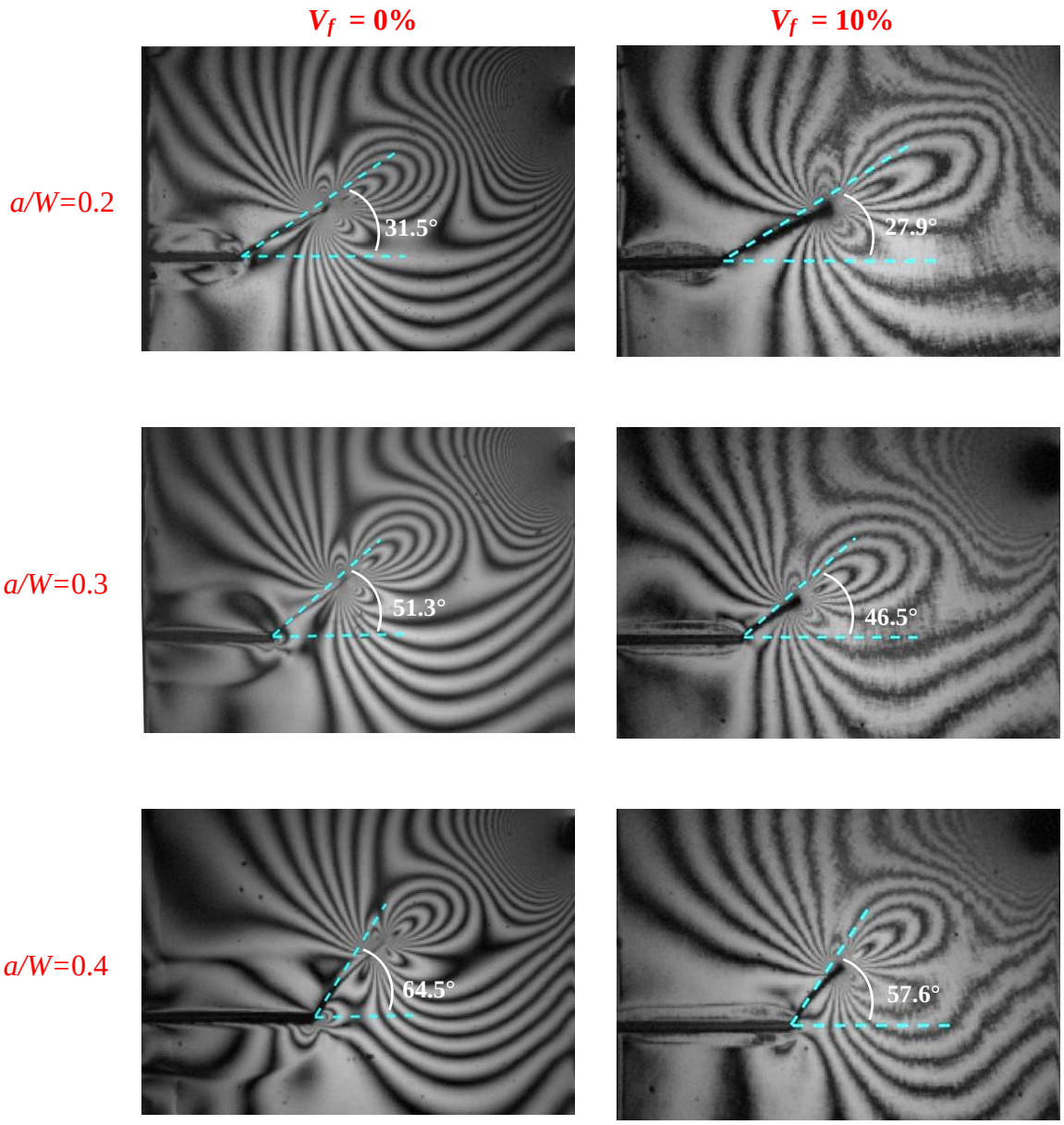

Figure 6-7: Photographs of crack initiation angle for 0% and 10% V_f and a/W = 0.2, 0.3, and 0.4 (t = ~30 µs post crack initiation)

6.3.2: Crack Velocity Histories

For each image, the position of the crack tip was measured and used to determine the instantaneous crack length from which the crack velocity histories were evaluated using the backward-difference method and are shown in Figure 6-8 –

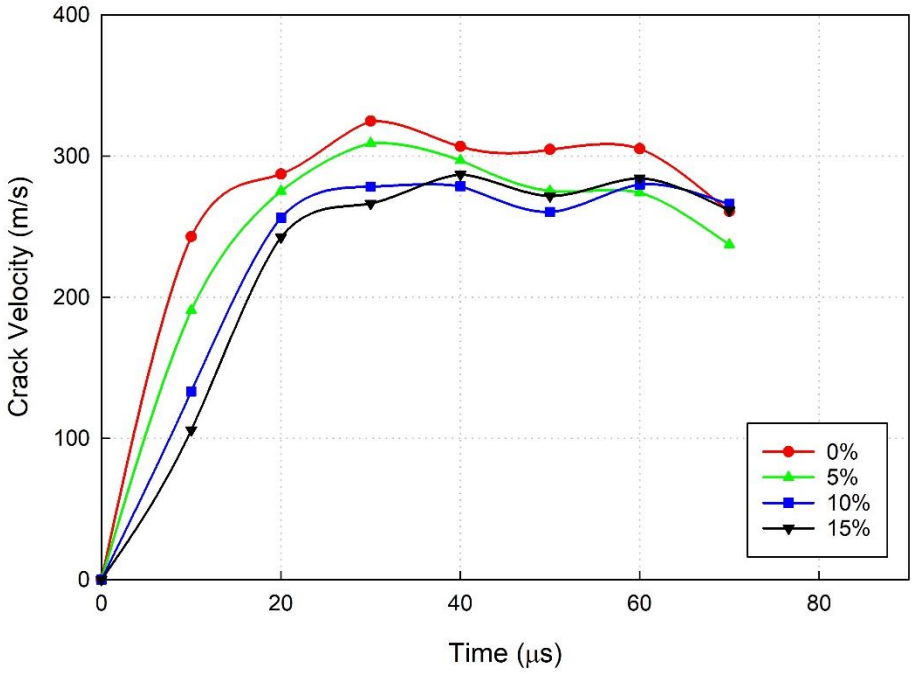

Figure 6-10.

In each case, a peak crack velocity occurs shortly after initiation, after which the crack begins to slow down as it continues to propagate towards the impact point.

For a/W = 0.2, peak crack velocities were approximately 378 m/s, 347 m/s, 306 m/s, and 291 m/s for V_f = 0%, 5%, 10%, and 15% samples, reflectively. For a/W = 0.3, peak crack velocities were approximately 329 m/s, 361 m/s, 337 m/s, and 324 m/s for V_f = 0%, 5%, 10%, and 15% samples, reflectively. Lastly, for a/W = 0.4, peak crack velocities were approximately 325 m/s, 309 m/s, 280 m/s, and 287 m/s for V_f = 0%, 5%,

10%, and 15% samples, reflectively. Clearly, a reduction in crack velocity was with respect to an increase in filler volume fraction in the matrix was observed in each *a/W* case.

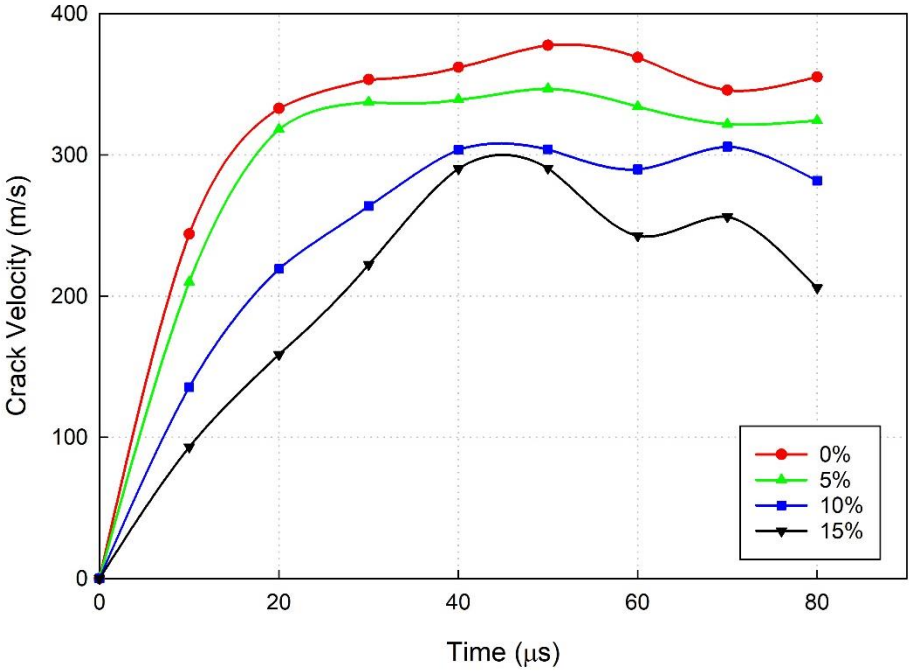

Figure 6-8: Measured crack velocity histories of 0%, 5%, 10%, and 15% V_f samples for dynamic mixed-mode fracture tests (a/W = 0.2)

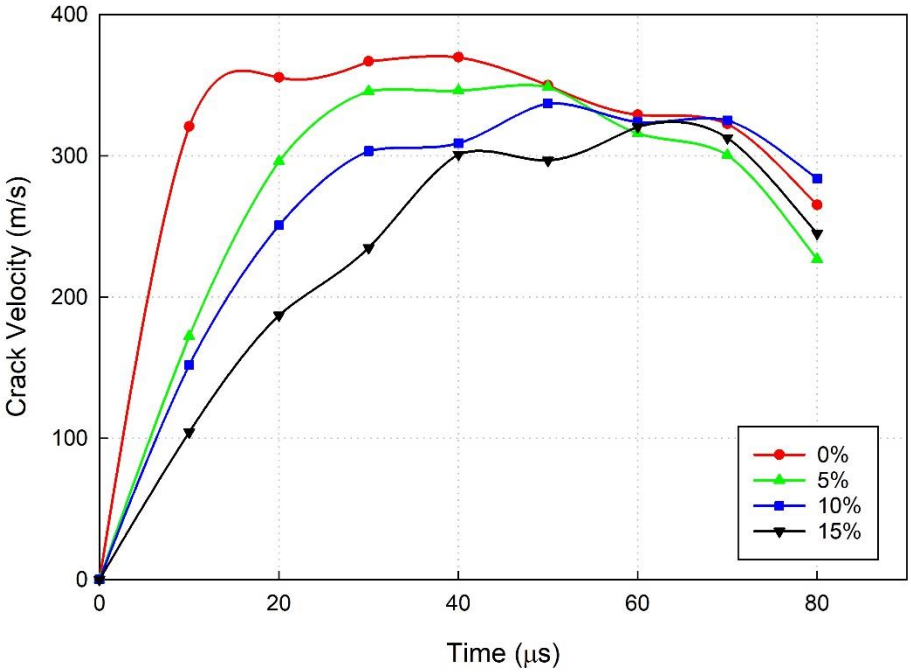

Figure 6-9: Measured crack velocity histories of 0%, 5%, 10%, and 15% V_f samples for dynamic mixed-mode fracture tests (a/W = 0.3)

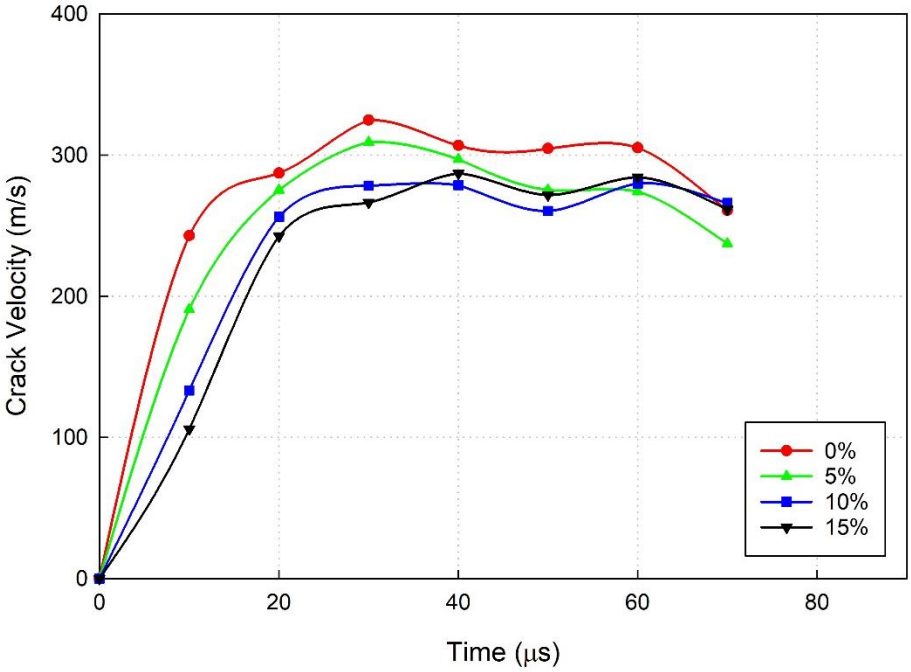

Figure 6-10: Measured crack velocity histories of 0%, 5%, 10%, and 15% V_f samples for dynamic mixed-mode fracture tests (a/W = 0.4)

6.3.3: Stress Intensity Factor Histories

To further study the mixed-mode dynamic fracture behavior of the glass-filled epoxy composites, an analysis of the stress intensity factor histories was performed. K_I and K_{II} values were extracted from the recorded images of the isochromatic fringes around the crack tip using the over-deterministic least-squares method described in the previous chapters. Additionally, as crack initiation occurred in mixed-mode conditions, the mode-I and mode-II stress intensity factors were used to evaluate the effective stress intensity factor (K_{eff}) using the following expression:

$$K_{eff} = \sqrt{K_I^2 + K_{II}^2} \qquad 6\text{-}1$$

<u>*a/W* = 0.2</u>

The first configuration that was tested in mixed-mode conditions was $a/W = 0.2$, and the resulting stress intensity factor histories are shown in Figure 6-11. For each V_f case, K_I and K_{II} values increase significantly prior to crack initiation, indicating the presence of both in-plane shear stress and normal stress around the crack k tip. Mode-I and mode-II SIFs reach peak magnitudes immediately before crack initiation, followed by a substantial drop due to unloading near the crack tip. As the crack continues to propagate, K_I increases while exhibiting an oscillatory behavior. $K_{II,}$ on the other hand, remains nearly zero for the remainder of the fracture event, indicating crack propagation under mode-I dominate conditions.

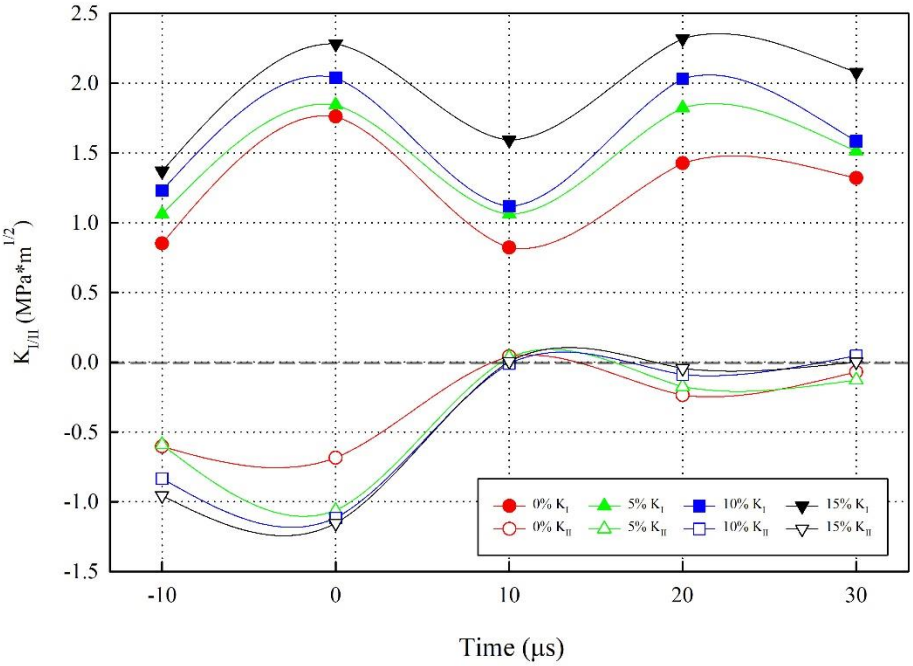

Figure 6-11: K_I and K_{II} histories for 0%, 5%, 10% and 15% V_f glass-filled epoxy composites under dynamic mixed-mode loading (a/W = 0.2)

Representative K_{eff} histories for 0%, 5%, 10%, and 15% volume fraction samples are shown in Figure 6-12. Evidently, an increase in K_{eff} values throughout the entire fracture event occurs with respect to an increased volume fraction of filler. Compared to the 0% case, 5% 10%, and 15% samples showed an improvement in the effective crack initiation toughness of 13%, 24%, and 36%, respectively.

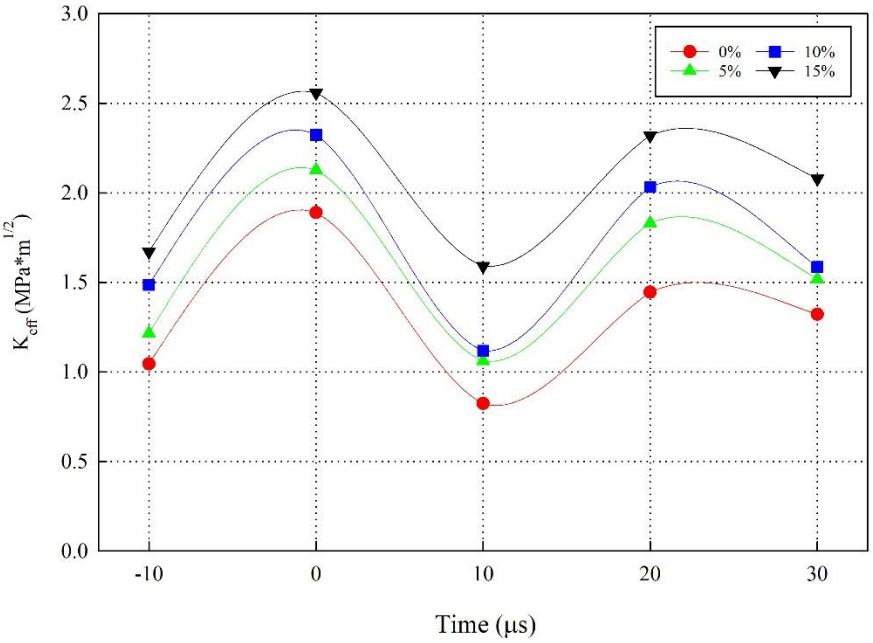

Figure 6-12: K_{eff} histories for 0%, 5%, 10% and 15% V_f glass-filled epoxy composites under dynamic mixed-mode loading (a/W = 0.2)

The measured mode-I, mode-II, and effective crack initiation toughness values are shown in Table 6-2. Each value is an average from two samples, and the error corresponds to one standard deviation from the mean.

Table 6-2: Measured K_I and K_{II} , and K_{eff} values for 0%, 5%, 10%, and 15% V_f samples at t = 0 (crack initiation) for a/W = 0.2

Filler % (V_f)	K_{Icr} (MPa√m)	K_{IIcr} (MPa√m)	K_{eff} (MPa√m)
0%	1.74 ± .06	-0.68 ± .05	1.87 ± .06
5%	1.84 ± .10	-1.06 ± .07	2.12 ± .08
10%	2.03 ± .11	-1.12 ± .10	2.32 ± .10
15%	2.28 ± .09	-1.16 ± .09	2.56 ± .09

***a/W* = 0.3**

The resulting stress intensity factor histories for the $a/W = 0.3$ are shown in Figure 6-13 K_I and K_{II} values (magnitude) increased until reaching a maximum at $t = 0$, then showed a significant drop after crack initiation. As the crack continued to propagate, K_I increased while K_{II} remained near zero, indicating crack propagation under mode-I dominate conditions.

While this trend in K_I and K_{II} values was similar to that seen in the $a/W = 0.2$ case, their magnitudes were quite different. The longer initial crack length contributed to significantly higher K_{II} values as well as a drop in K_I values throughout the observation window. Furthermore, a decrease in K_{eff} values at crack initiation can be seen for samples of each volume fraction compared to their $a/W = 0.2$ counterpart.

Representative K_{eff} histories for 0%, 5%, 10%, and 15% volume fraction samples are shown in Figure 6-14. K_{eff} values increased correspondingly with increasing filler volume fraction. Compared to the 0% case, 5% 10% and 15% samples showed an improvement in the effective crack initiation toughness of 27%, 49%, and 105%.

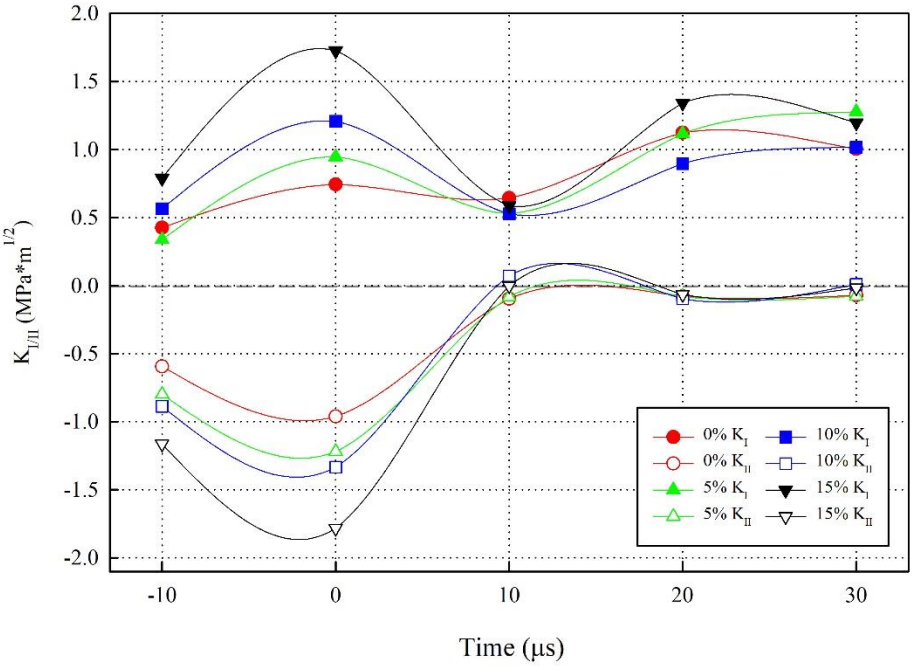

Figure 6-13: K_I and K_{II} histories for 0%, 5%, 10% and 15% V_f glass-filled epoxy composites under dynamic mixed-mode loading (a/W = 0.3)

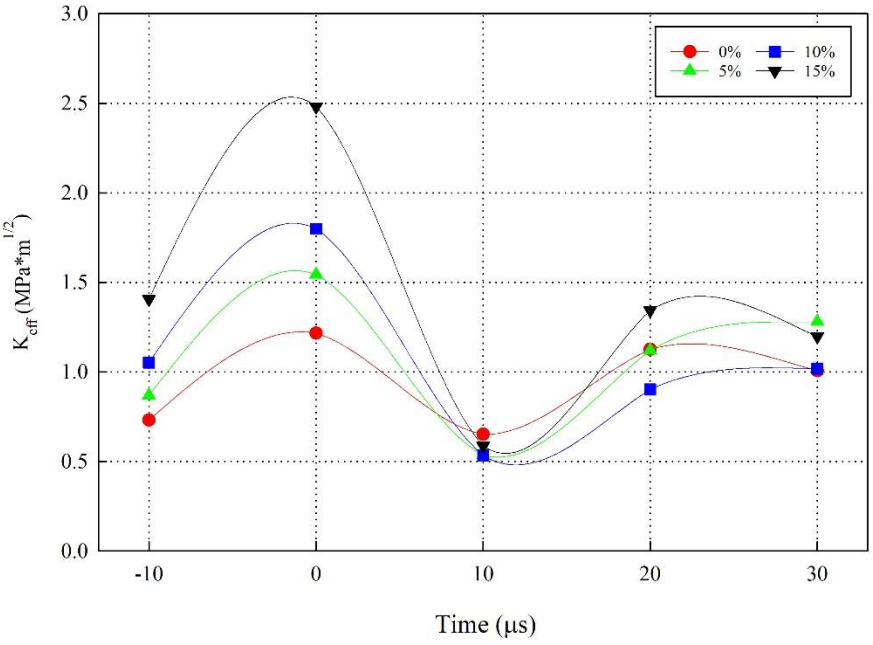

Figure 6-14: K_{eff} histories for 0%, 5%, 10% and 15% V_f glass-filled epoxy composites under dynamic mixed-mode loading (a/W = 0.3)

The measured mode-I, mode-II, and effective crack initiation toughness values are shown in Table 6-3. Each value is an average from two samples and the error corresponds to one standard deviation from the mean.

Table 6-3: Measured K_I and K_{II} , and K_{eff} values for 0%, 5%, 10%, and 15% V_f samples at t = 0 (crack initiation) for a/W = 0.3

Filler % (V_f)	K_{Icr} (MPa√m)	K_{IIcr} (MPa√m)	K_{eff} (MPa√m)
0%	0.74 ± .06	-0.96 ± .07	1.21 ± .06
5%	0.94 ± .05	-1.22 ± .06	1.54 ± .06
10%	1.21 ± .11	-1.33 ± .19	1.80 ± .15
15%	1.72 ± .12	-1.78 ± .14	2.48 ± .13

***a/W* = 0.4**

In the a/W = 0.4 case, a significant change to the stress intensity factor histories compared to the a/W = 0.2 and 0.3 cases can be observed. In this case, a/W was large enough with respect to the introduced eccentricity to cause crack closure prior to initiation. In the early stage of loading, the crack experiences a compressive stress on the crack face closest to the loading point causing the crack to close. However, after reaching the free edge (opposite of the impact edge), the compressive stress wave is reflected as a tensile wave causing the crack to open subsequently. This behavior can be seen as K_I values were negative before crack initiation and eventually turning positive in the post-initiation regime (t > 0). Additionally, the K_{II} values were the highest of all three

cases of a/W and lowest K_I values. These results can be seen in the K_I and K_{II} histories are shown in Figure 6-15:

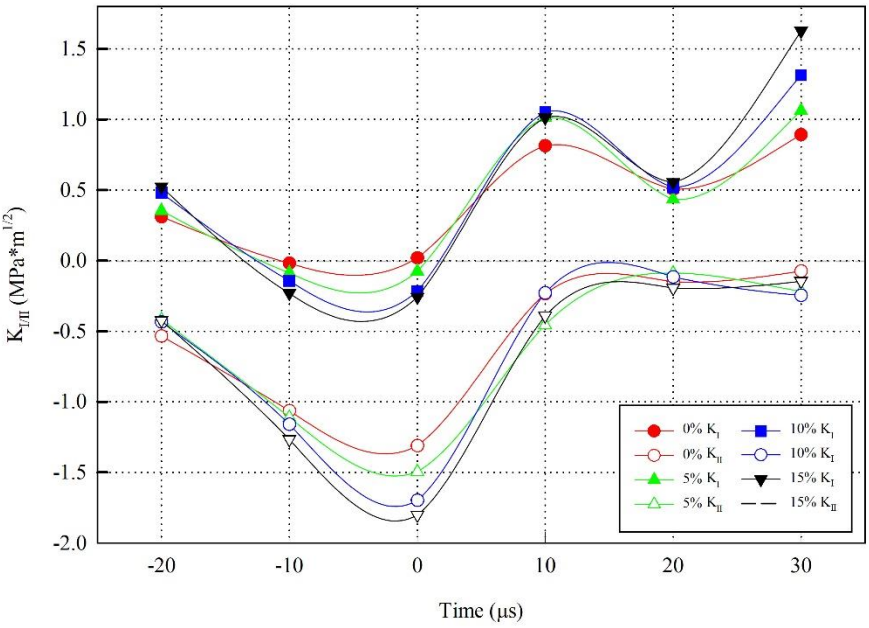

Figure 6-15: K_I and K_{II}, histories for 0%, 5%, 10% and 15% V_f glass-filled epoxy composites under dynamic mixed-mode loading (a/W = 0.4)

Representative K_{eff} histories for 0%, 5%, 10%, and 15% volume fraction samples are shown in Figure 6-16. As seen in both a/W = 0.2 and a/W = 0.3, K_{eff} values increased correspondingly with increasing filler volume fraction. Compared to the 0% case, 5% 10% and 15% samples showed an improvement in the effective crack initiation toughness of 15%, 31%, and 40%, respectively.

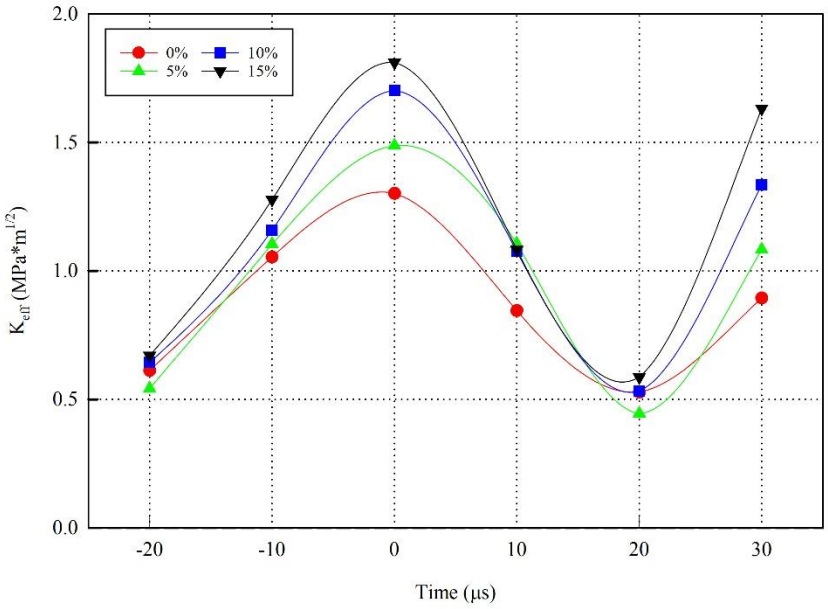

Figure 6-16: K_{eff} histories for 0%, 5%, 10% and 15% V_f glass-filled epoxy composites under dynamic mixed-mode loading (a/W = 0.4)

The measured mode-I, mode-II, and effective crack initiation toughness values are shown in Table 6-4:

Table 6-4: Measured K_I and K_{II} , and K_{eff} values for 0%, 5%, 10%, and 15% V_f samples at t = 0 (crack initiation) for a/W = 0.4

Filler % (V_f)	K_{Icr} (MPa√m)	K_{IIcr} (MPa√m)	K_{eff} (MPa√m)
0%	0.02 ± .05	-1.30 ± .10	1.30 ± .07
5%	-0.08 ± .03	-1.49 ± .06	1.49 ± .05
10%	-0.21 ± .04	-1.69 ± .08	1.70 ± .07
15%	-0.25 ± .15	-1.80 ± .10	1.82 ± .12

6.3.4: Mode-Mixity Histories

To characterize the relative amount of in-plane shear stress to normal stress around the crack-tip, the mode-mixity parameter (ψ) was calculated from the mode-I and mode-I SIFs using the following expression:

$$\psi = tan^{-1}\left(\frac{K_{II}}{K_I}\right) \qquad 6\text{-}2$$

Figure 6-17 (a)-(c) shows the mode-mixity histories of the glass-filled epoxy composites for *a/W* = 0.2, 0.3 and 0.4, respectively. In each case, peak mode-mixity values occurred in the initial stages after loading, indicating a significant presence of in-plane shear stress at the crack tip. After crack initiation, however, mode-mixity rapidly decreases to nearly zero in the *a/W* = 0.2 and 0.3 cases. For the *a/W* = 0.4 case, the mode-mixity values between -10 and -20 are seen.

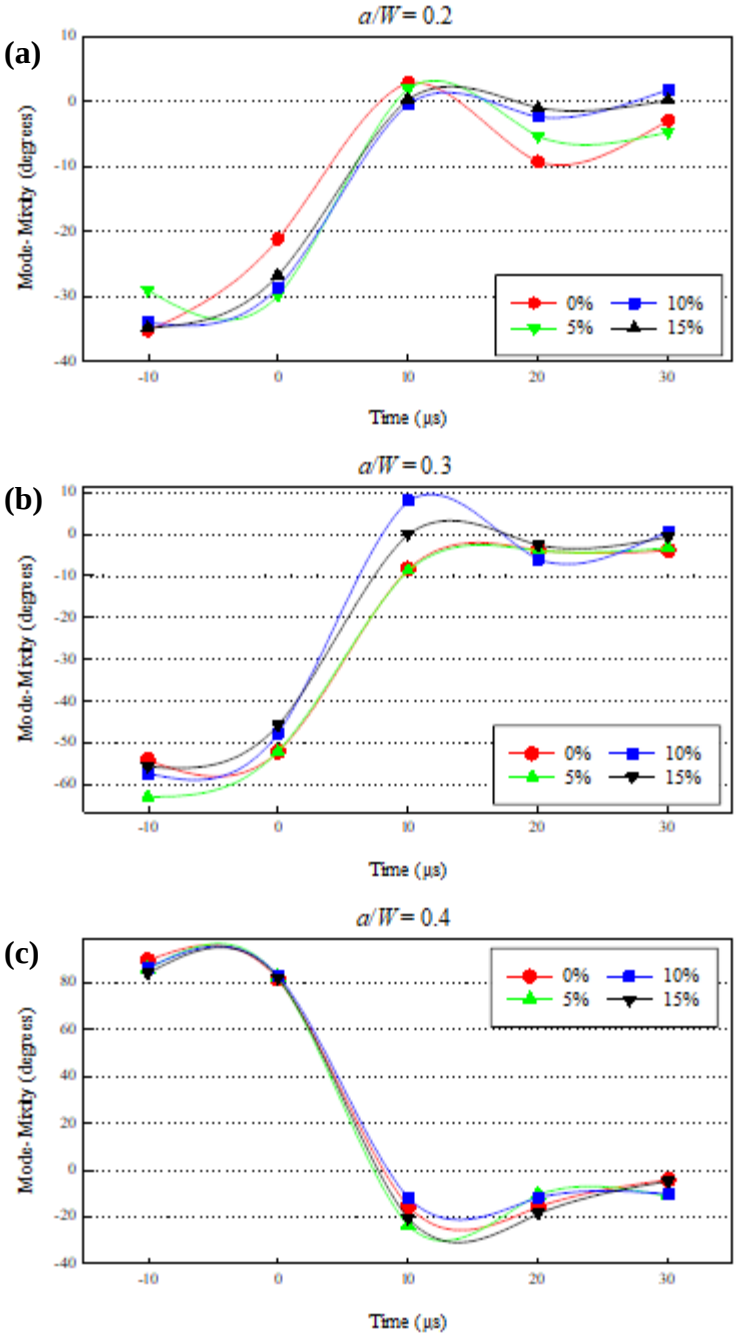

Figure 6-17: Mode-mixity histories for glass-filled epoxy composites under dynamic mixed-mode impact loading at (a) a/W = 0.2, (b) a/W = 0.3, (c) a/W = 0.4

Figure 6-18 shows a comparison of the mode-mixity histories for the three *a/W* configurations measured from representative samples of each volume fraction. Each V_f case shows a similar behavior where pre-initiation mode-mixity values increase with respect to increased crack length (*a/W* values).

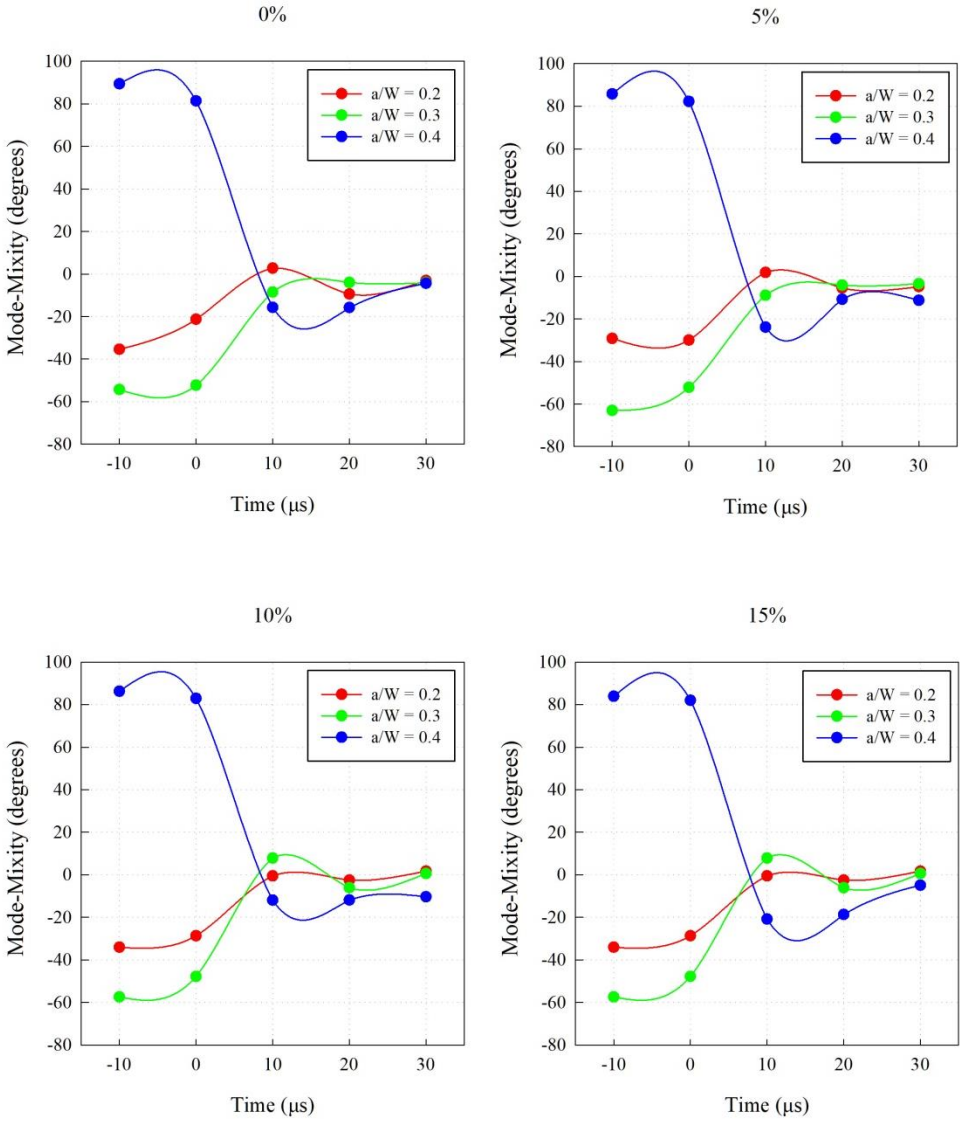

Figure 6-18: Mode-mixity histories of representative 0%, 5%, 10%, and 15% V_f samples for each *a/W* configuration

The measured mode-mixity values for each sample at crack initiation are shown in Table 6-5. Evidently, mode-mixity was effectively altered by crack length.

Table 6-5: Mode-mixity at crack initiation (t = 0) comparison for 0%, 5%, 10%, and 15% Vf samples with a/W = 0.2, 0.3, and 0.4

V_f (%)	**Mode-Mixity (degrees)**		
	a/W = 0.2	a/W = 0.3	a/W = 0.4
0%	-21.4°	-52.4°	89.1°
5%	-29.9°	-52.4°	86.9°
10%	-28.9°	-47.7°	82.9°
15%	-27.0°	-46.0°	82.1°

CHAPTER 7: CONCLUSIONS

In this work, a method of producing transparent glass-filled epoxy composites by refractive index matching of an epoxy matrix and rod-shaped E-glass fillers has been developed. These composites were processed at varying filler volume fractions (V_f) from 0% to 15%, with transparency maintained at each V_f. Using photoelasticity, the role of filler volume fraction, loading rate, and mode-mixity on the fracture behavior of the transparent composites were studied.

Initial investigations included ultrasonic measurements to determine the physical and elastic properties of each composite, as well as quasi-static three-point bending of edge-cracked specimens to determine the critical stress intensity factor (K_{Icr}) values. Improvement in K_{Icr} of 4.9%, 19.1%, and 27.2% over neat epoxy was seen in the 5%, 10%, and 15% volume fraction samples, respectively.

The glass-filled epoxy composites were observed to exhibit birefringence, thus making it feasible to mechanically study the fracture mechanics of the material using transmission photoelasticity. To perform a photoelastic analysis of the composites, the stress optic constant, f_σ, had to be evaluated for each sample. This was done using symmetric four-point bending configuration and recording the fringe patterns with a circular dark-field polariscope and time-lapse photography. Next, to validate photoelasticity as an accurate method to investigate the fracture behavior of these composites, edge-notched samples were loaded in the quasi-static four-point bending setup. Using a circular dark-field polariscope, isochromatic fringes were observed around the crack tip, and stress-intensity factors were evaluated at various load levels.

These values were compared to their analytical counterparts and were found to match closely. Once photoelastic evaluation proved successful, a more robust over-deterministic nonlinear least-squares analysis approach was used to determine the mode-I and mode-II stress intensity factors, K_I and K_{II}.

Next, the dynamic mode-I fracture behavior of the transparent glass-filled epoxy composites was evaluated with respect to two parameters: loading rate and filler volume fraction. Edge notched glass-filled epoxy composite samples were prepared at 0% (neat epoxy), 5%, 10%, and 15% filler volume fractions and were tested using three district loading configurations in order to vary strain rate. A dark-field circular polariscope in conjunction with high-speed photography was employed to capture the dynamic fracture events. From the recorded images, crack velocity histories were evaluated, which showed a substantial decrease in the apparent crack velocity with respect to the increasing volume fraction of fillers. Additionally, for each loading rate, as the volume fraction of the filler material was increased, a monotonic increase in the K_{Icr} values corresponding to crack initiation in this transparent composite was observed. A complementary finite element analysis of pre-crack initiation SIF values was performed, showing a good match with the experimental results.

Finally, the high-speed photoelastic measurements were extended to mixed-mode (mode-I + mode-II) fracture of these transparent glass-epoxy composites. To study the volume fraction effect on the mixed-mode dynamic fracture of the composites, edge notched samples were once again prepared at 0%, 5%, 10%, and 15% filler volume fractions. The mixed-mode fracture experiments were conducted using a long-bar setup

aligned to impact the specimens at a set eccentricity. To extend the mixed-mode fracture study, a simple method of varying the pre-notched crack length was adopted to alter the mode-mixity at crack initiation. Thus, samples of three distinct *a/W* ratios (0.2, 0.3, and 0.4) were prepared for each volume fraction. Using a high-speed photoelasticity setup, images of the isochromatic fringes around the crack tip were recorded from both pre and post-crack initiation. From these images, crack initiation angles, crack velocity histories, and the mode-I and mode-II stress intensity factor histories were measured. Additionally, K_I and K_{II} values were used to evaluate the effective stress intensity factor (K_{eff}) and mode-mixity histories.

For the a/W = 0.2 and 0.3 cases, a similar pattern in the extracted SIF histories was observed where both K_I and K_{II} increased monotonically up until crack initiation, after which K_{II} dropped to nearly zero, and the crack propagation occurred in mode-I dominant conditions. In the a/W = 0.4 case, a significantly different pattern in the stress intensity factor histories was apparent. In this case, *a/W* was large enough with respect to the introduced eccentricity to cause crack closure prior to initiation. As such, K_I values were negative prior to crack initiation. Additionally, the pre-initiation K_{II} values were the highest of all three *a/W* cases. In the post-initiation regime (t > 0), K_{II} values approached zero, while positive K_I values were observed, similar to the a/W = 0.2 and 0.3 cases.

To investigate the volume fraction effect on the mixed-mode crack initiation toughness, the extracted SIF values for each sample were compared to that of the neat epoxy (0% V_f) samples from the corresponding *a/W* configuration. For each case, an

improvement in the effective crack initiation toughness was observed with respect to an increase in filler volume fraction.

7.1: Future Directions

In this work, the stress-optic constants were measured for glass-filled epoxy composites of volume fractions ranging between 0% and 15%. A non-linear increase in these values was observed with respect to increased volume fraction of the filler. Further investigation of this behavior could be conducted to develop a Rule of Mixtures that relates the stress-optic constants of the individual constituents to that composite material.

In addition, the dynamic fracture behavior of the glass-filled epoxy composites was studied using a high-speed photoelasticity setup. Due to the relatively low frame rate of the camera and the high-speed nature of these fracture events, only a handful of images could be captured. Conducting similar tests with a camera capable of recording at higher frame rates could provide valuable insight into the material behavior under these loading conditions.

Finally, the mixed-mode fracture study presented in this work considered the effect of volume fraction and mode-mixity on the fracture behavior of the glass-filled epoxy composites. An investigation of the loading rate effect on the mixed-mode fracture behavior could also be performed.

References

[1] Z. Yin, F. Hannard, and F. Barthelat, "Impact-resistant nacre-like transparent materials," *Science*, vol. 364, pp. 1260–1263, 2019.

[2] "Transparent Armor," *The AMPTIAC Newsletter*, Fall 2000.

[3] B. Sundaram and H. Tippur, "Dynamic mixed-mode fracture behaviors of PMMA and Polycarbonate," *Eng. Fract. Mech.*, vol. 176, Mar. 2017, doi: 10.1016/j.engfracmech.2017.02.029.

[4] Y. Kagawa, H. Iba, M. Tanaka, H. Sato, and T. Chang, "Fabrication and optical/thermal properties of glass particle–epoxy optically transparent composites," *Acta Mater.*, vol. 46, no. 1, pp. 265–271, Dec. 1998, doi: 10.1016/S1359-6454(97)00190-0.

[5] H. Lin, D. E. Day, and J. O. Stoffer, "Optical and mechanical properties of optically transparent poly(methyl methacrylate) composites," *Polym. Eng. Sci.*, vol. 32, no. 5, pp. 344–350, 1992, doi: 10.1002/pen.760320507.

[6] S.-Y. Fu, X.-Q. Feng, B. Lauke, and Y.-W. Mai, "Effects of particle size, particle/matrix interface adhesion and particle loading on mechanical properties of particulate–polymer composites," *Compos. Part B Eng.*, vol. 39, no. 6, pp. 933–961, Sep. 2008, doi: 10.1016/j.compositesb.2008.01.002.

[7] N. Jain and A. Shukla, "Mixed Mode Dynamic Fracture in Particulate Reinforced Functionally Graded Materials," *Exp. Mech.*, vol. 46, no. 2, pp. 137–154, Apr. 2006, doi: 10.1007/s11340-006-5867-0.

[8] H. Iba, T. Chang, and Y. Kagawa, "Optically transparent continuous glass fibre-reinforced epoxy matrix composite: fabrication, optical and mechanical properties," *Compos. Sci. Technol.*, vol. 62, no. 15, pp. 2043–2052, Nov. 2002, doi: 10.1016/S0266-3538(02)00156-2.

[9] V. Kushvaha, A. Branch, and H. Tippur, "Effect of Loading Rate on Dynamic Fracture Behavior of Glass and Carbon Fiber Modified Epoxy.," *Dyn. Behav. Mater. Vol. 1 9783319007700*, p. 169, Jan. 2014.

[10] R. Kitey and H. Tippur, "Role of particle size and filler-matrix adhesion on dynamic fracture of glass-filled epoxy. I. Macromeasurements," *Acta Mater.*, vol. 53, pp. 1153–1165, Jan. 2005, doi: 10.1016/j.actamat.2004.11.012.

[11] M. Kirugulige and H. Tippur, "Mixed-Mode Dynamic Crack Growth in a Functionally Graded Particulate Composite: Experimental Measurements and Finite Element Simulations," *J. Appl. Mech.-Trans. Asme - J APPL MECH*, vol. 75, Sep. 2008, doi: 10.1115/1.2932095.

[12] J. R. Klepaczko *et al.*, “Behavior of particle-filled polymer composite under static and dynamic loading,” *Eng. Fract. Mech.*, vol. 75, no. 1, pp. 136–152, Jan. 2008, doi: 10.1016/j.engfracmech.2007.02.016.

[13] “Crack propagation in a glass particle-filled epoxy resin Part 1. Effect of particle volume fraction and size: Spanoudakis, J. and Young, R.J. Journal of Materials Science Vol 19 (1984) pp 473–486,” *Composites*, vol. 15, no. 3, p. 242, Jul. 1984, doi: 10.1016/0010-4361(84)90313-6.

[14] V. Kushvaha and H. Tippur, “Effect of filler shape, volume fraction and loading rate on dynamic fracture behavior of glass-filled epoxy,” *Compos. Part B Eng.*, vol. 64, pp. 126–137, 2014, doi: https://doi.org/10.1016/j.compositesb.2014.04.016.

[15] M. Kerker, *The Scattering of Light and Other Electromagnetic Radiation*, vol. 16. Academic Press, 1969.

[16] H. Iba and Y. Kagawa, “Light transmittance of continuous fibre-reinforced composites: analysis, model experiment and parametric study,” *Philos. Mag. B-Phys. Condens. MATTER Stat. Mech. Electron. Opt. Magn. Prop.*, vol. 78, no. 1, pp. 37–52, Jul. 1998.

[17] T. Liu, F. Xiang, X. Qi, W. Yang, R. Huang, and Q. Fu, “Optically transparent poly(methyl methacrylate) with largely enhanced mechanical and shape memory properties via in-situ formation of polylactide stereocomplex in the matrix,” *Polymer*, vol. 126, pp. 231–239, Sep. 2017, doi: 10.1016/j.polymer.2017.08.047.

[18] J. R. Olson, D. E. Day, and J. O. Stoffer, “Fabrication and Mechanical Properties of an Optically Transparent Glass Fiber/Polymer Matrix Composite,” *J. Compos. Mater.*, vol. 26, no. 8, pp. 1181–1192, Aug. 1992, doi: 10.1177/002199839202600806.

[19] H. Sato, H. Iba, and T. Naganuma, “Effects of the difference between the refractive indices of constituent materials on the light transmittance of glass-particle-dispersed epoxy-matrix optical composites,” *Philos. Mag. B Phys. Condens. Matter Stat. Mech. Electron. Opt. Magn. Prop.*, vol. 82, pp. 1369–1386, Jul. 2002, doi: 10.1080/13642810208220726.

[20] S. K. Khanna, M. D. Ellingsen, and R. M. Winter, “Investigation of Fracture in Transparent Glass Fiber Reinforced Polymer Composites Using Photoelasticity,” *J. Eng. Mater. Technol.*, vol. 126, no. 1, pp. 1–7, Jan. 2004, doi: 10.1115/1.1631022.

[21] M. Schoßig, C. Bierögel, W. Grellmann, and T. Mecklenburg, “Mechanical behavior of glass-fiber reinforced thermoplastic materials under high strain rates,” *Polym. Test.*, vol. 27, no. 7, pp. 893–900, Oct. 2008, doi: 10.1016/j.polymertesting.2008.07.006.

[22] M.-S. Cao *et al.*, “Dynamic compressive response and failure behavior of fiber polymer composites embedded with tetra-needle-like ZnO nanowhiskers,” *Compos. Struct.*, vol. 92, no. 12, pp. 2984–2991, 2010, doi: https://doi.org/10.1016/j.compstruct.2010.05.010.

[23] C. Elanchezhian, B. V. Ramnath, and J. Hemalatha, “Mechanical Behaviour of Glass and Carbon Fibre Reinforced Composites at Varying Strain Rates and Temperatures,” *3rd Int. Conf. Mater. Process. Characterisation ICMPC 2014*, vol. 6, pp. 1405–1418, Jan. 2014, doi: 10.1016/j.mspro.2014.07.120.

[24] M. M. Shokrieh and M. J. Omidi, “Compressive response of glass–fiber reinforced polymeric composites to increasing compressive strain rates,” *Compos. Struct.*, vol. 89, no. 4, pp. 517–523, Aug. 2009, doi: 10.1016/j.compstruct.2008.11.006.

[25] J. W. Dally and W. F. Riley, *Experimental Stress Analysis*, 4th Edition. McGraw Hill, 2005.

[26] M. A. Schroedl and C. W. Smith, “Local Stresses near Deep Surface Flaws under Cylindrical Bending Fields,” in *Progress in Flaw Growth and Fracture Toughness Testing*, J. Kaufman, J. Swedlow, H. Corten, J. Srawley, R. Heyer, E. Wessel, and G. Irwin, Eds. West Conshohocken, PA: ASTM International, 1973, pp. 45–63.

[27] H. Tada, P. C. Paris, and G. R. Irwin, *The Stress Analysis of Cracks Handbook, Third Edition*. ASME Press, 2000.

[28] D. J. Frew, M. J. Forrestal, and W. Chen, “A split Hopkinson pressure bar technique to determine compressive stress-strain data for rock materials,” *Exp. Mech.*, vol. 41, no. 1, pp. 40–46, Mar. 2001.

[29] R. Bedsole and H. Tippur, “Dynamic Fracture Characterization of Small Specimens: A Study of Loading Rate Effects on Acrylic and Acrylic Bone Cement,” *J. Eng. Mater. Technol.*, vol. 135, p. 031001, Jul. 2013, doi: 10.1115/1.4023405.

[30] R. W. Bedsole, P. B. Bogert, and H. V. Tippur, “An experimental investigation of interlaminar and intralaminar dynamic fracture of CFRPs: Effect of matrix modification using carbon nanotubes,” *Compos. Struct.*, vol. 132, pp. 1043–1055, Nov. 2015, doi: 10.1016/j.compstruct.2015.07.016.

[31] M. A. Kaiser, “Advancements in the Split Hopkinson Bar Test,” Virginia Polytechnic Institute and State University: Blacksburg, Virginia, 1998.